Development of Miniaturized Long-Range Optical Coherence Tomography for Smart Laser Surgery System

Inaugural dissertation

to
be awarded the degree of Dr. sc. med.

presented at
the Faculty of Medicine
of the University of Basel

by
Arsham Hamidi
from Arak, Iran

Basel, 2023

Approved by the Faculty of Medicine
on application of

Prof. Dr. Azhar Zam, University of Basel, *First examiner*
Prof. Dr. Philippe C. Cattin, University of Basel, *Second examiner*
Prof. Dr. med. Alexander A. Navarini, University of Basel, *Further advisor*
Dr. Ferda Canbaz, University of Basel, *Further advisor*
Prof. Dr. Thomas E. Milner, UCI Beckman Laser Institute & Medical Clinic, *External expert*

Basel, 20nd March 2023

Prof. Dr. Primo Leo Schär
Dean

To my parents (Azam and Hossein) and my beloved wife (Fariba Ghafouri), who is the happiness and motivation of my life.

ACKNOWLEDGMENTS

First and foremost, I am incredibly grateful to my supervisor, Prof. Dr. Azhar Zam, for giving me the opportunity to work on such a fantastic project and for his support during my studies and the development of my thesis project. I would like to extend my deepest gratitude to Prof. Dr. Philippe Cattin for the discussions and valuable feedback, which has improved my research. Moreover, I am very grateful to Prof. Dr. Alexander Navarini for his guidance and feedback from a medical point of view. I appreciate that he took the time for our meetings despite his busy schedule. Dr. Ferda Canbaz deserves special acknowledgment for her supervision. Midway through my doctoral studies, she accepted becoming a supervisor on the project and carrying out the study was only possible because of her contribution. I would like to acknowledge all my colleagues in the flagship MIRACLE project; in particular, I want to thank Yakub Bayhaqi, Christian Haas, Sandra Drusová, Cédric Duverney, Neha Sharma, and the former members of the biomedical laser and optics group (BLOG).

I would like to acknowledge Prof. Dr. Thomas Milner from the University of California for kindly being the external examiner of this thesis. Also, a great thanks to Prof. Dr. Georg Rauter for chairing my defense.

Last but not least, I would like to thank my wife, Fariba Ghafouri, for her great support during my doctoral studies. Without her support, I would not have had enough motivation to do this. I want to thank my family and friends, especially my parents (Azam Aslani and Hossein Hamidi), for their support. Finally, I would like to thank every single person I could not mention here who has helped me and who has given me input, ideas, and motivation.

CONTENTS

iv

Acronyms and abbreviations

MIRACLE *Minimally Invasive Robot-Assisted Computer-guided LaserosteotomE*

Er:YAG *erbium-doped yttrium aluminium garnet*

Nd:YAG *neodymium-doped yttrium aluminum garnet*

LIBS *laser-induced breakdown spectroscopy*

MIS *minimally invasive surgery*

DOF *depth of focus*

TD-OCT *time-domain OCT*

FD-OCT *Fourier-domain OCT*

SD-OCT *spectral-domain OCT*

SS-OCT *swept-source OCT*

SNR *signal-to-noise ratio*

GI *astrointestinal*

CW *continuous wave*

OPD *optical path difference*

SUMMARY

Optical coherence tomography (OCT) is a well-established interferometric imaging technology in biology and medicine. Nowadays, OCT has many applications in different clinical specialties due to its capability to provide high-resolution three-dimensional images of biological tissue in real time and remotely. In addition to the main application of OCT as a noninvasive optical biopsy, its features make it an ideal candidate as a visual-feedback system during laser surgery. OCT-assisted laser surgery can compensate for the primary inherent drawback of laser-surgery systems, namely, their feedback. In this thesis, a long-range OCT system was developed to provide the required feedback for surgeons during laser osteotomy.

In the first part of this thesis, a long-range and extended *depth of focus* (DOF) swept-source OCT system (SS-OCT) was developed. The long-range SS-OCT system demonstrated an imaging range of 26.2 mm and an extended DOF of 28.7 mm. The custom-made OCT system was integrated with an Er:YAG laser to monitor and control the depths of laser-induced cuts in real-time. In addition to the real-time visual feedback, a tissue-sensor (*laser-induced breakdown spectroscopy* (LIBS)) system was integrated with an Er:YAG laser to achieve closed-loop laser osteotomy. The closed-loop system allowed tissue-selective laser surgery with a controlled ablation depth in the target tissue (bone).

Thermal damage during bone surgery is a drawback of mechanical and laser methods. For this reason, the next goal of the thesis was to investigate the potential of a phase-sensitive OCT system to monitor temperature increases in the tissue during laser osteotomy. The developed method is based on calibrating the photothermal expansion of tissue with its corresponding temperature increase. The preliminary results of the phase-sensitive OCT system show its potential to monitor temperature increases in bone tissue beyond the coagulation level.

In the last part of this thesis, a miniaturized prototype of the fiber-based Er:YAG laser and OCT system were designed and fabricated. The miniaturized, integrated setup could potentially be used in minimally invasive laser surgery. The developed system could perform several preplanned ablation cuts (maximum ablation depth of 5 mm) with the assistance of the real-time depth monitoring provided by the OCT system. This study was part of the *Minimally Invasive Robot-Assisted Computer-guided LaserosteotomE* (MIRACLE) project, which aims to develop a robotic endoscope for performing laser-based bone surgery.

ZUSAMMENFASSUNG

Optische Koh"renztomografie (OCT) ist eine weit verbreitete interferometrische Bildgebungstechnik in der Biologie und der Medizin. Heutzutage gibt es, aufgrund der F"ahigkeit hochaufl"osende, dreidimensionale Bilder von biologischen Geweben aufzunehmen, viele OCT-Applikationen in verschiedenen medizinischen Fachrichtungen. Neben der Hauptanwendung des OCT als nicht invasive optische Biopsie, ist sie wegen ihrer Eigenschaften ein idealer Kandidat als visuelles Feedback-System während der chirurgischen Laserbehandlung. OCT-unterstützte Laserchirurgie kann den primären eigenen Nachteil von Laserchirurgiesystemen, nämlich ihre Rückkopplung kompensieren. In dieser Arbeit wurde ein Long-Range OCT System entwickelt, das dem Chirurgen während einer Laserosteotomie das erforderliche Feedback bereitstellt.

Im ersten Teil dieser Arbeit wurde ein Long-range und Extended Depth-of-Focus (DOF) Swept-Source-OCT System (SS-OCT) entwickelt. Das Long-Range SS-OCT System zeigte einen Bildbereich von 26.2mm und einen Extended DOF von 28.7mm. Das ma"sgeschneiderte OCT System wurde mit einen Er:YAG Laser integriert um die Tiefe der laserinduzierten Schnitte in Echtzeit zu überwachen. Zus"atzlich zum visuellen Feedback in Echtzeit wurde ein Gewebesensorsystem (Laser Induced Breakdown Spectroscopy (LIBS)) mit einem Er:YAG laser integriert um eine Closed-Loop Laserosteotomie zu erreichen.. Das Closed-Loop System ermöglichte eine gewebeselektive Laserchirurgie mit kontrollierten Ablationstiefen im Zielgewebe (Knochen). Ein Nachteil der Knochenchirurgie mit Lasern oder mechanisch sind thermische Sch"aden. Deshalb war das n"achste Ziel der Arbeit, das Potential eines phasensensitiven OCT zur "Uberwachung von Temperaturerh"ohungen im Gewebe w"ahrend der Laserosteotomie zu untersuchen. Die entwickelte Methode basiert auf der Kalibrierung der photothermalen Ausdehnung mit der entsprechenden Temperaturerh"ohung. Die vorl"aufigen Resultate des phasensensitiven OCT Systems zeigen sein Potential zur "Uberwachung der Temperaturerh"ohung "uber die Koagulationsschwelle im Knochengewebe. Im letzten Teil dieser Arbeit wurde ein miniaturisierter Prototyp eines glasfaserbasierten Er:YAG Lasers mit OCT System entworfen und gebaut. Das miniaturisierte und integrierte Setup kann in der minimalinvasiven Laserchirurgie verwendet werden. Das entwickelte System konnte mit Hilfe der Echtzeit"uberwachung der Ablationstiefe durch das OCT mehrere vorausgeplante Ablationsschnitte (maximale Ablationstiefe von 5mm) durchf"uhren. Diese Arbeit war Teil des *Minimally Invasive Robot-Assisted Computer-guided Laser osteotomE* (MIRACLE) Projekts, welches zum Ziel hat ein Roboterendoskop f"ur die Durchf"uhrung laserbasierter Knochenchirurgie zu entwickeln.

2

CHAPTER 1

Introduction

1.1 Motivation

In recent years, different applications of lasers have been introduced in surgical and other medical treatments. The various properties of lasers – including high precision, high speeds, minimal or less invasiveness, and contactlessness – have drawn great interest in the medical field [1–4]. Dermatology, ophthalmology, dentistry, bone surgery, and oral surgery are among the medical specialties that most commonly use lasers [5–8]. In particular, lasers present distinct advantages in the medical field of bone cutting (osteotomy). They are able to perform accurate and nonlinear cuts while preserving the porous structure of bones during surgery in comparison to common mechanical tools [9–11]. In addition, due to the hemostatic effect of lasers, they can provide clean and dry operating areas by coagulating small blood vessels [12]. The advantages offered by laser technology have the potential to reinvent surgery, but there are still some challenges that need to be addressed.

Human beings are able to use visual, auditory, olfactory, and tactile modalities to collect information when interacting with the environment. In surgical procedures, the synergistic effects of haptic and visual feedback mainly enable optimal surgical outcomes [13]. In open laser surgery, laser devices block the surgeon's direct vision, and several start-stop-check procedures are required to monitor the process, which consequently prolongs the surgical procedure. Furthermore, in *minimally invasive surgery* (MIS), where a small endoscope is inserted into the human body through a small opening, surgeons cannot control the procedure based on immediate visual and haptic feedback. Due to these challenges, different feedback systems are required to provide real-time feedback to surgeons.

In laser osteotomy, feedback, and control regarding the depth and shape of the laser-induced cuts, dynamic changes in the surrounding tissue (e.g., temperature), and type of tissue are crucial [12, 14]. Visual feedback systems ensure that laser-induced cuts follow the planned shape and depth, and temperature feedback systems can prevent thermal damage to the surrounding tissue. In addition to depth and temperature feedback, tissue-

differentiation feedback to detect the type of tissue before ablation is crucial to achieving smart laser surgery [15]. A tissue sensor can improve the safety of laser surgery and lead to tissue-specific laser surgery.

Integrating real-time feedback systems and ablative lasers is thus vital to providing surgeons with the necessary information during surgery. In MIS settings, the importance of feedback systems is even more pronounced since the ablation site is located inside the human body. An important requirement for the feedback system in this project was its potential to be miniaturized to provide the information required during minimally invasive laser osteotomy.

To date, different techniques have been investigated for their potential to serve as feedback systems in laser surgeries. Photoacoustic imaging [16], ultrasound [17], magnetic resonance imaging (MRI) [18], optical coherence tomography (OCT) [19], and laser-induced breakdown spectroscopy (LIBS) [20] are among the promising technologies that could serve as feedback systems in laser surgery. While extensive research has been conducted on developing different feedback mechanisms during laser surgery, further investigations are required to develop an integrated feedback system in laser osteotomy.

This doctoral thesis aimed to develop long-range OCT as a visual feedback system for surgeons during laser osteotomy. The developed OCT system should be able to visualize the depth of the laser-induced cut (up to $\simeq$ 2–3 centimeters in air) in real time. Integrating the developed long-range OCT system (visual feedback) and tissue sensor (LIBS) with an ablative laser (*erbium-doped yttrium aluminium garnet* (Er:YAG)) was another part of this doctoral thesis. In addition, it aimed to investigate the potential of the OCT system to detect temperature increases in the bone during laser osteotomy. Finally, miniaturizing the integrated ablative laser and OCT system to achieve minimally invasive surgery was the final goal of this project.

1.2   Contribution

This thesis project was part of the Swiss flagship project MIRACLE (Minimally Invasive Robot-Assisted Computer-guided LaserosteotomE) at the University of Basel in Switzerland. The MIRACLE project aims to develop a robotic endoscope integrated with an ablative laser and feedback systems capable of performing deep bone ablation. The objective of the thesis project presented in this thesis was to develop a long-range OCT imaging system as a visual feedback system for the MIRACLE project. To achieve this goal, first, a free-space long-range Bessel-like beam OCT (BLB-OCT) system integrated with an Er:YAG laser was developed to monitor the ablation process in real time [21]. The developed BLB-OCT system achieved a DOF of 28.7 mm within the imaging range of 26.2 mm inside the laser-induced crater. In addition to the extended DOF, the BLB improved the imaging quality during bone ablation by reducing imaging artifacts (such as debris and water droplets). In addition to visual feedback (OCT), smart laser osteotomy also requires feedback regarding the type of tissue. A tissue sensor could improve the safety of surgery by preventing the ablation of the wrong tissue and by advancing the development of tissue-specific laser surgery. Here we utilized LIBS

to detect tissue types based on their spectra. A nanosecond *neodymium-doped yttrium aluminum garnet* (Nd:YAG) laser was added to the integrated Er:YAG laser and OCT system. This allowed us to achieve closed-loop tissue-specific laser osteotomy that avoids cutting unwanted tissue (such as bone marrow, fat, and muscle) [22].

In laser osteotomy (and in a similar way in conventional bone surgery), an irrigation system is commonly used to prevent thermal damage and rehydrate the bone. However, water molecules in the structure of the bone have a strong absorption peak at the wavelength of the Er:YAG laser (2.94 µm), so an excessive amount of water on the bone tissue can work as a protective layer and reduce ablation efficiency. Adding temperature feedback to the irrigation system could therefore improve ablation efficiency. This thesis investigated the potential of a calibrated phase-sensitive OCT for detecting temperature increases in the bone during laser osteotomy beyond the limits of the photothermal OCT and the thermal imaging of the optoacoustic system. The preliminary results of the developed phase-sensitive OCT system demonstrate its potential to serve as a temperature-feedback system [23]. The working principle of the developed temperature feedback is based on correlating the thermal expansion of the bone tissue (measured with an OCT system) with a corresponding temperature increase (measured with a thermal camera). To the best of our knowledge, there are no similar methods for detecting temperature increases in tissue during laser ablation. The unique advantage of the developed method is how it uses the OCT system to monitor both depth and temperature, which eliminates the need for another device and follows the requirements of the MIRACLE project. Miniaturizing the integrated Er:YAG laser and OCT system to monitor the depth of the laser-induced cuts was the final step of this thesis [24]. After completing these steps, the first prototype of the integrated ablative laser and OCT system was developed for the MIRACLE project.

1.3   Outline

This doctoral thesis consists of six chapters. Following this introductory chapter, Chapter 2 describes the background of the thesis project, including the medical basis of the project, laser surgery, image-guided laser surgery, the principles of the OCT system, phase-sensitive OCT, and miniaturized OCT systems. Chapters 3 to 6 present the publications were arising from this thesis. Each chapter begins with a brief introduction followed by the corresponding publications. Chapter 3 describes the developed long-range OCT system integrated with an Er:YAG laser (first paper). Chapter 4 concerns the development of the phase-sensitive OCT system for measuring temperature increases in bone tissue during laser osteotomy (second paper). Chapter 5 reports on a miniaturized ablative laser integrated with an OCT system (third paper). Finally, the thesis concludes in Chapter 6 with a discussion of the findings, an outlook on future research, and closing remarks.

Background

2.1 Laser surgery

Following the invention of the laser by Maiman in 1960 (Ruby laser) [25], it found its first medical application when Goldman used it in dermatology to treat skin melanoma. In the same year, Campbell demonstrated how a laser could be used to weld the detached retina of a rabbit [26]. Following these pioneering studies, researchers began investigating the effects of lasers on different biological tissues. Goldman, who is often called the "father" of lasers in medicine and surgery [27], listed the advantages of laser surgery over conventional surgery as follows [3]:

- Contactless surgery

- Highly sterile surgery

- Highly localized and precise microsurgery

- Clear field of view and easy access in confined areas

- Prompt healing with minimal postoperative swelling and scarring

- Apparent reduction in postoperative pain

- No electromagnetic interference on monitoring instrumentation

Although lasers offered quite a few advantages in the medical field, several shortcomings prevented further applications. In contrast to common surgical procedures, surgeons might not be able to control laser procedures based on haptic and visual feedback due to either fine laser-induced cuts or laser safety protocols. In laser surgery, the depths of laser-induced cuts have mainly been controlled by surgeons using manual surgical tools. This method of monitoring laser surgery limits the accuracy and requires several laser-pause-control steps since the direct view of the ablation site is blocked by the laser

system. Contactless, noninvasive, and accurate feedback systems are required to control laser-surgery procedures in real time. For instance, M.C Muckerheide suggested that technologies such as the distance-measurement system used in the Vietnam War could be integrated into laser systems to monitor the depth and surface of the tissue being cut [28].

Thanks to many breakthroughs, today, lasers have a wide range of applications in medical science, including in ophthalmology [29], dermatology [30], dentistry [31,32], bone surgery [14], and many other therapeutic and surgical procedures [2]. However, despite this wide range of applications, to the best of our knowledge, there are no closed-loop feedback control systems that can provide the necessary information during a procedure to achieve efficient and safe laser surgery.

2.2   Laser osteotomy

In the medical field of bone cutting (osteotomy), lasers present a means to address the drawbacks of traditional mechanical tools. These drawbacks include bacterial contamination, limited cutting geometry, and low precision. Lasers are able to perform high-precision and nonlinear cuts remotely [11,33,34]. They thus have the potential to reinvent bone surgery as we know it. Among the different types of lasers, the Er:YAG laser has been demonstrated to produce efficient ablation in hard tissue with minimum collateral damage [11,35,36]. However, developing feedback systems is crucial to achieving efficient and safe laser surgery [15].

2.3   Feedback systems for laser osteotomy

To date, several techniques have been investigated for their potential as feedback systems in laser osteotomy. Since the main goal of laser osteotomy is to cut the bone in the desired shape and depth, a visual feedback system that can monitor and control the ablation procedure is crucial [37]. The presence of different types of tissue in bone structures underscores the importance of a method for accurate tissue differentiation in tissue-specific laser surgery [38]. Finally, due to the heat-based interaction of the laser and tissue, temperature feedback could help prevent thermal damage to the surrounding tissue [39]. The following section discusses the systems and technologies required to provide such feedback in laser osteotomy.

2.3.1   Feedback: depth monitoring

The lack of depth feedback is considered one of the main technical obstacles to the medical applications of lasers. A depth-monitoring system must be able to monitor the depth of a cut remotely, noninvasively, in high resolution, and in real time. By definition, real-time depth monitoring is when the acquisition rate of the imaging system is faster than the repetition rate of the ablative laser. This would make it possible to stop the

ablative laser when it reaches the desired depth. To date, several optical and acoustic methods have been proposed for monitoring the depth and shape of cuts during laser surgery, including optoacoustic methods [40], inline coherent imaging [41], self-mixing interferometry [42], and OCT [43]. Among these methods, OCT and optoacoustic methods have demonstrated promising results. However, optoacoustic methods are considered a slightly invasive method for depth monitoring since detection depends on generating acoustic waves and the acquisition rate depends on the repetition frequency of the ablative laser. In recent years, several studies have shown that OCT can be used to noninvasively monitor the depth of laser-induced cuts in real time.

2.3.2 Feedback: temperature

Although laser ablation can create a localized heated region, the diffusion of heat to the adjacent tissue can cause thermal damage to it. In addition, in deep laser ablations of bone tissue, the nonuniformity of the spot size outside the Rayleigh length is considered to be an extra parameter that can induce thermal damage to the surrounding tissue. Heat deposition causes tissue temperature to rise, which may lead to hyperthermia (45 °C), coagulation (60 °C), vaporization (100 °C), carbonization (>100 °C), and melting (>300 °C) [44, 45].

Regarding the importance of safety, several methods have been investigated for their potential to monitor temperature rise in the surrounding tissue during laser surgery. Thermocouples [46], thermal cameras [47], fiber-optic sensors [48, 49], magnetic resonance thermal imaging (MRTI) [50], optoacoustic methods [51, 52], and photothermal OCT [53, 54] are among the various technologies utilized during laser surgery to determine and control the temperature of the tissues. Since the main aim is to measure the temperature of surrounding tissue remotely, MRTI, optoacoustic methods, and photothermal OCT have exhibited promising results in providing tomographic images of temperature rise. Current systems have been able to measure temperatures during laser coagulation. However, to the best of our knowledge, there are no imaging modalities for detecting the temperature rise of the tissue in laser-ablation regimes, which is the topic of this thesis.

2.4 Optical coherence tomography

Optical coherence tomography is a noninvasive, high-resolution, and high-speed imaging modality, which has a wide range of applications. The applications range from the nondestructive examination of museum objects [55] to industry [56] and medical applications [57]. In medical settings, OCT is a high-resolution interferometric imaging technique that acts as an "optical biopsy" [58], a real-time and noninvasive visualization of tissue microstructures and pathology. The applications of OCT in clinical settings can be classified into several categories: (1) for cases where a standard excisional biopsy is hazardous or impossible; (2) for cases where a standard excisional biopsy has a sampling error; (3) for the guidance of intervention procedures; and (4) for performing functional

measurements and imaging. In addition, OCT can be integrated with many medical devices such as catheters, endoscopes, laparoscopes, or needles [59].

2.4.1 History

The application of optical coherence tomography in medicine and biology has a long history. Although it has often been described as an optical analogue of ultrasound due to its similar working principle, in fact, it has its origins in femtosecond optics. The main concepts that ultimately led to the development of OCT started with early studies by Michel Duguay that suggested that high-speed optical gating could be used to "see inside" biological tissues [60]. Following the invention of OCT in 1991, it has achieved tremendous success.

2.4.2 Principle of OCT

The optical configuration of OCT is mainly based on the Michelson interferometer, which has a history that reaches back to 1881 [61] when Michelson introduced an apparatus to precisely determine the value of a meter in a luminous wavelength [62]. This method detects induced phase changes (due to displacement, etc.) based on intensity changes in terms of the known wavelength of the light source. Analogous to high-speed optical shutters that perform selective imaging, a broadband light source (low coherence) is used to image inside the tissue. Figure 2.1 shows a schematic of the Michelson interferometer. The illumination from the light source is first divided into two channels using a beam splitter, a reference arm, and a sample arm, where the reflected or scattered light from the sample in the sample arm interferes with the intact reference beam reflected from a mirror. These beams (from the reference arm and sample arm) are then recombined using a beam splitter and imaged by a detector.

By denoting the angle of the optical beams in respect to the optical axis as θ, the optical path difference between two beams can be described as:

$$\Delta_d = 2(d_2 - d_1)cos(\theta). \tag{2.1}$$

In equation 2.1, the constant 2 denotes that light travels twice the difference in distance between two mirrors. In addition, with consideration of the fact that the beam in channel 2 undergoes internal reflection only once and the beam in channel 1 undergoes it twice, equation (2.1) can be written as:

$$m\lambda = 2(d_2 - d_1)cos(\theta) \quad (m = 0, 1, 2, 3, ...) \quad \text{destructive interference}$$

$$(m + 1/2)\lambda = 2(d_2 - d_1)cos(\theta) \quad (m = 0, 1, 2, 3, ...) \quad \text{constructive interference} \tag{2.2}$$

where λ denotes the wavelength of the light source. Equation 2.2 shows that the difference in distance between the two mirrors can be detected with an accuracy of $\lambda/2$. This interference pattern is visible within the temporal coherence length, which is defined as [63]:
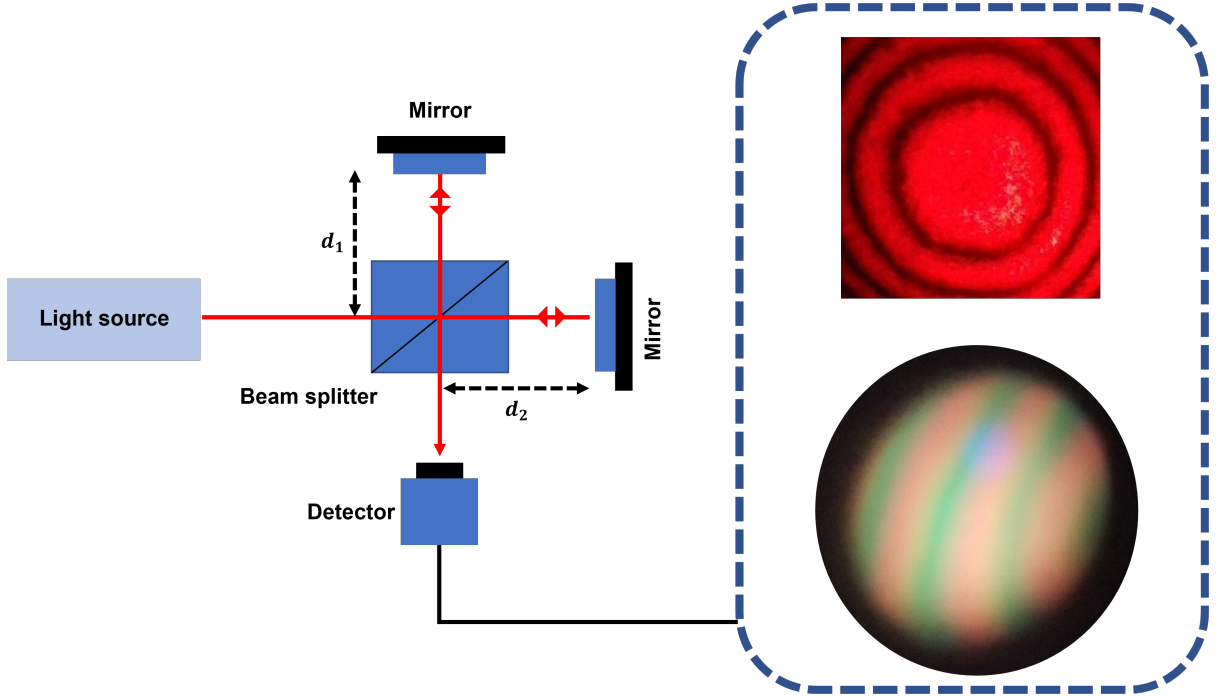
Figure 2.1:   Schematic of the Michelson interferometer. The top figure: the interference of the He-Ne laser; and the bottom figure: the interference of white light.

$$l_c = c\tau_c \approx \frac{\lambda_0^2}{\Delta\lambda}. \tag{2.3}$$

In equation 2.3, c represents the speed of light, τ_c is the coherence time (the time interval within the phase of the optical wave is usually predictable), λ_0 is the central wavelength, and $\Delta\lambda$ defines the spectral bandwidth of the light source.

According to the working principle, there are two categories of OCT: *time-domain OCT* (TD-OCT) and *Fourier-domain OCT* (FD-OCT))(Fig. 2.1). TD-OCT is the conventional method for OCT systems, in which the first OCT image is also produced using this configuration [60]. In TD-OCT, a power density of the interference signal is acquired using a single photodiode. In addition, a cross-sectional image of the sample is produced by scanning the reference mirror in the reference arm within the coherence length, where the amplitude of the successive interference signal corresponds to each scattering layer of tissue. Despite the breakthrough results introduced by TD-OCT, a lower *signal-to-noise ratio* (SNR) and lower speeds in comparison to the inherent motion of tissue limits its application [64].

Equation 2.2 denotes that if we keep the reference mirror stationary, changes in the wavelength (λ) can also produce the same effect. This introduces the principle of FD-OCT systems, which, in contrast to TD-OCT, require a scanning mirror and in which information about the entire depth is acquired by a signal shot of the laser. In addition, in contrast to conventional OCT, which measures the interference signal, FD-OCT mea-
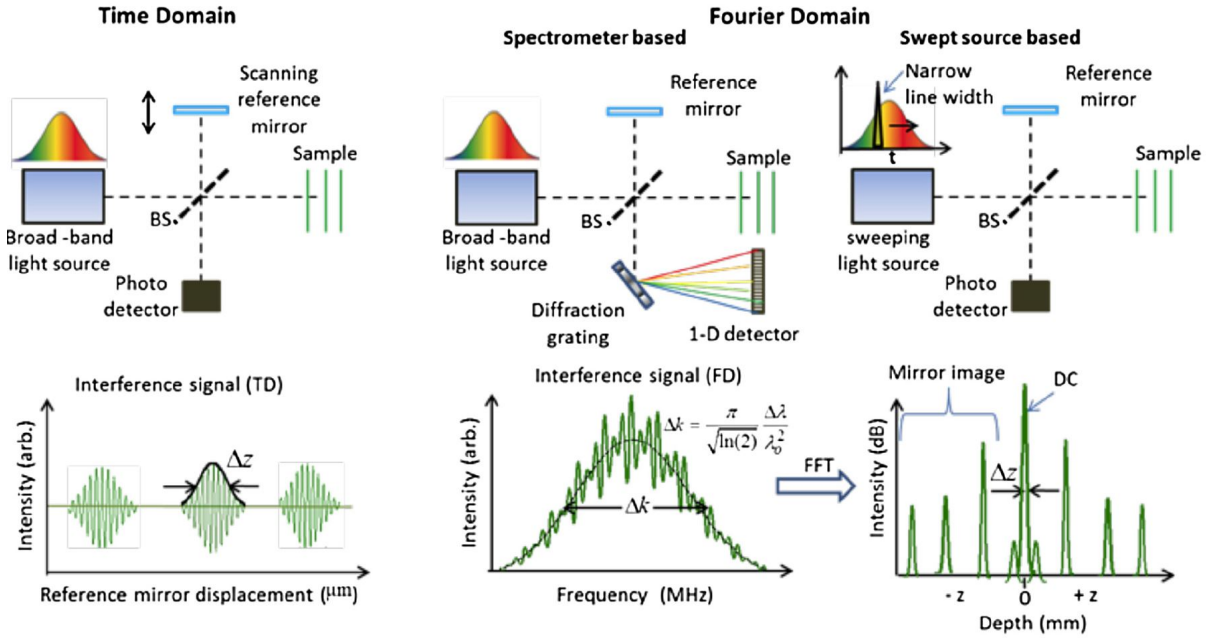
Figure 2.2:   Schematic of different OCT modalities. Based on the working principle, OCT can be divided into two groups, time-domain OCT (TD-OCT) and Fourier-domain OCT (FD-OCT). Furthermore, FD-OCT can also be divided into spectral-domain OCT (SF-OCT), and swept-source OCT (SS-OCT). Adapted with permission from [65] ©The Optical Society.

sures the spectrum of the interference signal [66]. Measuring the backscattered light in the Fourier domain could improve the sensitivity and speed of OCT imaging. Based on the method of accessing the frequency information of the tissue, FD-OCT can be divided into *spectral-domain OCT* (SD-OCT) and *swept-source OCT* (SS-OCT). In SS-OCT, similarly to TD-OCT, a single photodiode is used as the detection tool. In SS-OCT, time encodes spectral information by sweeping a narrow line-width laser through a broad optical bandwidth [67]. A broadband light source is utilized in SD-OCT, and the interference spectrum is directed toward a spectrometer. In the spectrometer, the interference spectrum is resolved into its spectral components, and each is measured separately.

Based on the advantages of FD-OCT in producing high-speed imaging, different scanning protocols have been developed to take advantage of these features to yield volumetric images. Figure 2.3 presents the scanning protocol for acquiring volumetric images. A one-dimensional (A-scan) signal is the unit of the volume image in the OCT system, which produces a cross-sectional image (B-scan) by scanning the OCT beam in a transverse direction. Acquiring adjacent B-scans makes it possible to produce a volumetric OCT image (Fig. 2.3).
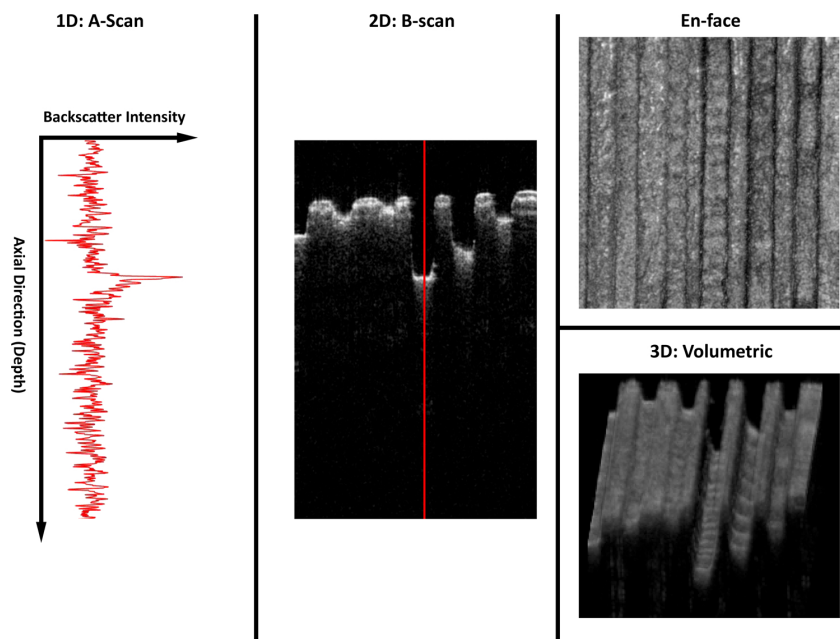
Figure 2.3: Schematic of the OCT scanning protocol. From left to right: 1D depth profile (A-scan), B-scan, acquired A-scans in the transverse direction, series of B-scans to produce a volumetric image, and en face OCT images.

Imaging parameters in OCT

One of the unique advantages of OCT is that the axial and lateral resolutions of the imaging system are defined independently. The axial resolution is defined by the spectral properties of the light source, and the lateral resolution is defined by the imaging properties of the optical lens. The axial resolution, lateral resolution, imaging range, and depth of focus are defined respectively as [68]:

$$\text{axial resolution}: \quad \Delta z = \frac{2ln2}{n\pi} \times \frac{\lambda_0}{\Delta\lambda}, \tag{2.4}$$

$$\text{lateral resolution}: \quad \Delta x = \frac{4\lambda_0}{\pi} \times \frac{f}{d}, \tag{2.5}$$

$$\text{depth of focus}: \quad n \times \frac{\pi\Delta x^2}{\lambda_0}, \tag{2.6}$$

$$\text{imaging range}: \quad z_{max} = \frac{\lambda_0^2}{4n\delta\lambda}. \tag{2.7}$$

Where λ_0 is the central wavelength of the light source, $\Delta\lambda$ is the spectral bandwidth, f is the focal length of the lens, d is the size of the incident beam on the lens, n is the refractive index of the sample, and $\delta\lambda$ is the wavelength-sample spacing following digitization [66].

2.4.3   Miniaturized OCT

OCT fills the gap between high-resolution microscopy and whole-body imaging techniques [69]. One technical drawback of OCT in comparison to other imaging modalities is its limited imaging range inside biological tissue due to the strong optical attenuation of biological tissue. This technical drawback limits its application in directly accessing internal organs from outside the body. However, since OCT is a fiber-based imaging technology, it has the potential to be miniaturized and used in endoscopic systems to access the internal organs of the human body. The first demonstration of in vivo endoscopic OCT was done by Tearney et al. in 1997 using a 1 mm fiber-optic catheter to image the *astrointestinal* (GI) and pulmonary tracts of a rabbit [70]. Following this study, endoscopic OCT has become a critical component in enabling high-resolution tomographic imaging of internal organs [71].

In recent years, various OCT probes have been developed, which, based on their design, can be divided into two groups: forward-viewing and side-viewing probes [71,72]. Figure 2.4 presents the design of the endoscopic sample arm of the OCT system. A side-viewing endoscope is more suited for surveying a large area of a luminal organ, while a forward-viewing endoscope is generally more suited for image guidance in biopsies, device placement, or treatments in which sufficient space between the OCT probe and the sample surface is needed.
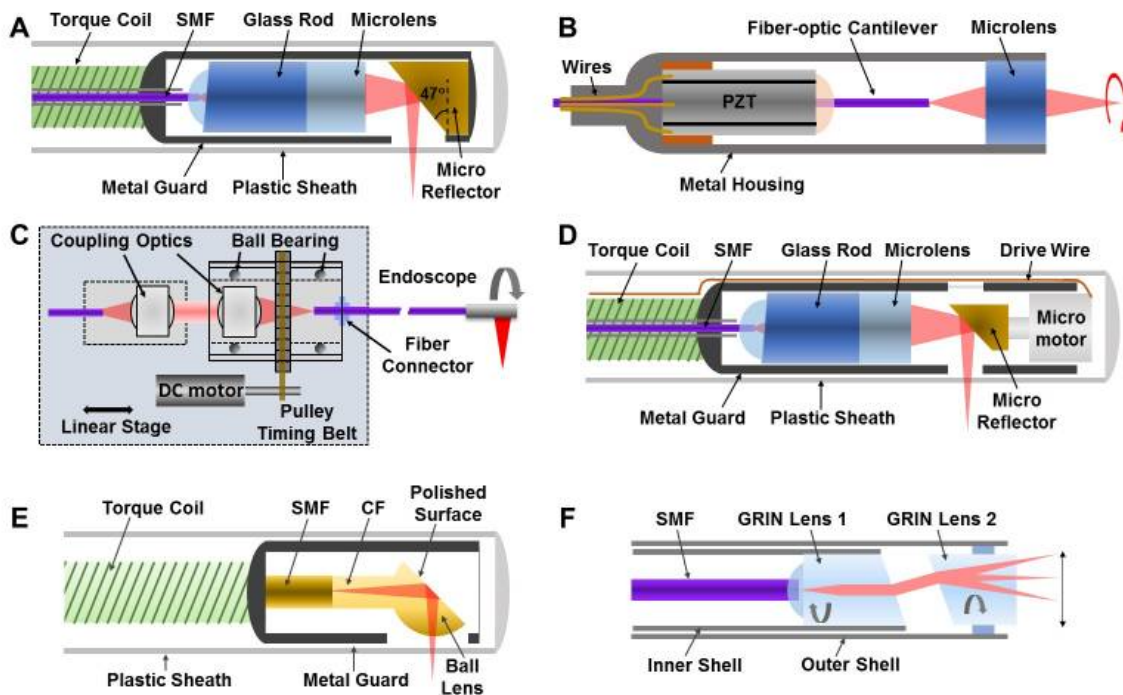

Figure 2.4: Schematics of a side-viewing OCT system (A, C, D, F). Schematics of forward-viewing OCT systems (B, F). Adapted with permission from [71] ©The Optical Society.

2.4.4   Photothermal OCT

During a temperature rise in a material, the kinetic energy of atoms increases, and the atoms vibrate and move, which results in a greater average separation of the atoms and thermal expansion [73]. Due to the high accuracy of interferometric methods, they have been utilized to measure the induced thermal expansion of tissue [74,75]. Early research on detecting the thermal expansion of samples using a Michelson interferometer was performed by attaching a mirror to the sample. This made it possible to determine the thermal expansion of tissue by detecting displacement and its corresponding temperature value during controlled heating of the sample. This method can be used to detect the coefficient of the linear thermal expansion of tissue regardless of its optomechanical properties. Equation 2.8 illustrates the correlation of the linear coefficient of thermal expansion with temperature changes and displacement:

$$\alpha = \frac{n\lambda}{2L_0 \Delta T} \; . \tag{2.8}$$

In equation 2.8, L_0 is the initial thickness of the sample, n is the number of fringe shifts in the interference pattern (displacement), α is the linear thermal expansion coefficient of the tissue, and ΔT is the measured temperature change [76].

Because of the promising results of interferometric methods in detecting temperature rise, researchers have investigated the potential of OCT, which is an interferometric imaging system, for measuring temperature rise in tissue. These studies have led to additional functionality of conventional OCT systems in detecting changes beyond its axial resolution [77]. The contrast in conventional OCT images resulted from measuring the amplitude of the interference signal in the Michelson interferometer. However, it is also possible to extract the phase of the interference signal to add extra contrast to OCT images. Phase-sensitive Fourier-domain detection enables contrast at extremely high imaging speeds. This high sensitivity offered by phase-sensitive OCT can detect the optical displacement of the target tissue beyond the axial resolution of conventional OCT systems. Consequently, optical path displacement (Δz) can be calculated from the value of the measured phase difference ($\Delta \phi$) [77]:

$$\Delta z = \frac{\lambda_0 \Delta \phi}{4\pi n}, \tag{2.9}$$

where λ_0 is the central wavelength of the light source, and n is the refractive index of the targeted sample. Using this principle, *Adler et.al* measured the modulation frequency and corresponding displacement of the attached piezoelectric transducer attached to a glass-cover slide as a sample. The measured displacement and frequency were measured as 5 kHz and $\pm 3 \, \text{nm}$, respectively [77].

Equations 2.8, and 2.9 denotes that through detecting the photothermal expansion of tissue and an understanding of linear thermal expansion and the optomechanical properties of tissue, one can predict temperature rise in a sample. The photothermal expansion of tissue can be described as the expansion of tissue due to the absorption of laser radiation (pulse, *continuous wave* (CW)). These changes in the temperature of tissue can

result in changes in the refractive index and thermoelastic surface displacement [78]. Measuring and controlling the corresponding temperature changes during laser therapy or surgery can reduce the risk of thermal damage. Figure 2.5 shows the photothermal expansion of bone during laser osteotomy using an Er:YAG laser. In Figure 2.5, (a) is the B-scan OCT image, and (b) is the corresponding M-mode OCT image over the time of laser ablation (4.1 seconds). The zoomed version is presented in Figure 2.5(c), where the photothermal expansion of tissue resulting from each pulse is visible.
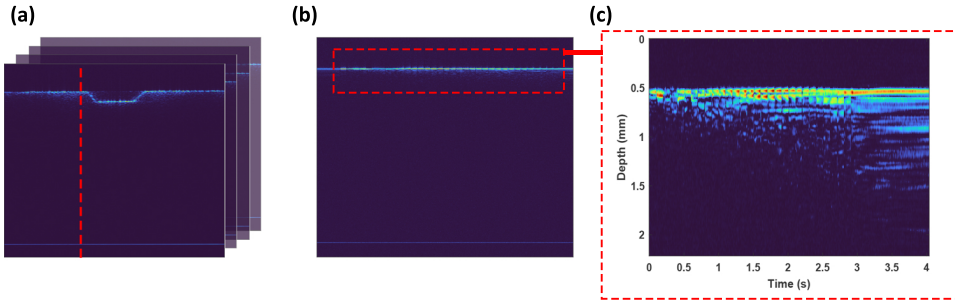

Figure 2.5:   Photothermal expansion of bone tissue during laser osteotomy with an Er:YAG laser. (a) B-scan image, (b) M-mode image acquired over the time of laser ablation, and (c) zoomed version of M-mode with visible photothermal expansion of the tissue.

The working principle described above has been used to measure the photothermal expansion of tissue with an OCT system. The net displacement on the surface of the tissue can be defined as [79]:

$$\Delta OPL(r) = \int_{L_0}^{L} n(T, r) dl. \tag{2.10}$$

In the equation 2.10, L_0 is the initial thickness, and L is the expanded thickness of the tissue. Therefore, the photothermal expansion can be defined as a summation of the changes in *optical path difference* (OPD). To date, several studies have investigated different methods for correlating temperature changes and changes in OPD measurements with OCT systems [53,80,81]. Photothermal OCT faces several challenges in measuring temperature rise in tissue beyond the coagulation threshold of the tissue. For instance, as mentioned with regard to the optoacoustic temperature-measurement method, there is a nonlinearity in the Grüneisen parameter as well as changes in the optical properties of the tissue (absorption and scattering coefficients) that reduce the accuracy of temperature measurements [82]. Due to the nonhomogeneous structure of biological tissue, changes in the optomechanical properties of the tissue will reduce the accuracy of photothermal OCT, just as they reduce the accuracy of optical measurement methods. That is why we investigated the potential of using phase-sensitive OCT to measure temperature rise during laser ablation.

Real-time depth monitoring and tissue differentiation during laser osteotomy

This chapter contains two publications. Feedback systems are essential during laser surgery to provide real-time feedback for the surgeon in real-time. In the first publication, visual feedback, and in the second publication, integrated visual feedback and tissue sensor with an Er:YAG laser is presented.

3.1 Real-time visual feedback

Our development of a long-range Bessel-like beam OCT system integrated with an Er:YAG laser as real-time visual feedback during laser osteotomy is presented in this section. The developed long-range BLB-OCT demonstrated supreme advantages compared to monitoring the depth of laser-induced cuts during laser osteotomy, which is accompanied by the generation of debris and water droplets.

Publication: Hamidi, A., Bayhaqi, Y. A., Canbaz, F., Navarini, A. A., Cattin, P. C., and Zam, A. (2021). Long-range optical coherence tomography with extended depth-of-focus: a visual feedback system for smart laser osteotomy. Biomedical Optics Express, 12(4), 2118-2133.

Long-range optical coherence tomography with extended depth-of-focus: a visual feedback system for smart laser osteotomy

ARSHAM HAMIDI,[1,4] **YAKUB A. BAYHAQI,**[1] **FERDA CANBAZ,**[1] **ALEXANDER A. NAVARINI,**[2] **PHILIPPE C. CATTIN,**[3] **AND AZHAR ZAM**[1,5]

[1]*Biomedical Laser and Optics Group (BLOG), Department of Biomedical Engineering, University of Basel, CH-4123 Allschwil, Switzerland*
[2]*Digital Dermatology, Department of Biomedical Engineering, University of Basel, CH-4123 Allschwil, Switzerland*
[3]*Center for medical Image Analysis and Navigation (CIAN), Department of Biomedical Engineering, University of Basel, CH-4123 Allschwil, Switzerland*
[4]*arsham.hamidi@unibas.ch*
[5]*azhar.zam@unibas.ch*

Abstract: This work presents a long-range and extended depth-of-focus optical coherence tomography (OCT) system using a Bessel-like beam (BLB) as a visual feedback system during laser osteotomy. We used a swept-source OCT system ($\lambda_c = 1310$ nm) with an imaging range of 26.2 mm in the air, integrated with a high energy microsecond Er:YAG laser operating at 2.94 µm. We demonstrated that the self-healing characteristics of the BLB could reduce the imaging artifacts that may arise during real-time monitoring of laser ablation. Furthermore, the feasibility of using long-range OCT to monitor a deep laser-induced incision is demonstrated.

1. Introduction

Osteotomy is a surgical intervention involving cutting, etching, shaving, and/or chipping of the bone. The most common osteotomy methods apply mechanical stress to the surface of the bone, using saws, drills, and chisels [1,2]. In addition to practical difficulties, mechanical trauma, broad cuts, excessive heat generation, and bacterial contamination are among the main risks associated with using conventional instruments for osteotomy [3]. Laser technology was introduced to overcome the limits of the mechanical tool used during surgery. Laser osteotomy is a contactless and potentially minimally invasive technology for bone surgery, providing freedom along with the cutting geometry and high precision [4–8]. However, one technical drawback of using lasers for osteotomy is the lack of depth feedback and the missing feedback in the type of tissue being cut currently [9]. Without this information, there is a risk of damaging the critical structure in the vicinity. Thus, a real-time feedback system is needed to guide the ablative laser during surgery. To date, several optical and acoustics methods have been proposed to monitor the depth and shape of the cuts during laser surgery [10–17].

Photoacoustic tomography is an imaging technique based on the generation and time-resolved detection of optoacoustic waves. These optoacoustic waves originate from the interaction of a short-pulse ablation laser and biological tissue [18,19]. Shockwaves emanate from the ablation spot; consequently, measuring the time-of-flight of these shockwaves can present a one-dimensional (1D) depth profile of the incision. Remote detection of shockwaves using air-coupled transducers shows a reliable sensitivity, suitable for real-time monitoring of the incision depth [14]. Using an air-coupled transducer, Landa FJO et al. could monitor the 1D depth profile of an 8 mm deep incision in osseous tissue. Furthermore, three-dimensional (3D)

localization of the laser cut (ex-vivo) was achieved by using an array of ultrasound detection elements [10]. This method robustly and accurately tracked incisions up to 9 mm deep in bovine tissue. However, photoacoustic tomography is able to measure the depth of the incisions only after the tissue has been ablated and shockwaves generated.

Optical techniques are also capable of remotely and non-invasively monitoring the depth and shape of laser cuts in real-time. To date, several optical methods have been developed to monitor the ablation procedure, such as the linnik interferometer (using a femtosecond laser), the self-mixing interferometer, and inline coherence imaging [15–17]. The first report of monitoring using the OCT system during the ablation of a rat organ demonstrated the strength of using OCT to monitor the formation of ablation craters, carbonization, and thermal damage [11]. Subsequently, extensive effort has been made to improve the integrated OCT and laser ablation system to provide visual feedback for the surgeon during laser surgery.

OCT is a non-invasive, high resolution, and high-speed interferometric imaging modality capable of providing 3D images of the internal microstructure within biological tissues [20–22]. However, one inherent drawback of OCT is the inverse proportion between the depth-of-focus (DOF) and lateral resolution [23,24]. This issue is more pronounced in the Fourier-domain OCT, which measures the whole depth profile (A-scan) in a single shot [25]. To achieve a high lateral resolution within the imaging range, a DOF that is comparable to the imaging range of OCT is required. Several methods have been introduced to achieve a high lateral resolution over an extended DOF to resolve this dilemma [26–33]. One approach could be the generation of Bessel beams (BBs) using an axicon lens or pupil filters [34]. By utilizing diffraction-limited BBs extended DOF has been achieved while preserving the lateral resolution. One major drawback of BBs compared to the Gaussian beam at focus is the sidelobe artifacts that reduce the sensitivity [29]. Multiple aperture synthesis (MAS) has also demonstrated an extended DOF depth profile with a high lateral resolution. In this method, the A-scans were collected using distinctive apertures then coherently summed [27,28]. MAS is free from sidelobe artifacts and signal loss; however, the coherent summation of the A-scans reduces the imaging speed leading to an application limitation in real-time monitoring systems. Computational methods can also correct the defocus and optical aberration of the Gaussian beam while imaging a biological tissue to achieve a uniform lateral resolution within the imaging range [30,32]. Interferometric synthetic aperture microscopy (ISAM) computationally produces spatially uniform resolution regardless of the focus position by solving the inverse scattering problem [26]. Computational adaptive optics (CAO) corrects the induced aberration to achieve a high lateral resolution in the imaging range [33]. ISAM and CAO methods are computationally expensive and require a phase-stable acquisition of the consecutive depth profile.

The possibility of using fiber optics makes OCT even more interesting, particularly for minimally invasive clinical applications. In a free-space integrated setup, two approaches have been introduced to monitor the ablation site by OCT, one with an angled and one with a perpendicular view. The angled view is achieved by selecting different beam paths for the ablation laser and OCT laser [35,36]. The perpendicular view is accomplished by employing a dichroic filter to combine the OCT and the ablation laser beams on a coaxial path. Monitoring the ablation procedure with a perpendicular view can measure the cutting depth with higher accuracy than with an angled view, particularly for deep incisions. Several studies have yielded promising results with various configurations of fiber-based OCT setups to monitor the ablation progress. One novel method used a simplified setup, including a single laser source (1064 nm mode-lock fiber laser with a 10 MHz repetition rate and 20 ps pulse duration) and a beam splitter (instead of a dichroic filter) for both ablation and imaging [37]. The authors of the paper demonstrated a real-time depth profile of stainless steel with an A-line rate, axial resolution, and imaging range of 46 kHz, 16 μm, and 1 mm, respectively. Alternatively, several groups have reported all-fiber integrated laser ablation and OCT systems using a doubled-clad fiber (DCF). This configuration

allows for a coaxial beam path (delivery without using a dichroic filter), which reduces the size of the integrated setup [38,39]. In this configuration, the OCT laser beam was coupled to a single-mode core of a DCF, and a coagulation laser was delivered through the multimode first cladding. One drawback inherent to this configuration is the generation of multimodal crosstalk-induced artifacts on the images. Several methods have since been introduced in order to reduce these image artifacts [38,40,41].

Each method for monitoring the ablation depth has its own pros and cons. The imaging range of these systems is limited to less than 1 cm, and these systems are not able to monitor the incision cut where a deep incision is needed. A long-range visual feedback system is required to monitor ablation procedures when a deeper cut is required. Recently, the feasibility of using an akinetic laser source for a long-range OCT system was investigated [42,43]. To the best of our knowledge, the integration of a long-range, extended DOF OCT system with an ablation laser has not been reported yet. Furthermore, deep ablation of hard tissue presents challenges for any visual feedback system, as the debris generated and water droplets sprayed by the irrigation system are more pronounced, thereby reducing the image quality of the monitoring system.

In this paper, we present the process of integrating an Er:YAG laser and a long-range, swept-source OCT (SS-OCT) system to provide real-time visual feedback during laser osteotomy. We extend the DOF of the OCT system up to 28.7 mm using the Bessel-like beam (BLB) to meet the requirements for a long-range imaging system. We also showed that image artifacts that may arise during laser ablation could be reduced by using BLB in the OCT system due to the BLB's self-healing nature. This study also demonstrates the potential use of BLB-OCT as a feedback system for real-time monitoring of the laser ablation process.

2. Methods

2.1. Photothermal ablation of bone

The ablation mechanism of Er:YAG (2.94 μm) laser is known as photothermal ablation [9,44]. The ablation laser's wavelength overlaps with a strong absorption peak of water and hydroxyapatite around 3 μm. When the laser impinges the bone's surface, heat transfers to the water molecules present in the bone and increase the pressure in the bone's interstitial matrix [45,46]. The pressure build-up leads to an explosion and, consequently, the removal of the tissue. Water spray and high-pressure airflow are usually integrated with the Er:YAG laser to clean the ablation area and keep the temperature of tissue below the damage/carbonization threshold [47,48]. In this study, a microsecond-long pulse Er:YAG laser was used to ablate the bone.

2.2. Imaging artifacts during laser ablation

Laser osteotomy is followed by the generation of debris and bone fragmentations [49,50]. Water droplets (due to the irrigation system) also can cause imaging artifacts for the imaging system. As the laser interacts with the generated debris and water droplets, several optical effects can occur, such as absorption, scattering, diffraction, reflection, and refraction. Although the spectral bandwidth of the OCT system is selected according to the optical window of the biological tissue, water droplets surrounding the bone and the superficial layer of water on the bone can still degrade the quality of the OCT image. For this experiment, we used a sapphire window to protect the optical components against the debris and water droplets during laser osteotomy. However, accumulated debris on the sapphire window can block and scatter the OCT's laser. To demonstrate these artifacts, we used the shadowgraph imaging method to capture the generated debris and explosion of accumulated water inside the incision [51]. The Er:YAG laser and camera are synchronized. For the synchronization, the TTL trigger pulse of Er:YAG laser is connected to start the capture of the camera with a time-steps of 50 μsec. The energy level per pulse of the ablative laser was 220 mJ.

2.3. Experimental setup

2.3.1. Bessel-like beam

The zero-order BB is a solution to the scalar Helmholtz equation. The electrical field amplitude of the zero-order BB is given by [52]:

$$E(r, z) = A \, exp(ik_z z)J_0(k_r, r), \tag{1}$$

where J_0 is the zero-order Bessel function, and k_r and k_z are the radial and longitudinal components of the free-space wave vector ($k, \quad k = \frac{2\pi}{\lambda}$) respectively. Distinct advantages of non-diffractive BB include preserving the transverse resolution within the DOF and self-healing properties [34]. BBs have been proposed for use in combination with OCT because of their diffraction-free propagation and self-healing properties, which can improve the quality of OCT images in a scattering media [29,53–55]. This combination allows for an extended DOF beyond what is possible with a Gaussian beam. The most straightforward way to generate a BBs is to use an axicon lens with cone-shaped refractive material (or a reflective surface) to transform an incident plane wave into a self-interfering cone of light. This self-interference forms concentric fringes, as shown in Fig. 1. An ideal non-diffraction BBs carry an infinite amount of energy and exist over an infinite area; hence are not practical. However, BBs with z-dependent cone angles, Bessel-like beam (BLB), can overcome the limitation of the BBs [56]. BLB also demonstrates extended DOF and self-constructing; however, it exhibits slow diffraction during propagation [57]. For this study, we aimed to use BLB to extend the DOF of the OCT system and reducing the image artifacts due to the self-healing properties of BLB.
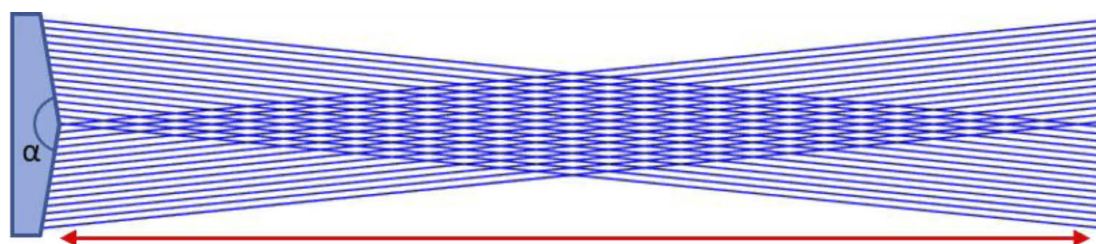

Fig. 1. Schematic of Bessel beam generation using an axicon for the plane wave. α shows the apex angle of the axicon. The red arrow delineates the region where the BB is generated, corresponding to the DOF of the BB.

Figure 2 shows the ray-tracing simulation of the sample arm designed for the OCT system, using the Zemax OpticStudio software. The collimated output of the fiber optics (a), with a beam diameter of 3.4 mm, was incident to an axicon lens with an apex angle of two degrees (b); it was followed by an achromatic lens (c). Galvanometer scanner (d) directed the ring-shaped beam beyond the axicon to the achromatic lens (e). Focusing this ring-shaped beam also generates self-interfering beams, which result in a second BLB with an extended DOF. Figure 2(f) illustrates the zoomed generated BLB behind the achromatic lens pairs. Figure 2(g) is corresponding to the cross-section of the computed point spread function using Fast Fourier Transform (FFT) at the center of BLB. The corresponding calculated DOF of the simulated BLB using Zemax OpticStudio software is 25.7 mm.

2.3.2. Integrated setup

Figure 3 gives an overview of the integrated system. The OCT system consisted of a fiber-based Michelson interferometer, a programmable akinetic swept-source laser (Insight Photonic Solution, Inc., Lafayette, Co, USA), and a balanced photodetector (PDB48xC-AC). In the sample arm of the OCT system, the collimated beam (after C1) was incident on an axicon lens (A1) with an
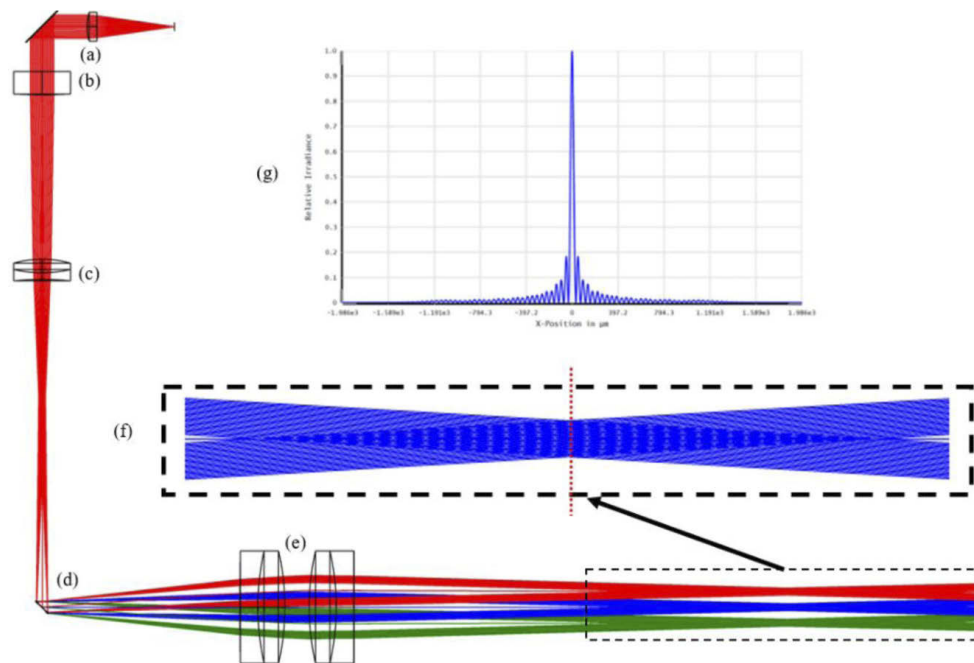
Fig. 2. Ray-tracing simulation calculated using Zemax OpticStudio software for the sample arm of the OCT system. (a) the collimator, (b) axicon lens with apex angle of two degrees, (c) achromatic doublet lens (f = 75 mm), (d) two-dimensional galvanometer scanner, (e) achromatic lens pairs (f = 100 mm). (f) Zoomed illustration of the generated BLB, (g) cross-section of the computed PSF at the focal plane of the achromatic lens pair, where dashed red line is shown in (f).
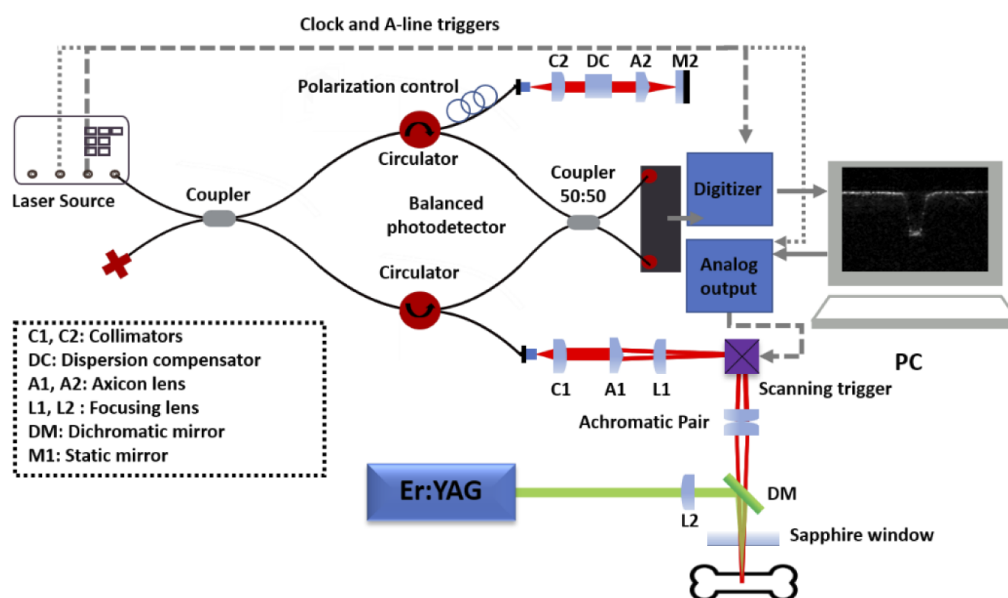
Fig. 3. Schematic of the integrated long-range and extended DOF OCT system for laser ablation. An Er:YAG laser is integrated into the sample arm of the OCT system using a dichroic filter.

apex angle of two degrees. An achromatic lens with a focal length of 75 mm (L1) was placed after the conical lens to focus the ring-shaped beam onto the Galvano scanner's relatively small size (3 mm). A two-dimensional galvanometer scanner directed the ring-shaped beam to an achromatic lens pair (1:1 with 100 mm effective focal length). Focusing the ring-shaped beam resulted in self-interfering beams, which generated the second BLB with an extended DOF.

In the reference arm, a dispersion compensator (DC) and an axicon lens (A2) with an apex angle of two degrees were placed after the collimator lens (C2) to compensate for the dispersion mismatch between the sample arm and the reference arm. The laser source in the OCT system operated at a central wavelength of 1310 nm, a spectral bandwidth of 61.5 nm, and an A-scan line rate of 111.61 kHz. The imaging range of the OCT system is equal to 26.2 mm in the air. In this experiment, we set the OCT system parameters in such a way as to capture B-scans, including 400 A-scans, which could provide a field of view of 4.3×4.3 mm^2. The captured raw data was processed using DC subtraction, averaging filter, and fixed-term noise subtraction. The Er:YAG laser (LITETOUCH by Syneron) was integrated with the OCT system, using a custom-made dichromatic filter that transmits the OCT's laser beam and reflects the beam of the Er:YAG laser. A 75 mm calcium fluoride (CaF$_2$) lens was utilized to focus the ablation laser onto the surface of the bone. A protective window was also placed after the dichroic filter to protect the optical elements from the debris as well as water droplets. As debris and/or water accumulate on the protective window, it could be exposed to high laser energy due to the absorption by debris and/or water. Thus, a window (e.g., sapphire, magnesium fluoride) with a high damage threshold is needed. In this experiment, we used a sapphire window with 2 mm thickness. The bone was placed within the focal region of both the Er:YAG and OCT lasers.

2.4. Irrigation system

A water jet was directed to the ablation spot to improve ablation efficiency. Using a water-based irrigation system prevents the carbonization of the bone during laser ablation and rehydrates the surface of the bone. A specially designed nozzle from Synova Laser MicroJet Technology was used in the experiments which can produce laminar water flow within a 50 μm diameter with 10-800 bar pressure [58]. Figure 4 demonstrates a photograph of the experimental setup. Er:YAG and OCT lasers were aligned to be in a coaxial path using a dichroic filter; in addition, a water jet (at 30 bar pressure) is aimed at the ablation spot to prevent carbonization. Since water has one of its highest absorption peaks around 3 μm, which overlaps with the operation wavelength of the Er:YAG laser, water accumulation on the surface of the sample reduces the efficiency of ablation. Therefore, we also used a continuous air pressure nozzle directed to the ablation spot to extract the accumulated water and debris from the laser-induced cut.
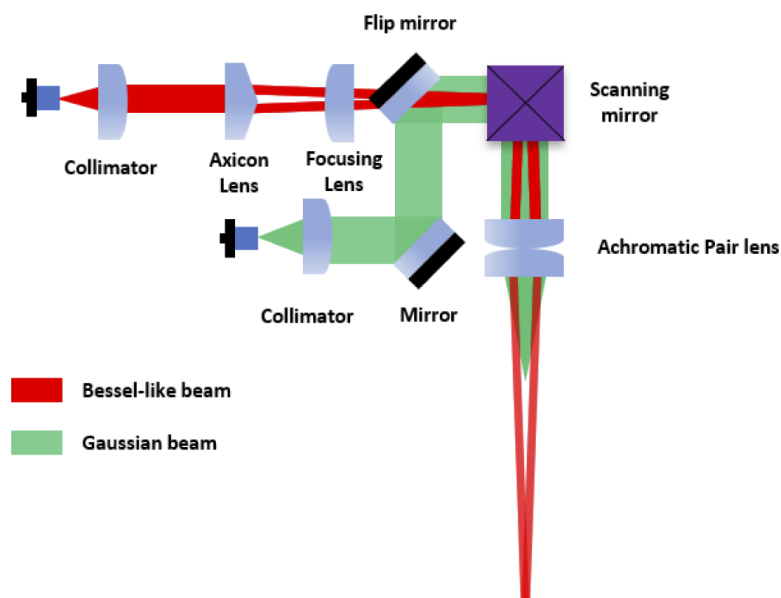
2.5. Comparison of performance of the BLB and Gaussian beam in the presence of imaging artifacts

Figure 5 demonstrates the schematic of the sample arm of the OCT system to compare the performance of BLB and Gaussian beam. In Fig. 5, red and green beam trajectories correspond to the BLB and Gaussian beam, respectively. To integrate the Gaussian beam, we utilized the same optical fiber and collimator which have been used in the BLB path (Fig. 4), and an additional flip mirror. We switched between these two arms by using a flip mirror. In addition, during the experiments, the corresponding sample arm was connected to the interferometer. To compare the performance of BLB and Gaussian beam, we created three different conditions of the protective window (sapphire window in Fig. 3): clean, covered with debris, and covered with water droplets. The 2D intensity profile of each beam after passing the protective window was recorded within the imaging range of the OCT system using a camera (BFLY-U3-23S6M-C, FLIR).

One inherent drawback of the Bessel beam is the signal-to-noise ratio (SNR) penalty due to the small fraction of power in the central lobe of the Bessel beam [59]. However, comparing the
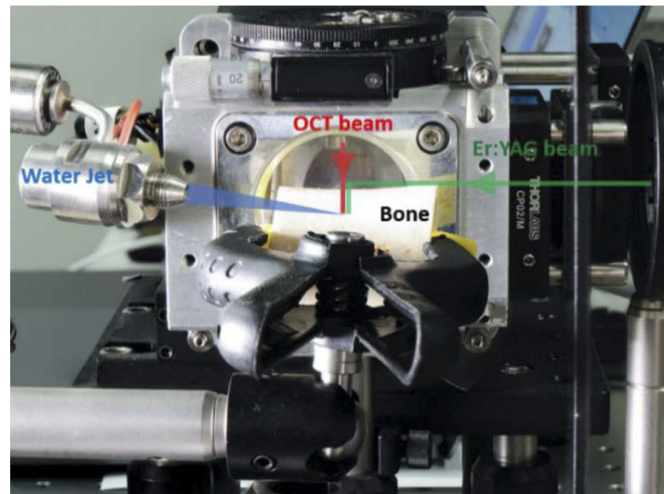
Fig. 4. Photograph of the setup used for ablation of femur bone sample. The OCT and Er:YAG lasers are combined using a dichroic filter. To avoid carbonization and enhance the efficiency of ablation, a water jet and a pressurized air nozzle are aimed at the ablation crater, respectively.

Fig. 5. Schematic of the sample arm of the OCT system for comparing the performance of BLB and Gaussian beam. In this experimental setup, switching between Gaussian beam and BLB is possible using the flip mirror.

SNR of the BB and Gaussian beam using the conventional method (placing a reflector instead of the sample) is not feasible for BLB mainly because the back-coupled signal in the BB case will include the contributions from the sidelobes. Therefore, this comparison was made by comparing the sensitivity of these beams. Illumination efficiency and collection efficiency for both sample arms were measured at different conditions of the protective window (clean, covered with debris, and covered with water droplets) by using the method described by Lee. et al. [60]. The incident beam power of 8 mW is measured by a power meter. For the BLB case, the collection efficiency was measured using a convential lens (LSM05, Thorlabs). The on-axis sensitivity of BLB in different conditions of the protective window was determined by subtracting the illumination efficiency and collection efficiency from the corresponding peak sensitivity of the Gaussian beam.

3. Results

3.1. Extending depth-of-focus of OCT using Bessel-like beams

Figure 6(a) illustrates the cross-sectional intensity profile of the BLB in the sample arm of the OCT system. The evolution of the BLB was recorded by a camera, with a step size of 0.5 mm in the propagation direction (z-direction). The white curve [Fig. 6(a)] indicates the corresponding variation of intensity of the central peak as a function of the propagation distance. The DOF of the BLB was measure as 28.7 mm (full width at half maximum (FWHM)), which exceed the imaging range of 26.2 mm in the experiment. Figures 6(b)–6(d) demonstrate the 2D intensity profiles of the BLB at $z = 20$ mm, $z = 40$ mm, and $z = 60$ mm with corresponding point spread function of 38.6 μm, 29 μm, and 26 μm, respectively.

3.2. Imaging artifacts

3.2.1. Debris

When ablative laser pulses are directed onto biological tissue, ablated particles are emitted above the tissue surface. Figure 7(a) demonstrates the generation debris with time-steps of 50 μsec after shooting an Er:YAG laser pulse to the surface of the bone. Figures 7(b) and 7(c) illustrate the window covered with debris. Figure 7(d) depicts the OCT beam with a Gaussian intensity distribution, which was obtained after the protective window [Fig. 7(d)].

3.2.2. Water droplets

Laser surgery using an Er:YAG laser system is usually integrated with a water spray. Figure 8(a) corresponds to the explosion of water accumulated inside the incision (time-steps are 50 μsec). Figures 8(b)–8(d) illustrate a Gaussian beam interaction with water droplets on the protective window. These images were acquired at different axial and lateral positions to demonstrate different artifacts induced by water droplets on the protective window.

3.3. Interaction of the BLB and Gaussian beam with debris and water droplets

Debris and water droplets generated during laser osteotomy pose significant challenges to the visual feedback system, mainly due to their interaction with laser light. These interactions may reduce the quality of the images collected by the OCT system. Note that, since the accumulation of water droplets and debris were random during laser ablation of the bone, it was not feasible to compare the performance of the BLB OCT and the Gaussian beam OCT in real-time monitoring of laser osteotomy. Therefore, these comparisons are made by using a protective window that was deliberately kept clean, covered with debris, and covered with water droplets.

To investigate the influence of debris and water droplets on the quality of the imaging system, we captured the 2D intensity profile of the BLB and Gaussian beam after the protective window. Since water droplets on the sapphire window were unstable due to movement or evaporation, we
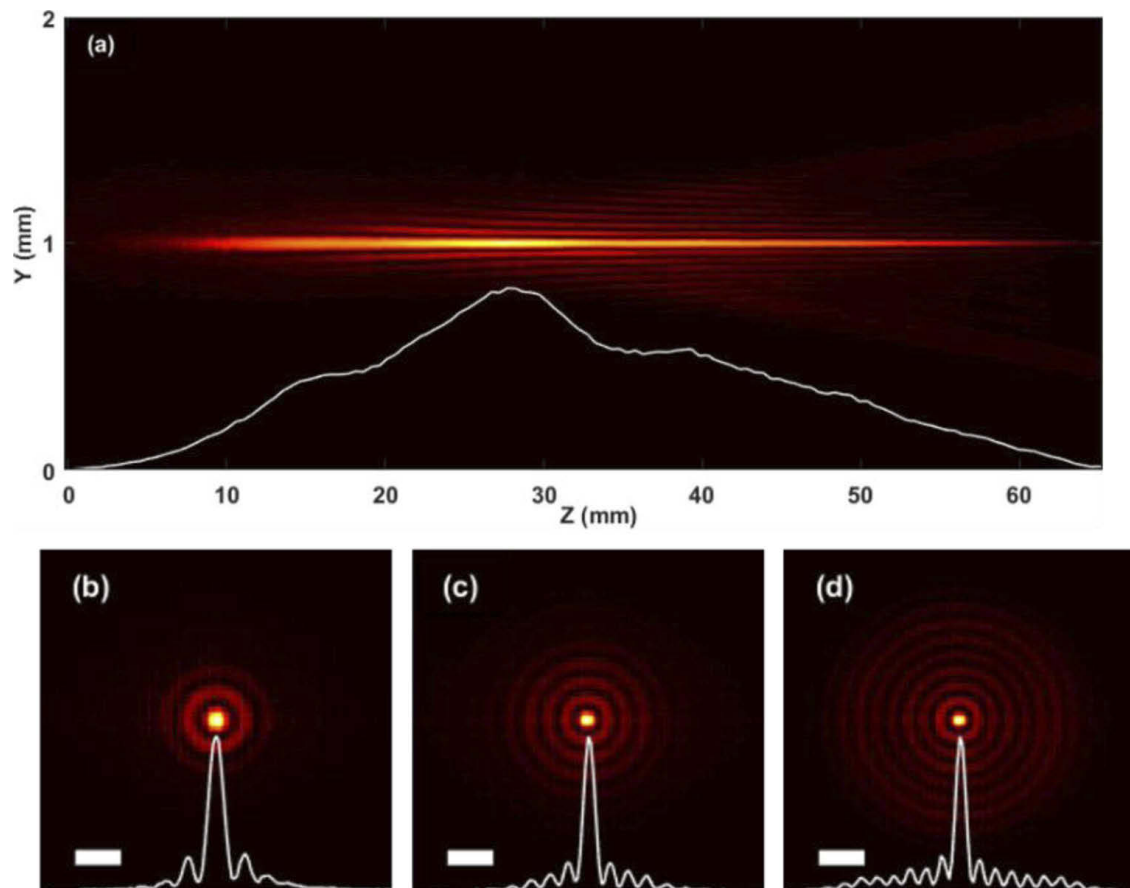
Fig. 6. (a) Measured cross-sectional intensity profile of the experimentally-generated BLB, and propagation is from left to right. The variation of the intensity profile of the central peak of the BLB over 65 mm propagation distance, where FWHM was 28.7 mm. Cross-sectional intensity image of the BLB at (b) z = 20 mm, (c) z = 40 mm, and (d) z = 60 mm. The point spread function of (b)-(c) is 38.6 µm, 29 µm, and 26 µm, respectively. The scale bar is 100 µm.

used a window with a hydrophobic coating to capture the intensity profile of the beam. Figure 9 illustrates the intensity profile variation with respect to distance from the focal plane for the three cases.

The three columns in Fig. 9 present the intensity profile of the BLB and Gaussian beam when it passed through a window covered with water droplets, covered with debris, and the clean window, respectively. Each raw represents the relative distance to the focal plane of the Gaussian beam and BLB. The interaction of the Gaussian beam and BLB with debris and water droplets on the surface of the protective window results in a distorted 2D intensity profile. However, BLB demonstrated superior performance in comparison to Gaussian beam due to the so-called self-healing properties.

To investigate the performance of the BLB and the Gaussian beam for monitoring the depth of ablation in laser osteotomy, lateral resolution and sensitivity of each beam have been compared. Figure 10 demonstrates the comparison of lateral resolution and sensitivity of the BLB and the Gaussian beam in different conditions of the protective window. First raw [Figs. 10(a)–10(c)] illustrates the measured lateral resolution for each experiment. In Fig. 10(a), the lateral resolution of 23 µm and 25 µm were measured for the BLB and Gaussian beam, respectively. Figures 10(b)–10(d) demonstrate the effect of the imaging artifacts on the lateral resolution of the Gaussian beam; however, the BLB showed approximately an invariant lateral
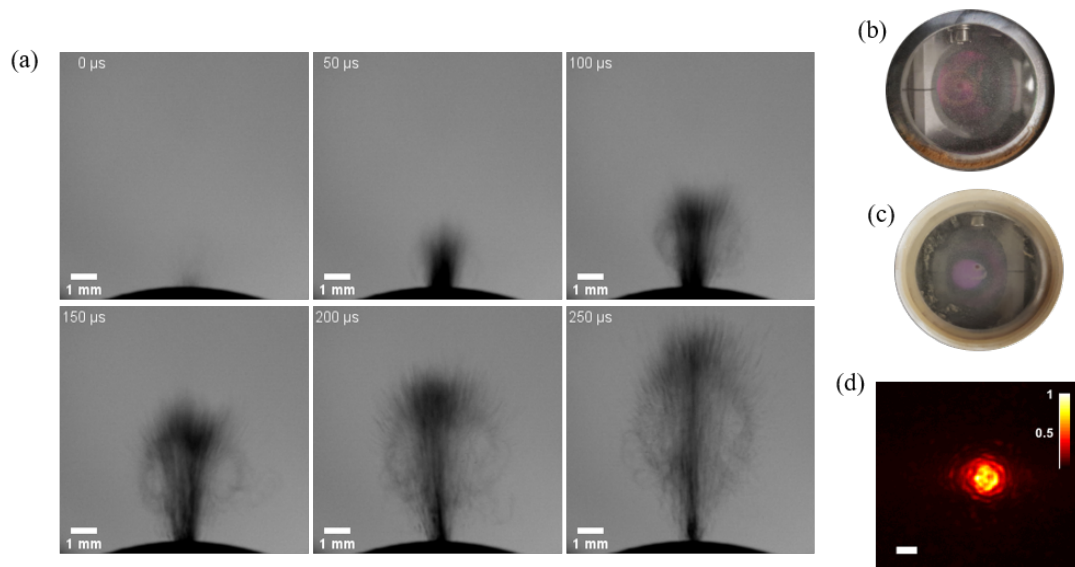
Fig. 7. (a) Debris formation over time, from the onset of an Er:YAG laser pulse onto hard tissue. These images are captured using shadowgraphy method. (b)-(c) Debris accumulated on the sapphire. (d) Intensity profile of the Gaussian beam after passing through the windows covered with debris (scalebar = 200 μm).
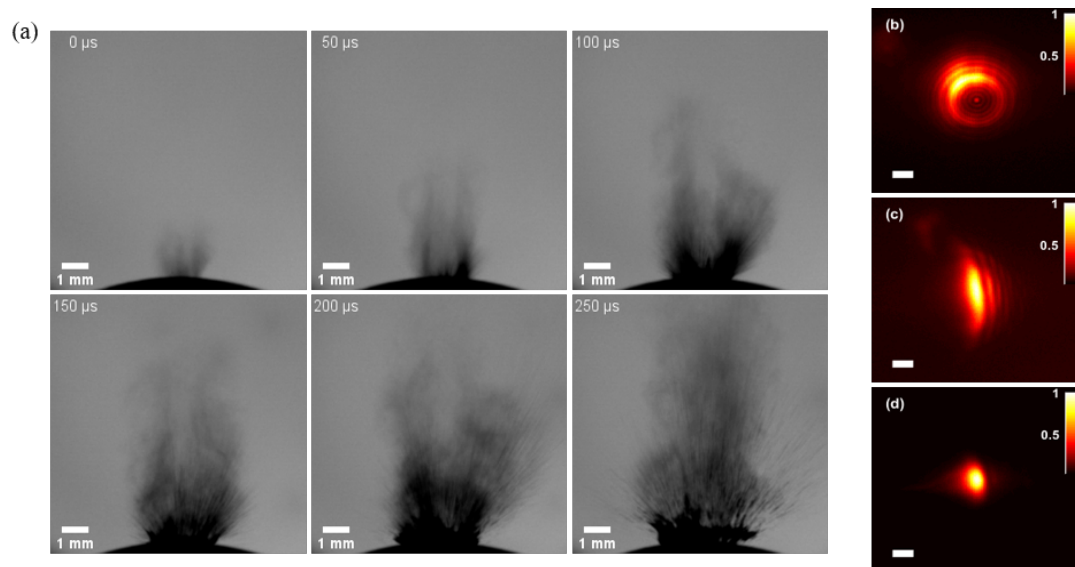
Fig. 8. (a) The explosion of water accumulated inside the cut after shooting Er:YAG laser pulse. These images are captured using the shadowgraphy method (time-steps are 50 μsec). (b)-(d) Intensity profile of the Gaussian beam after passing through the protective window covered with water droplets. The scale bar is 200 μm.
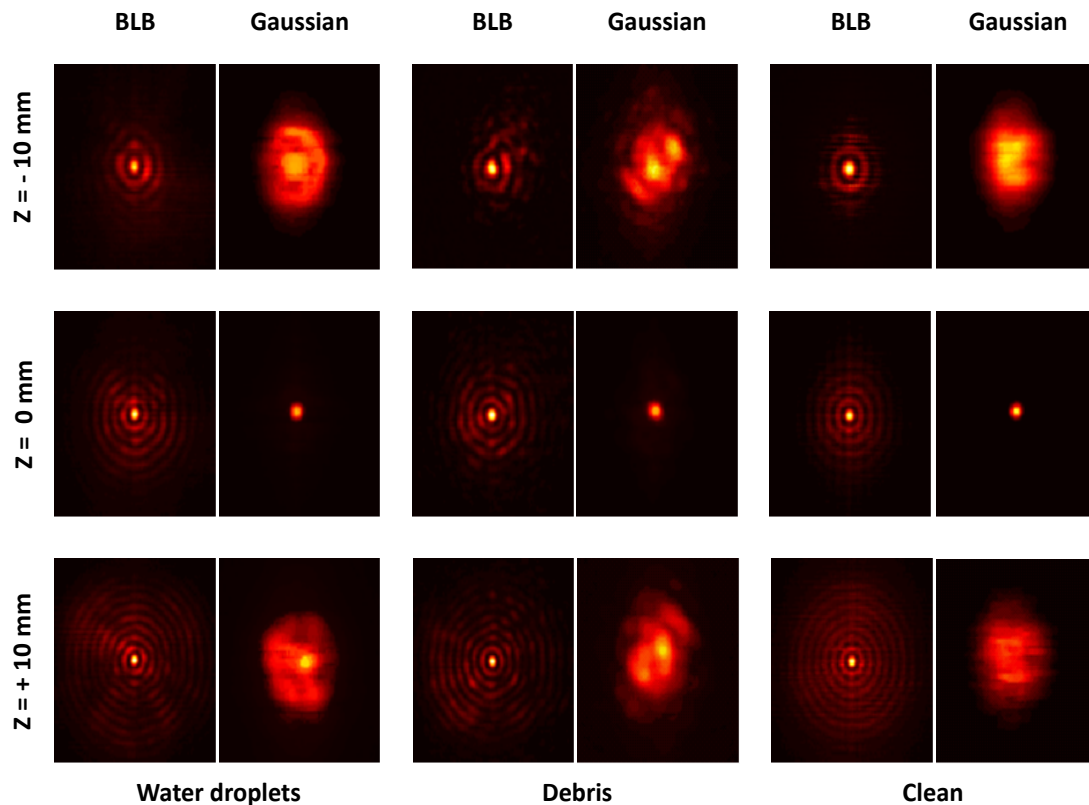
Fig. 9. Intensity profile of Bessel-like beam and Gaussian beam after passing through the protective window under three conditions: clean, covered with debris, and covered with water droplets. Each column represents one of these situations, starting from Z = -10 mm, to Z = 10 mm from the focus point. The size of the images is 1 mm × 1 mm.

resolution (less than 11 µm within 2.6 cm) in different condition of the sapphire window. The second raw in Fig. 10 demonstrates the measured sensitivity of the BLB and the Gaussian beam. For the Gaussian beam, on-axis peak sensitivities of 108 dB, 98 dB, and 82 dB were measured for a clean, covered with debris, and covered with water droplets, respectively. The sensitivity of the BLB was determined by subtracting the illumination efficiency and collection efficiency from peak sensitivity in each case. The SNR penalty of using BLB is visible in Figs. 10(d)–10(f). The higher sensitivity region of the Gaussian beam is localized over its DOF, while BLB shows a considerably higher sensitivity along with the imaging range.

Furthermore, the power ratio (ratio between the central peak and sidelobe) of the normalized intensity profile of BLB at the focus were measured as 0.21, 0.28, 0.37 in a clean protective window, covered with debris, and covered with water droplets, respectively. As it is visible in Fig. 11, the sidelobes of the BLB do not cause any significant artifacts during real-time monitoring of the laser osteotomy.

3.4. Real-time monitoring of laser ablation of bone

For this experiment, we placed a pig femur at the focal plane of the integrated BLB OCT and laser ablation system. The ablation laser's output energy and repetition frequency were 220 mJ and 1 Hz, respectively. To monitor the ablation procedure of the femur bone, we ran the OCT system continuously, starting before administering the first laser pulse to the end of the ablation procedure. Figures 11(a)–11(d) represent selected images captured within the imaging range of the OCT. Figure 11(d) shows that the ablative laser passed through the cortical line of the femur bone, reaching the surface of the cortical bone in the medullary cavity. Figure 11(e) shows the
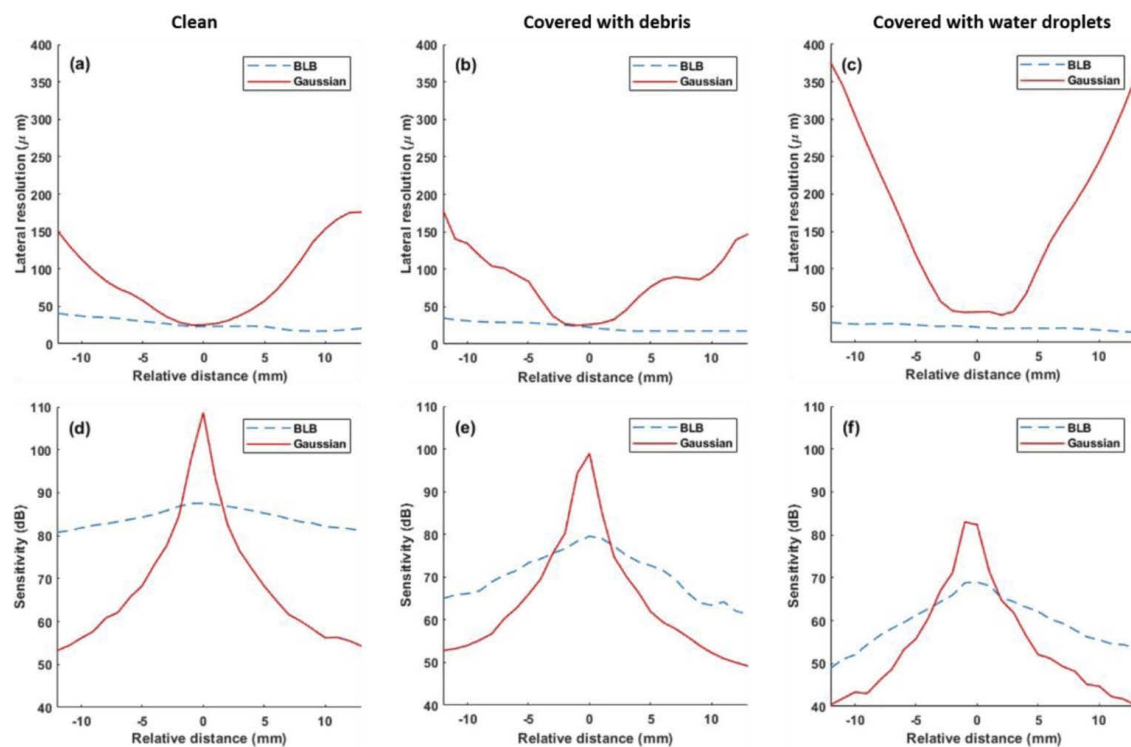
Fig. 10. Comparison of lateral resolution (a-c) and sensitivity (d-f) for Gaussian and BLB cases at different conditions of the sapphire window: clean [(a) and (d)], covered with debris [(b) and (e)], and covered with water droplets [(c) and (f)]. Gaussian beam and BLB are delineated with continuous red and dashed blue lines, respectively.

deepest point of the ablated cut with the OCT images presented. The depth of the incisions in Figs. 11(a)–11(d) is 0.5 mm, 1.57 mm, 2.53 mm, and 12.72 mm, respectively. The cutting width is measured as ∼ 0.56 mm. The time difference between Figs. 11(a)–11(d) is 51 seconds, which corresponds to 51 pulses of the Er:YAG laser. The thickness of the cortical line of the femur bone to the medullary cavity was 2.54 mm, and the diameter of the medullary cavity was 10.1 mm, which was measured with a caliper.
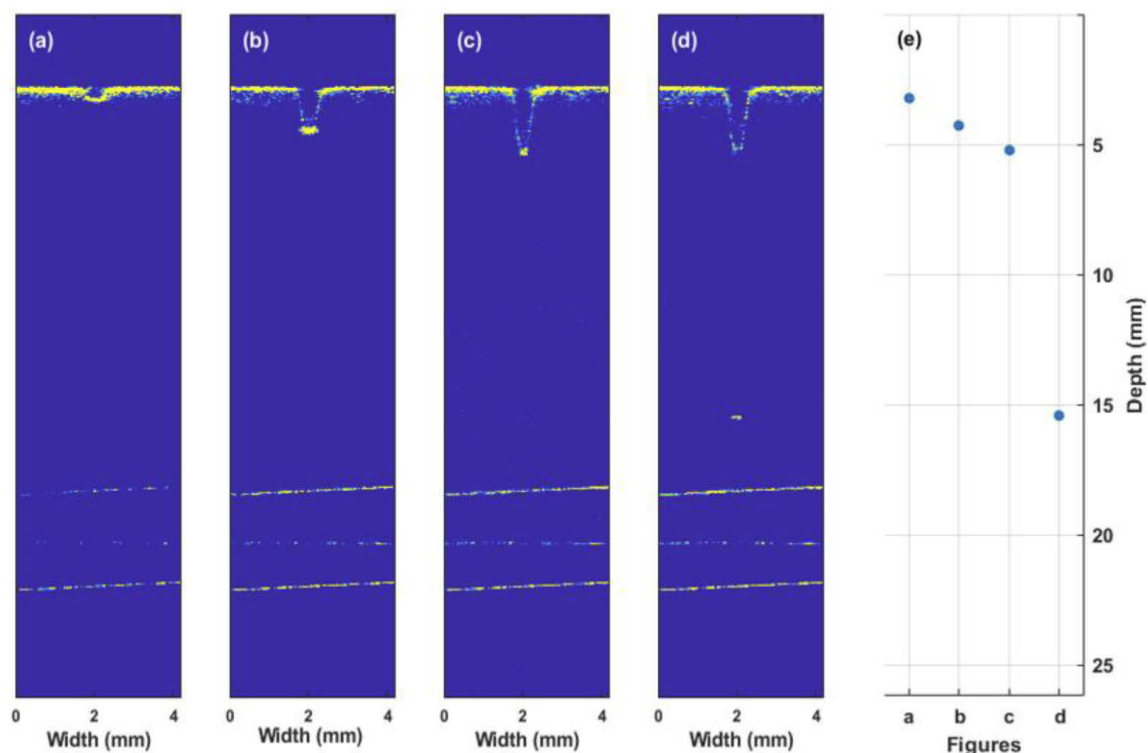
Fig. 11. Selected images during a laser ablation process of bone collected using the long-range and extended DOF OCT system. (a)-(d) real-time depth monitoring of laser ablation of the femoral bone. (d) In this image, the ablative laser cut through the cortical line of the femur bone and reached the surface of the cortical bone in the medullary cavity. (e) The measured depth of cuts within the imaging range of the OCT system.

4.   Discussion and conclusion

This study demonstrated the feasibility of using a long-range optical coherence tomography system to provide visual feedback during laser osteotomy. Laser osteotomy often generates image artifacts (especially in deep ablation) that hinder the OCT system; thus, we investigated the potential of a Bessel-like beam (BLB-OCT) to extend the DOF of the long-range OCT system and to improve the quality of acquired images by reducing the effect of such artifacts.

The proposed method offers some unique advantages over existing designs that employ a Gaussian beam in the OCT system to monitor the ablation procedure. A long-range imaging system can be used when deep laser-induced cuts (in order of cm) are required. Likewise, the most effective approach to reducing image artifacts is to place the sample further away from the protective window. Although this configuration is not practical for minimally invasive surgical procedures, a free-space integrated setup would benefit from the reduction of debris and water droplets that reach the protective window. Such a setup would require an optimized ablation laser with an extended DOF to perform a deep ablation, which is beyond the scope of this paper. In our configuration, just a fraction of the debris reaches the protective window. The debris cloud scatters laser light close to the sample's surface [61]. As can be seen from Fig. 10, the BLB-OCT shows a superior lateral resolution and sensitivity in comparison to the Gaussian beam within the imaging range, especially in the presence of imaging artifacts (accumulated debris and water droplets) on the protective window. However, it worth mentioning that the protective window needs to be cleaned in a long-term ablation. An additional feedback system that controls the irrigation system would enhance the quality of the OCT images further. Another approach would be the use of the OCT system as a feedback system for the irrigation system. Lastly, the proposed

method has the absence of a depth control system that can stop the ablative laser after reaching the desired depth of the incision.

Using a novel long-range extended DOF BLB-OCT system to provide visual feedback during laser ablation, we demonstrated real-time monitoring of laser osteotomy. Using the BLB-OCT, we demonstrated how self-healing property improves the quality of the OCT images in the case of debris and water droplet accumulation. We believe that the proposed BLB-OCT system has the potential to be used in smart laser osteotomy involving deep incisions. Controlling the irrigation system, miniaturizing this system, and providing depth control to be used in a minimally invasive device are of future interest.

Disclosures. The authors declare no conflicts of interest.

References

1. K. W. Baek, W. Deibel, D. Marinov, M. Griessen, M. Dard, A. Bruno, H. F. Zeilhofer, P. Cattin, and P. Juergens, "A comparative investigation of bone surface after cutting with mechanical tools and Er:YAG laser," Lasers Surg. Med. **47**(5), 426–432 (2015).
2. Y. Zhang, C. Wang, S. Zhou, W. Jiang, Z. Liu, and L. Xu, "A comparison review on orthopedic surgery using piezosurgery and conventional tools," Procedia Cirp **65**, 99–104 (2017).
3. G. K. Eyrich, "Laser-osteotomy induced changes in bone," Medical Laser Application **20**(1), 25–36 (2005).
4. M. Augello, C. Baetscher, M. Segesser, H.-F. Zeilhofer, P. Cattin, and P. Juergens, "Performing partial mandibular resection, fibula free flap reconstruction and midfacial osteotomies with a cold ablation and robot-guided Er:YAG laser osteotome (CARLO®)–A study on applicability and effectiveness in human cadavers," Journal of Cranio-Maxillofacial Surgery **46**(10), 1850–1855 (2018).
5. M. Ivanenko, M. Werner, S. Afilal, M. Klasing, and P. Hering, "Ablation of hard bone tissue with pulsed CO2 lasers," Medical Laser Application **20**(1), 13–23 (2005).
6. Y.-M. Lee, R. Tu, A. Chiang, and Y.-C. Huang, "Average-power mediated ultrafast laser osteotomy using a mode-locked Nd: YVO 4 laser oscillator," J. Biomed. Opt. **12**(6), 060505 (2007).
7. R. Mauceri, V. Panzarella, L. Maniscalco, A. Bedogni, M. E. Licata, A. Albanese, F. Toia, E. M. G. Cumbo, G. Mazzola, and O. Di Fede, "Conservative surgical treatment of bisphosphonate-related osteonecrosis of the jaw with Er, Cr: YSGG laser and platelet-rich plasma: a longitudinal study," BioMed Res. Int. **2018**, 1–10 (2018).
8. D. G. Panduric, I. B. Juric, S. Music, K. Molčanov, M. Sušic, and I. Anic, "Morphological and ultrastructural comparative analysis of bone tissue after Er:YAG laser and surgical drill osteotomy," Photomed. Laser Surg. **32**(7), 401–408 (2014).
9. S. Stübinger, "Advances in bone surgery: the Er:YAG laser in oral surgery and implant dentistry," Clin., Cosmet. Invest. Dent. **2**, 47–62 (2010).
10. E. Bay, X. L. Deán-Ben, G. A. Pang, A. Douplik, and D. Razansky, "Real-time monitoring of incision profile during laser surgery using shock wave detection," J. Biophotonics **8**(1-2), 102–111 (2015).
11. S. A. Boppart, J. Herrmann, C. Pitris, D. L. Stamper, M. E. Brezinski, and J. G. Fujimoto, "High-resolution optical coherence tomography-guided laser ablation of surgical tissue," J. Surg. Res. **82**(2), 275–284 (1999).
12. A. Hamidi, Y. A. Bayhaqi, F. Canbaz, A. Navarini, P. C. Cattin, and A. Zam, "Imaging photothermal-induced expansion of bone during laser osteotomy by phase-sensitive OCT: preliminary results," in *Biomedical Spectroscopy, Microscopy, and Imaging*, (International Society for Optics and Photonics, 2020), 113590 K.
13. H. N. Kenhagho, I. Sugiarto, R. Guzman, P. Cattin, and A. Zam, "Contact-free Crater Depth Monitoring Using Measured Acoustic Shock Waves for Smart Laser Surgery Applications: Preliminary Result," in *2019 International Conference on Radar, Antenna, Microwave, Electronics, and Telecommunications (ICRAMET)*, (IEEE, 2019), 118–121.
14. F. J. O. Landa, X. L. Deán-Ben, F. M. de Espinosa, and D. Razansky, "Noncontact monitoring of incision depth in laser surgery with air-coupled ultrasound transducers," Opt. Lett. **41**(12), 2704–2707 (2016).
15. F. P. Mezzapesa, L. Columbo, M. Brambilla, M. Dabbicco, A. Ancona, T. Sibillano, F. De Lucia, P. M. Lugarà, and G. Scamarcio, "Simultaneous measurement of multiple target displacements by self-mixing interferometry in a single laser diode," Opt. Express **19**(17), 16160–16173 (2011).
16. P. J. Webster, L. G. Wright, K. D. Mortimer, B. Y. Leung, J. X. Yu, and J. M. Fraser, "Automatic real-time guidance of laser machining with inline coherent imaging," J. Laser Appl. **23**(2), 022001 (2011).
17. A. Zakharov, M. Volkov, I. Gurov, V. Temnov, K. Sokolovski-Tinten, and D. Von Der Linde, "Interferometric diagnostics of ablation craters formed by femtosecond laser pulses," J. Opt. Technol. **69**(7), 478 (2002).
18. T. Juhasz, X. H. Hu, L. Turi, and Z. Bor, "Dynamics of shock waves and cavitation bubbles generated by picosecond laser pulses in corneal tissue and water," Lasers Surg. Med. **15**(1), 91–98 (1994).
19. J. Walsh and T. Deutsch, "Measurement of Er:YAG laser ablation plume dynamics," Appl. Phys. B **52**(3), 217–224 (1991).

20. W. Drexler and J. G. Fujimoto, *Optical Coherence Tomography: Technology and Applications* (Springer Science & Business Media, 2008).
21. J. G. Fujimoto and W. Drexler, "Introduction to OCT," in *Optical Coherence Tomography* (Springer, 2015), pp. 3–64.
22. J. A. Izatt and M. A. Choma, "Theory of optical coherence tomography," in *Optical Coherence Tomography* (Springer, 2008), pp. 47–72.
23. W. Bao, Z. Ding, J. Qiu, Y. Shen, P. Li, and Z. Chen, "Quasi-needle-like focus synthesized by optical coherence tomography," Opt. Lett. **42**(7), 1385–1388 (2017).
24. L. Yu, B. Rao, J. Zhang, J. Su, Q. Wang, S. Guo, and Z. Chen, "Improved lateral resolution in optical coherence tomography by digital focusing using two-dimensional numerical diffraction method," Opt. Express **15**(12), 7634–7641 (2007).
25. A. Dubois, O. Levecq, H. Azimani, D. Siret, A. Barut, M. Suppa, V. Del Marmol, J. Malvehy, E. Cinotti, and P. Rubegni, "Line-field confocal optical coherence tomography for high-resolution noninvasive imaging of skin tumors," J. Biomed. Opt. **23**(10), 1 (2018).
26. S. G. Adie, N. D. Shemonski, T. S. Ralston, P. S. Carney, and S. A. Boppart, "Interferometric synthetic aperture microscopy (ISAM)," oct, 965 (2015).
27. E. Bo, X. Ge, L. Wang, X. Wu, Y. Luo, S. Chen, S. Chen, H. Liang, G. Ni, and X. Yu, "Multiple aperture synthetic optical coherence tomography for biological tissue imaging," Opt. Express **26**(2), 772–780 (2018).
28. E. Bo, Y. Luo, S. Chen, X. Liu, N. Wang, X. Ge, X. Wang, S. Chen, S. Chen, and J. Li, "Depth-of-focus extension in optical coherence tomography via multiple aperture synthesis," Optica **4**(7), 701–706 (2017).
29. A. Curatolo, P. R. Munro, D. Lorenser, P. Sreekumar, C. C. Singe, B. F. Kennedy, and D. D. Sampson, "Quantifying the influence of Bessel beams on image quality in optical coherence tomography," Sci. Rep. **6**(1), 23483 (2016).
30. B. Hermann, E. Fernández, A. Unterhuber, H. Sattmann, A. Fercher, W. Drexler, P. Prieto, and P. Artal, "Adaptive-optics ultrahigh-resolution optical coherence tomography," Opt. Lett. **29**(18), 2142–2144 (2004).
31. L. Liu, F. Diaz, L. Wang, B. Loiseaux, J.-P. Huignard, C. Sheppard, and N. Chen, "Superresolution along extended depth of focus with binary-phase filters for the Gaussian beam," J. Opt. Soc. Am. A **25**(8), 2095–2101 (2008).
32. T. S. Ralston, S. G. Adie, D. L. Marks, S. A. Boppart, and P. S. Carney, "Cross-validation of interferometric synthetic aperture microscopy and optical coherence tomography," Opt. Lett. **35**(10), 1683–1685 (2010).
33. K. Sasaki, K. Kurokawa, S. Makita, and Y. Yasuno, "Extended depth of focus adaptive optics spectral domain optical coherence tomography," Biomed. Opt. Express **3**(10), 2353–2370 (2012).
34. D. S. Simon, "Bessel beams, self-healing, and diffraction-free propagation," in *A Guided Tour of Light Beams: From Lasers to Optical Knots* (IOP Concise Physics, 2016), pp. 1–15.
35. Y. Fan, B. Zhang, W. Chang, X. Zhang, and H. Liao, "A novel integration of spectral-domain optical-coherence-tomography and laser-ablation system for precision treatment," International journal of computer assisted radiology and surgery **13**(3), 411–423 (2018).
36. W.-Y. Oh, S. Yun, B. Vakoc, G. Tearney, and B. Bouma, "Ultrahigh-speed optical frequency domain imaging and application to laser ablation monitoring," Appl. Phys. Lett. **88**(10), 103902 (2006).
37. P. J. Webster, M. S. Muller, and J. M. Fraser, "High speed in situ depth profiling of ultrafast micromachining," Opt. Express **15**(23), 14967–14972 (2007).
38. K. Beaudette, H. W. Baac, W.-J. Madore, M. Villiger, N. Godbout, B. E. Bouma, and C. Boudoux, "Laser tissue coagulation and concurrent optical coherence tomography through a double-clad fiber coupler," Biomed. Opt. Express **6**(4), 1293–1303 (2015).
39. K. Beaudette, W. Lo, M. Villiger, M. Shishkov, N. Godbout, B. E. Bouma, and C. Boudoux, "Towards in vivo laser coagulation and concurrent optical coherence tomography through double-clad fiber devices," in *Multimodal Biomedical Imaging XI* (International Society for Optics and Photonics, 2016), 97010B.
40. S. Liang, C. Sun, A. Saidi, J. Jing, G. Liu, J. Li, J. Zhang, Z. Chen, and J. Narula, "Intravascular atherosclerotic imaging with combined fluorescence and optical coherence tomography probe based on a double-clad fiber combiner," J. Biomed. Opt. **17**, 070501 (2012).
41. H. Pahlevaninezhad, A. M. Lee, T. Shaipanich, R. Raizada, L. Cahill, G. Hohert, V. X. Yang, S. Lam, C. MacAulay, and P. Lane, "A high-efficiency fiber-based imaging system for co-registered autofluorescence and optical coherence tomography," Biomed. Opt. Express **5**(9), 2978–2987 (2014).
42. M. Bonesi, M. Minneman, J. Ensher, B. Zabihian, H. Sattmann, P. Boschert, E. Hoover, R. Leitgeb, M. Crawford, and W. Drexler, "Akinetic all-semiconductor programmable swept-source at 1550 nm and 1310 nm with centimeters coherence length," Opt. Express **22**(3), 2632–2655 (2014).
43. S. Song, J. Xu, and R. K. Wang, "Long-range and wide field of view optical coherence tomography for in vivo 3D imaging of large volume object based on akinetic programmable swept source," Biomed. Opt. Express **7**(11), 4734–4748 (2016).
44. N. Jowett, W. Wöllmer, R. Reimer, J. Zustin, U. Schumacher, P. W. Wiseman, A. M. Mlynarek, A. Böttcher, C. V. Dalchow, and B. B. Lörincz, "Bone ablation without thermal or acoustic mechanical injury via a novel picosecond infrared laser (PIRL)," Otolaryngol.–Head Neck Surg. **150**(3), 385–393 (2014).
45. L. M. B. Bernal, I. T. Schmidt, N. Vulin, J. Widmer, J. G. Snedeker, P. C. Cattin, A. Zam, and G. Rauter, "Optimizing controlled laser cutting of hard tissue (bone)," at-Automatisierungstechnik **66**(12), 1072–1082 (2018).
46. V. Tuchin, "Tissue optics and photonics: Light-tissue interaction II," J. Biomed. Photonics Eng. **2**(3), 030201 (2016).

47. R. Eriksson, T. Albrektsson, and B. Magnusson, "Assessment of bone viability after heat trauma: a histological, histochemical and vital microscopic study in the rabbit," Scand. J. Plast. Reconstr. Surg. **18**(3), 261–268 (1984).

48. S. R. Visuri, J. T. Walsh Jr, and H. A. Wigdor, "Erbium laser ablation of dental hard tissue: effect of water cooling," Lasers in Surgery and Medicine **18**, 294–300 (1996).

49. A. K. Dubey and V. Yadava, "Laser beam machining—a review," International Journal of Machine Tools and Manufacture **48**(6), 609–628 (2008).

50. N. Rachmanis, G. B. McGuinness, and J. A. McGeough, "Characterisation of debris from laser and mechanical cutting of bone," Proc. Inst. Mech. Eng., Part H **228**(7), 735–739 (2014).

51. K. Nahen and A. Vogel, "Plume dynamics and shielding by the ablation plume during Er:YAG laser ablation," J. Biomed. Opt. **7**(2), 165–179 (2002).

52. J. Arlt, V. Garcés-Chávez, W. Sibbett, and K. Dholakia, "Optical micromanipulation using a Bessel light beam," Opt. Commun. **197**(4-6), 239–245 (2001).

53. I. Apitz and A. Vogel, "Material ejection in nanosecond Er:YAG laser ablation of water, liver, and skin," Appl. Phys. A **81**(2), 329–338 (2005).

54. Z. Ding, H. Ren, Y. Zhao, J. S. Nelson, and Z. Chen, "High-resolution optical coherence tomography over a large depth range with an axicon lens," Opt. Lett. **27**(4), 243–245 (2002).

55. R. Leitgeb, M. Villiger, A. Bachmann, L. Steinmann, and T. Lasser, "Extended focus depth for Fourier domain optical coherence microscopy," Opt. Lett. **31**(16), 2450–2452 (2006).

56. Y. Ismail, N. Khilo, V. Belyi, and A. Forbes, "Shape invariant higher-order Bessel-like beams carrying orbital angular momentum," J. Opt. **14**(8), 085703 (2012).

57. V. Belyi, A. Forbes, N. Kazak, N. Khilo, and P. Ropot, "Bessel–like beams with z–dependent cone angles," Opt. Express **18**(3), 1966–1973 (2010).

58. L. M. B. Bernal, F. Canbaz, A. Droneau, N. F. Friederich, P. C. Cattin, and A. Zam, "Optimizing deep bone ablation by means of a microsecond Er:YAG laser and a novel water microjet irrigation system," Biomed. Opt. Express **11**(12), 7253–7272 (2020).

59. D. Lorenser, C. C. Singe, A. Curatolo, and D. D. Sampson, "Energy-efficient low-Fresnel-number Bessel beams and their application in optical coherence tomography," Opt. Lett. **39**(3), 548–551 (2014).

60. K.-S. Lee and J. P. Rolland, "Bessel beam spectral-domain high-resolution optical coherence tomography with micro-optic axicon providing extended focusing range," Opt. Lett. **33**(15), 1696–1698 (2008).

61. N. Gutknecht, M. Lukac, M. Marincek, T. Perhavec, and M. Kazic, "A novel quantum square pulse (QSP) mode erbium dental laser," J LAHA **1**, 15–21 (2011).

3.2   Multimodal feedback systems for smart laser osteotomy: Depth control and tissue differentiation

In the second publication, a close-loop tissue-specific laser osteotomy system is presented. In this study, a tissue sensor (LIBS) is integrated to differentiate tissue types and to avoid damaging soft tissue during laser osteotomy. The developed system is a coaxial integration of a long-range BLB-OCT system (visual feedback and depth control), a LIBS (tissue sensor), and an Er:YAG laser.

Publication: Hamidi, A., Bayhaqi, Y. A., Drusová, S., Navarini, A. A., Cattin, P. C., Canbaz, F., & Zam, A. Multimodal feedback systems for smart laser osteotomy: Depth control and tissue differentiation. Lasers in Surgery and Medicine, Wiley.

BASIC SCIENCE ARTICLE

Multimodal feedback systems for smart laser osteotomy: Depth control and tissue differentiation

Arsham Hamidi PhD[1] | Yakub A. Bayhaqi PhD[1] | Sandra Drusová PhD[1] |
Alexander A. Navarini MD, PhD[2] | Philippe C. Cattin PhD[3] |
Ferda Canbaz PhD[1] | Azhar Zam PhD[1,4,5]

[1]Biomedical Laser and Optics Group (BLOG), Department of Biomedical Engineering, University of Basel, Allschwil, Switzerland

[2]Digital Dermatology, Department of Biomedical Engineering, University of Basel, Allschwil, Switzerland

[3]Department of Biomedical Engineering, Center for medical Image Analysis and Navigation (CIAN), University of Basel, Allschwil, Switzerland

[4]Division of Engineering, New York University Abu Dhabi, Abu Dhabi, UAE

[5]Department of Biomedical Engineering, Department of Electrical and Computer Engineering, Tandon School of Engineering, New York University, Brooklyn, New York, USA

Correspondence

Arsham Hamidi, PhD and Azhar Zam, PhD, Biomedical Laser and Optics Group (BLOG), Department of Biomedical Engineering, University of Basel, CH-4123 Allschwil, Switzerland.
Email: arsham.hamidi@unibas.ch and azhar.zam@nyu.edu

Abstract

Objectives: The study aimed to improve the safety and accuracy of laser osteotomy (bone surgery) by integrating optical feedback systems with an Er:YAG laser. Optical feedback consists of a real-time visual feedback system that monitors and controls the depth of laser-induced cuts and a tissue sensor differentiating tissue types based on their chemical composition. The developed multimodal feedback systems demonstrated the potential to enhance the safety and accuracy of laser surgery.

Materials and Methods: The proposed method utilizes a laser-induced breakdown spectroscopy (LIBS) system and long-range Bessel-like beam optical coherence tomography (OCT) for tissue-specific laser surgery. The LIBS system detects tissue types by analyzing the plasma generated on the tissue by a nanosecond Nd:YAG laser, while OCT provides real-time monitoring and control of the laser-induced cut depth. The OCT system operates at a wavelength of 1288 ± 30 nm and has an A-scan rate of 104.17 kHz, enabling accurate depth control. Optical shutters are used to facilitate the integration of these multimodal feedback systems.

Results: The proposed system was tested on five specimens of pig femur bone to evaluate its functionality. Tissue differentiation and visual depth feedback were used to achieve high precision both on the surface and in-depth. The results showed successful real-time tissue differentiation and visualization without any visible thermal damage or carbonization. The accuracy of the tissue differentiation was evaluated, with a mean absolute error of 330.4 μm and a standard deviation of ± 248.9 μm, indicating that bone ablation was typically stopped before reaching the bone marrow. The depth control of the laser cut had a mean accuracy of 65.9 μm with a standard deviation of ± 45 μm, demonstrating the system's ability to achieve the pre-planned cutting depth.

Conclusion: The integrated approach of combining an ablative laser, visual feedback (OCT), and tissue sensor (LIBS) has significant potential for enhancing minimally invasive surgery and warrants further investigation and development.

KEYWORDS

Er:YAG laser, laser-induced breakdown spectroscopy, laser osteotomy, smart laser surgery, optical coherence tomography

---

INTRODUCTION

Laser osteotomy is a contactless surgical procedure where bone tissue is removed by a laser. The advantages of using lasers include faster healing, functional cutting geometries, and no contamination, due to contactless cutting.[1–4] Laser osteotomy has the potential to replace conventional osteotomy in the future, but first, several challenges still need to be addressed.[5,6] An important aspect of any surgical intervention is safety, which is typically carried out by surgeons during conventional surgery. In the case of laser osteotomy, in free-space and endoscopic settings, a feedback system is required to avoid damaging the critical adjacent tissue. Ideally, a noninvasive method is needed to provide real-time feedback about the depth of the cut and the tissue type.

To date, several feedback systems for controlling the depth of cuts in laser surgery have been reported in the literature. Optoacoustic tomography,[7,8] inline coherent imaging (ICI),[9] optical coherence tomography (OCT)[10–12] are some of the techniques introduced for monitoring the depth of laser-induced cuts. Particularly, OCT has demonstrated high-speed monitoring of the ablation process noninvasively presenting superior advantages compared to other methods. OCT is a well-established noninvasive imaging technique in medical diagnosis because it can provide three-dimensional (3D) images of the tissue with high resolution.[13,14] Tissue sensors play a vital role in advanced laser surgery, enabling precise and targeted procedures while minimizing the risk of unintended damage. These sensors operate by identifying the type of tissues through the detection of their optical or mechanical characteristics. By leveraging this principle, tissue sensors provide valuable information that guides surgeons in performing tissue-specific laser surgery. An example of this is the utilization of acoustic shock waves (ASWs), which are primarily influenced by the properties of the ablated material. As a result, ASWs can be employed to identify and differentiate various types of tissues. The optical methods have often been combined with machine-learning classification algorithms. Hohmann et al.[15] used random lasing phenomena caused by the scattering of fluorescent emissions in the tissue. The tissues were classified using support vector machines (SVM). Other machine learning approaches were diffuse reflectance spectroscopy with linear discriminant analysis,[16–18] Raman spectroscopy and nearest-mean classifiers,[19] and OCT and convolutional neural networks.[20,21] The utilization of short-pulse (ns-ps-fs) laser ablation systems offers the advantage of generating a localized plasma at the ablation site. Spectroscopic analysis of the generated plasma can reveal the chemical composition of the tissue, enabling precise tissue differentiation. Both Nd:YAG and CO_2 lasers have demonstrated successful outcomes in ablation and tissue differentiation during laser surgery.[22–27]

Furthermore, studies have reported the integration of OCT into the aforementioned configuration to achieve tissue differentiation and depth monitoring.[28,29] However, these investigations are limited to nonbiological samples, and challenges during laser surgery have not been investigated. Despite the simplified configuration of using a single laser for both tissue differentiation and laser ablation, it should be noted that a significant portion of the laser pulse's energy is primarily consumed for plasma generation, resulting in limited ablation efficiency. Consequently, to achieve deep laser-induced ablation, longer-pulsed lasers are preferred. Er:YAG laser (2.94 μm) in μs pulse regime has demonstrated a superior advantage to achieve deep laser ablation in hard tissues in comparison to the Nd:YAG and CO_2 lasers. The high absorption of Er:YAG laser at water molecules inside the bone tissue can lead to an efficient laser ablation with minimal thermal damage to the surrounding tissue.[30] Another efficient optical method for analyzing the chemical content of different tissues is laser-induced breakdown spectroscopy (LIBS).[27,31] LIBS is considered a slightly invasive technique due to the need for slight tissue removal during the plasma generation process. Following the collection of plasma, the tissue can be differentiated from other tissue types by comparing the ratios of selected peaks.[32]

Although several methods have been used for depth monitoring and tissue differentiation, only a few have been implemented as feedback systems for laser osteotomy. In our earlier study,[33] we presented a streamlined integration of the Er:YAG laser and Nd:YAG laser for tissue differentiation and ablation. The tissue differentiation relied on the collected intensity of the generated plasma without spectrum analysis. However, certain drawbacks, including the sensitivity of the detected intensity level to various parameters (e.g., tissue hydration, presence of water/blood, tissue roughness) and a limited depth of focus, were recognized as limitations of the previous configuration. In this paper, we present a novel and smart feedback system capable of simultaneous depth control and tissue-specific ablation. This system can further be used in other applications with only small iterations in the controlling algorithm, increasing its appeal for transferring optical systems into real-life clinical applications. Depth control was demonstrated by making several cuts to a predefined depth while preserving the soft tissue. The system uses a long-range Bessel-like beam OCT capable of imaging deep cuts up to 26.2 mm. Bone-specific ablation was achieved using LIBS combined with a novel software that first generates the tissue type map and keeps it in its memory. This memory reduces the data-processing time during ablation and the risk of repetitive tissue damage with plasma generation. The presented coaxial integration of various feedback systems yields superior accuracy in deep laser ablation compared to alternative configurations. This represents a significant technological advancement toward utilizing laser osteotomy in minimally invasive surgery.

MATERIALS AND METHODS

Laser osteotomy

The ablation mechanism of the Er:YAG laser is known as photothermal ablation, and it has been demonstrated to make efficient ablations of hard tissue with minimal collateral damage.[34,35] The wavelength of the Er:YAG laser (2.94 μm) has high absorption in water and hydroxyapatite (≈73% of bone's structure[36,37]). The photothermal interaction steps are the following: (1) laser pulse energy is transferred to the tissue, (2) the temperature of the tissue increases, (3) the pressure buildup inside the hard tissue leads to micro explosions resulting in tissue removal.[38] However, the high ablation efficiency of the Er:YAG laser in hard tissues results in a lower cutting precision in comparison to other lasers used in osteotomy.[39] A study regarding the ablation efficiency of the Er:YAG laser in bone ablation is provided elsewhere.[35] In this study, we used an Er:YAG laser (LITETOUCH by Syneron) for cutting bone tissue. The Er:YAG laser was running at a 2 Hz repetition rate and a pulse energy of 138.3 mJ. To perform line cuts, the samples were placed on a 1D motorized stage.

Real-time depth control

OCT is a noninvasive interferometric imaging technology that can provide 3D and real-time tissue images with submillimeter resolution.[40] The first study that monitored the laser ablation process using OCT demonstrated its potential capabilities for use as a reliable visual feedback system.[41] The high-speed imaging of OCT can make it possible to control the depth of laser-induced cuts. In this study, the depth of the cut was measured based on the difference between the height of the reference line (the surface of the surrounding areas) and the bottom surface of the cut. This was measured by integrating the OCT system with an ablative laser controlled by an optical shutter. This allowed the OCT system to send a trigger to close the optical shutter when the desired ablation depth had been reached.
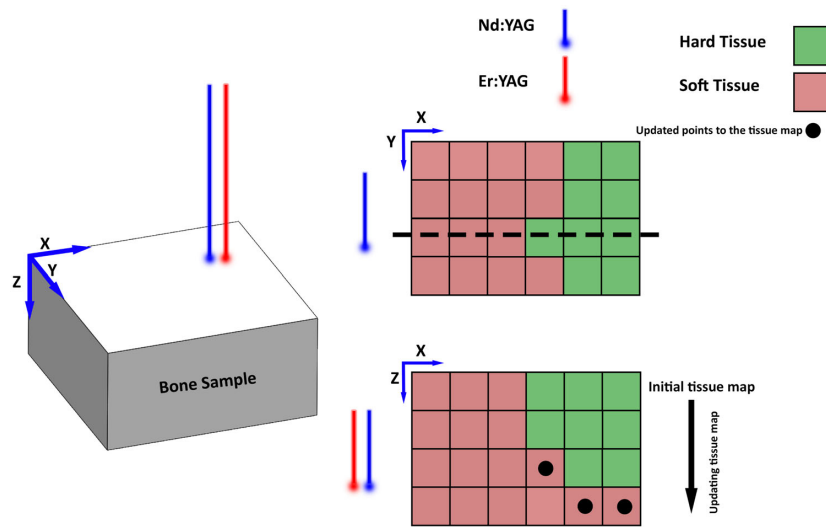
Tissue differentiation

Knowledge regarding the type of tissue before firing the ablative laser pulse is crucial for ensuring laser surgery's safety. Among the different methods for tissue differentiation in laser surgery, LIBS has exhibited promising results in performing tissue-specific surgery.[42] The LIBS analysis system consists of two elements: an excitation laser (here Nd:YAG, 1064 nm, at 4 Hz repetition rate and pulse energy of 85.9 mJ) that produces plasma on the surface of the tissue and a spectrometer that analyzes the collected spectrum. The collected spectrum matches the chemical structure of the material under investigation.[43] Here our main interest was to ablate hard tissue while preserving soft tissue. To do so, the difference in the intensity of calcium peaks (385–400 nm) of hard tissue's spectrum (bone) and that of soft tissue (bone marrow, muscle, etc.) was used. Therefore, the strong peaks in the spectrum of the bone in comparison to soft tissue make it distinguishable. Laser osteotomy requires 3D tissue differentiation that can detect the type of tissue on the surface and below the surface. Although the LIBS method can provide accurate information regarding tissue type, plasma generation on the tissue is accompanied by a shallow ablation of the tissue. To prevent further unwanted damage to the superficial soft tissue, we used a tissue map. The working principle was to compare the intensity of the Ca peaks in the spectra of the tissues, which are the main difference between the soft and the hard tissues, at each individual point and then to use this to create a tissue map. Tissue differentiation was repeated twice for each spatial point to reduce the risk of incorrect detections. In addition, we have set a threshold of the intensity of the Ca peak to prevent false detection of debris splashed on the tissue. Figure 1 illustrates the working principle of the described method. The red and blue lines represent the Er:YAG and Nd:YAG lasers, respectively. The xy-coordinate plane is the surface of the bone. At first, a tissue map of the surface is created by LIBS. In Figure 1, the locations of the red boxes were detected as soft tissue, and the green boxes were recognized as hard tissue. Following the creation of the tissue map on the surface, a line cut (dashed line) was performed into the depth of the tissue. On the xz-coordinate plane, red boxes correspond to the spatial points that were detected as soft tissue, and neither the Nd:YAG laser nor the Er:YAG laser was used. During the ablation of the bone tissue, the tissue map was updated by the detection of soft tissue below the ablated bone tissue (marked with a black circle).

Integrated closed-loop setup

The optical setup consisted of an integration of three different optical technologies: an Er:YAG laser, LIBS, and OCT. Figure 2A illustrates the schematic of the combined setup with a long-range Bessel-like beam OCT system with a swept-source laser (Insight Photonic Solution, Inc.) with a central bandwidth of 1288 ± 30 nm, a swept rate of 104.17 kHz, and an imaging range of 26.2 mm.[10] The OCT system was responsible for monitoring and controlling the depth of the cut in real-time. In the OCT system, C1 and C2 were collimators, A1 and A2 were the axicon lenses with an apex angle of two degrees (AX122-C; Thorlabs), L1 and L2 were achromatic doublet lenses ($f = 75$ mm, AC127-075-C; Thorlabs), and L3 was an achromatic lens pair ($f = 100$ mm, 47-302, Edmundoptics). DM1 was a long-pass

FIGURE 1 Three-dimensional tissue differentiation. The *xy*-coordinate plane represents the surface of the sample. Red boxes correspond to spatial points detected to be soft tissue, and green boxes correspond to bone tissue. The *xz*-coordinate plane represents a depth at the dashed line in the *xy* plane. Black circles correspond to spatial points characterized as soft tissue and update the previous tissue map. At first, a tissue map is created by the LIBS system on the surface of the sample. The system remembers not to perform ablation and LIBS on soft tissue. Ablation and LIBS are performed on the hard-tissue points. When LIBS detects soft tissue after ablating hard tissue, the tissue map is updated. Once all the spatial points are detected as soft tissue, the ablation laser is stopped automatically.

dichroic mirror (DMLP950, Thorlabs) that transmitted the OCT wavelength and reflected the generated plasma light from the sample's surface. The reflected plasma light was directed to a multimode fiber, that delivered the light to the Echelle spectrometer using a microscope objective lens (RMS4X; Olympus). A flash-lamp pumped Q-switched Nd:YAG laser (Q-smart 450; Quantel) running at 1064 nm was used to generate the plasma light on the surface of the tissue. In Figure 2A, OS1 was an optical shutter (SH1; Thorlabs), L4 was a plano-convex lens ($f = 150$ mm, 69-622 Edmundoptics), and the Nd:YAG laser was combined with the OCT laser using a harmonic beam splitter (HBS, HBSY11; Thorlabs), which had a transmission of 53% at 1280 nm. Finally, the Er:YAG laser was combined with the OCT system and Nd:YAG lasers using a custom-made dichroic mirror (DM3, 97% reflection at 2.94 µm, and transmission at ≥90%1300 ± 75 nm). Here, OS2 was an optical shutter, and L5 was calcium fluoride (CaF₂, $f = 100$ mm; Thorlabs). Since the ablation process and plasma generation were accompanied by the generation of debris and tissue particles, a sapphire window was placed after the lenses to protect the optics. Proper adjustments of L4 and L5 according to the working distance of the OCT system ensured that all lasers had a common focal plane. The estimated beam size for Nd:YAG and Er:YAG lasers are 62.5 and 682.4 µm, and the corresponding pulses duration are 6 ns and 350 µs respectively. Finally, the sample was placed on a 2D stage (Standa 8MT167S-25LS-MEn1), that

could move in steps of 0.5 mm. A detailed version of the sample arm of the OCT system, which was integrated with the Er:YAG laser and LIBS system, is presented in Figure 2B.
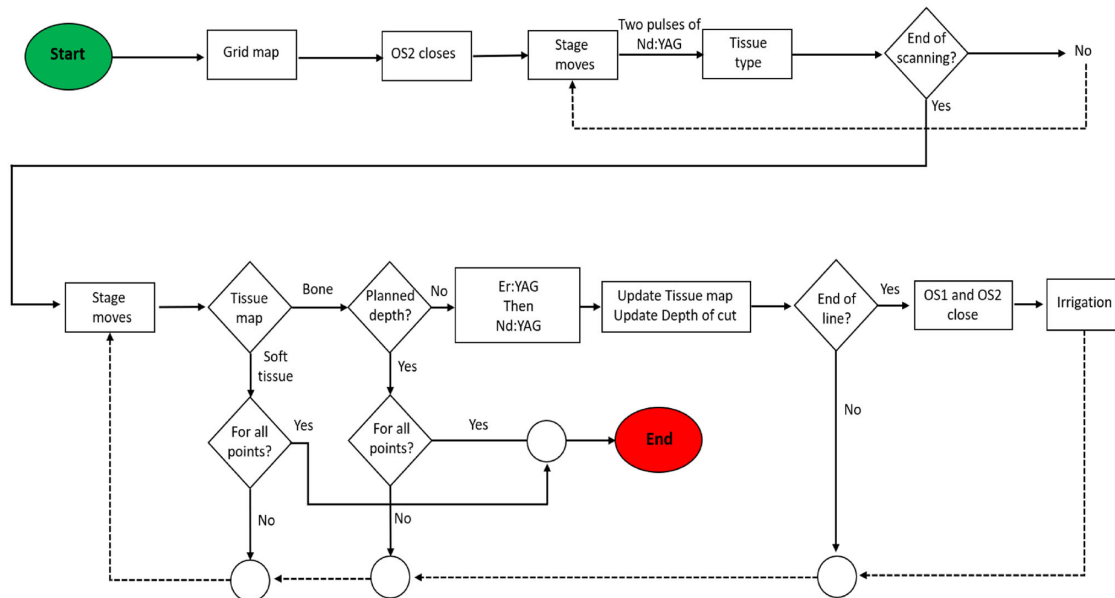
Workflow of the experiment

Integrating different laser technologies with different properties requires a predefined protocol to ensure the performance of an efficient and safe laser osteotomy. The workflow of the experiment is presented in Figure 3. To start, the sample was scanned on the *xy* plane to generate a 2D tissue map based on the analyzed data from the LIBS system.

For each point, two pulses of the Nd:YAG laser were fired at the sample to detect the tissue type, which was then saved to the tissue map. A high-pressure airflow was continuously used to reduce the error in the detection of the type of tissue by cleaning the surface of the sample. Following the generation of the map on the surface, the ablation procedure was initiated to cut a line by running the Er:YAG laser and the Nd:YAG laser in sequence (two pulses of the Er:YAG laser and then two pulses of Nd:YAG laser) on the bone parts. This sequence was longer than the required time for the formation of the debris cloud (500 µs[10]), which consequently results in false detection of the tissue type. Due to the photothermal
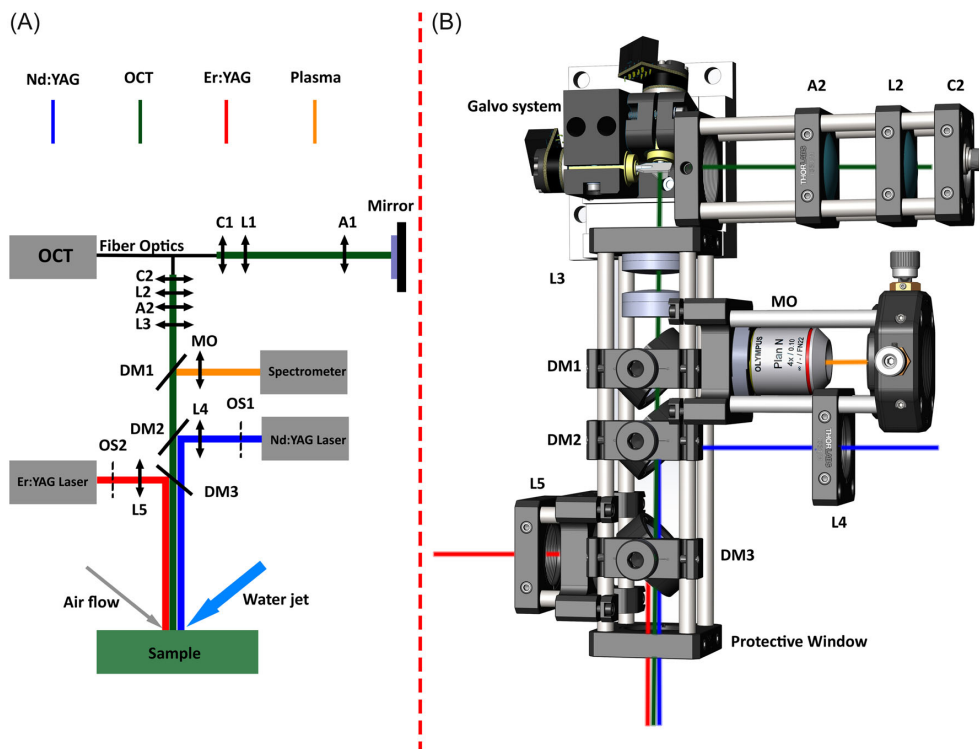
FIGURE 2 Schematic of the integrated setup including the optical coherence tomography (OCT) system, the Er:YAG laser, and the laser-induced breakdown spectroscopy system. (A) Simplified schematic of the optical setup. (B) A detailed version of the sample arm of the OCT system with the Er:YAG laser, Nd:YAG laser, and a channel for the collection of generated plasma.

FIGURE 3 Workflow of the experiment. Creation of a grid map at the first arrow beginning from START.

ablation mechanism of the Er:YAG laser, an irrigation system was essential. Irrigation can both improve ablation efficiency and reduce thermal damage to the surrounding area of the cut.[44] One major drawback of continuously using water is that excessive amounts of water on the surface of the bone can work as a protective shield reducing the ablation efficiency. In addition, a layer of water on the tissue can increase the chance of false detection by the LIBS system due to the high content of water in soft tissue. We, therefore, used a mechanism where the irrigation system (Synova Laser MicroJet Technology) only irrigated the sample at every end of the line cut for a couple of seconds. Consequently, after sufficiently irrigating the sample, high-pressure airflow removed the excess water on the surface. At each round of the laser ablation and tissue differentiation, the tissue map was updated by adding any detected soft tissue. As the laser continued ablation, it was possible for it to go through the bone and reach the bone marrow lying underneath in some regions. Updating the map was important for protecting soft tissues lying beneath hard tissue. These steps continued until the Nd:YAG laser detected bone marrow and commanded OS2 to stop at that spatial point. This way, we achieved 3D tissue differentiation (LIBS system) synchronized with depth monitoring (OCT system). To show that we can also control the ablation depth with the tissue map approach, we also set 1 mm as our cutting depth and ablation stopped when the pre-defined depth was reached.

The sequence and decisions of the closed-loop feedback system are controlled using integrated software (Figure 4). The software is responsible for (1) processing and visualization of the OCT data, controlling (2) the Nd:YAG laser and processing the LIBS data, (3) the irrigation system, (4) the shutters, (5) stages, and (6) Er:YAG laser. The detected spectrum of the plasma light using a camera (PI-MAX 4; Princeton Instruments) is transferred to the processing unit of the OCT system to detect the tissue type (green indicator in Figure 4 shows the bone tissue). To improve the speed of the tissue differentiation, we have used a cropped image (1024 × 70) which includes our main area of interest (the spectrum of the bone tissue). The overall response time for the acquisition of the spectrum and detection of the type of tissue was 2.3 Hz. Depth control was based on the cross-sectional image of the OCT (frame rate of 16.6 Hz). Following the detection of soft tissue or reaching the pre-planned depth of cut, a software command is sent to the optical shutters to stop the lasing process (response time = 10 ms, information was provided by the manufacturing company).

Specimens

In this experiment, we used five different pig femur slices purchased from a local butcher (Figure 5), and the experiment was performed on the same day. Samples have an average diameter of 25 mm and a height of 30 mm. Part of the muscle attached to the bone's surface was removed by a scalpel and cleaned using tap water. In this way, the surface of each sample had muscle and bone, as well as the bone marrow in the center. Samples were not fixed or processed with any chemicals.

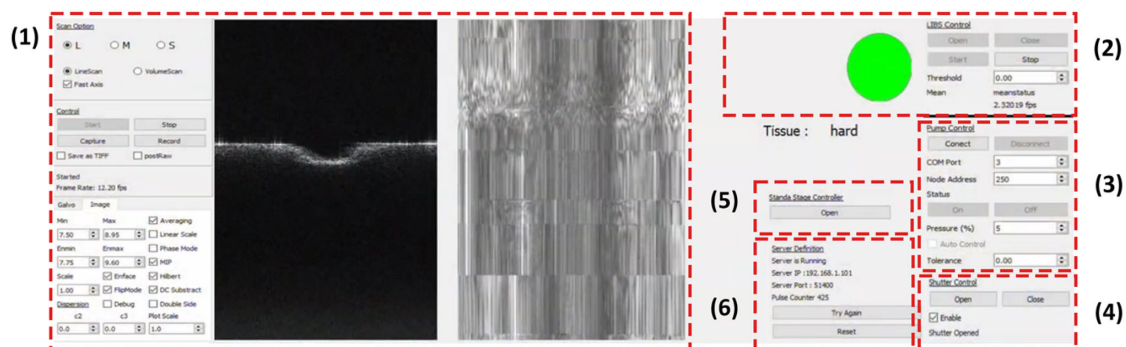**FIGURE 5** Prepared pig femur bone slices for the experiment.

FIGURE 4 Integrated software used in this study. The software controls (1) optical coherence tomography system, (2) laser-induced breakdown spectroscopy system, (3) irrigation system, (4) shutters, 5) stages, and (6) Er:YAG laser.

RESULTS

Tissue differentiation: Validation

To validate tissue differentiation based on the disparity in calcium peak intensities within the 385–400 nm range, we investigated the calcium peak intensities for five samples, including bone, muscle, and bone marrow. Figure 6A illustrates the spectroscopic analysis of the spectra from these three distinct tissue types studied in this research. The region of interest is highlighted in the graphs. To ascertain the disparity and establish the necessary threshold for distinguishing between bone and soft tissues (muscle and bone marrow), LIBS measurements were conducted on five different samples, with each type of tissue comprising 20 points, and the mean values of the peaks along with their standard deviations were evaluated. Figure 6B depicts the mean value and standard deviation of the calcium peaks for each sample. The variation in intensity values between bone and soft tissues served for tissue differentiation.

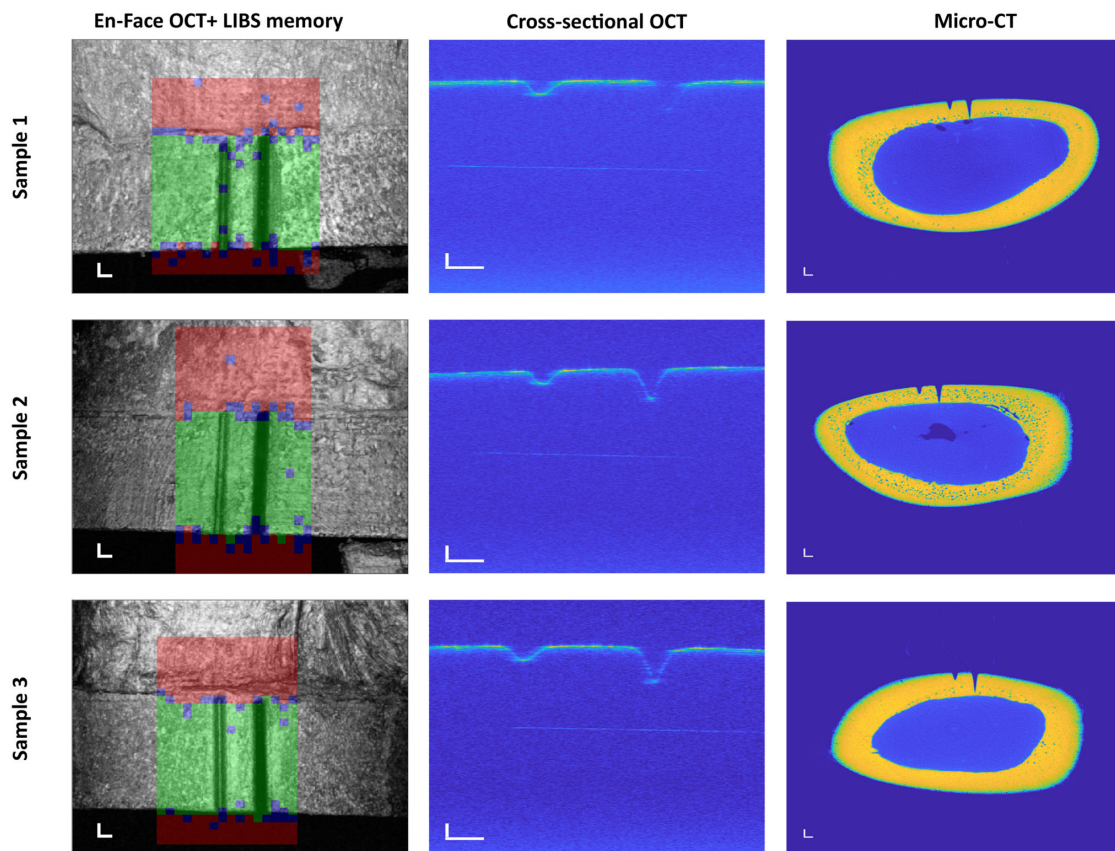## Real-time tissue differentiation and depth control

To test the functionality of the proposed system, we used closed-loop tissue differentiation and visual depth feedback on five different samples of pig femur bones. The tissue differentiation was used to achieve hard-bone-specific ablations on the surface (avoiding cutting muscle) and hard-bone-specific ablation in depth (cutting through the hard bone layer until bone marrow). The depth control feedback was used to achieve 1 mm deep cuts.

Figure 7 illustrates the representative results of the closed-loop real-time tissue differentiation and visualization during smart laser osteotomy. Each row in Figure 7, presents the results for each sample. No visual thermal damage or carbonization was induced during the experiment. From left to right, the first column is an en-face OCT image overlaid with the acquired tissue's map on the surface; the second column is a cross-sectional OCT image; and the third column is a cross-sectional image acquired with microcomputed tomography (micro-CT, pixel size of 18 μm). To generate the tissue map, two laser pulses were sent at each spatial point on the sample's surface. If both pulses detected the point as soft tissue, it was saved as soft tissue in the tissue map (red); if both pulses detected the point as hard tissue, it was saved as hard tissue (green); and if one pulse detected the point as soft and the other signal detected it as hard tissue, the point was saved as uncertain (blue). If an uncertain point was surrounded by soft or hard tissue, it was assigned the value of the neighboring tissue (after
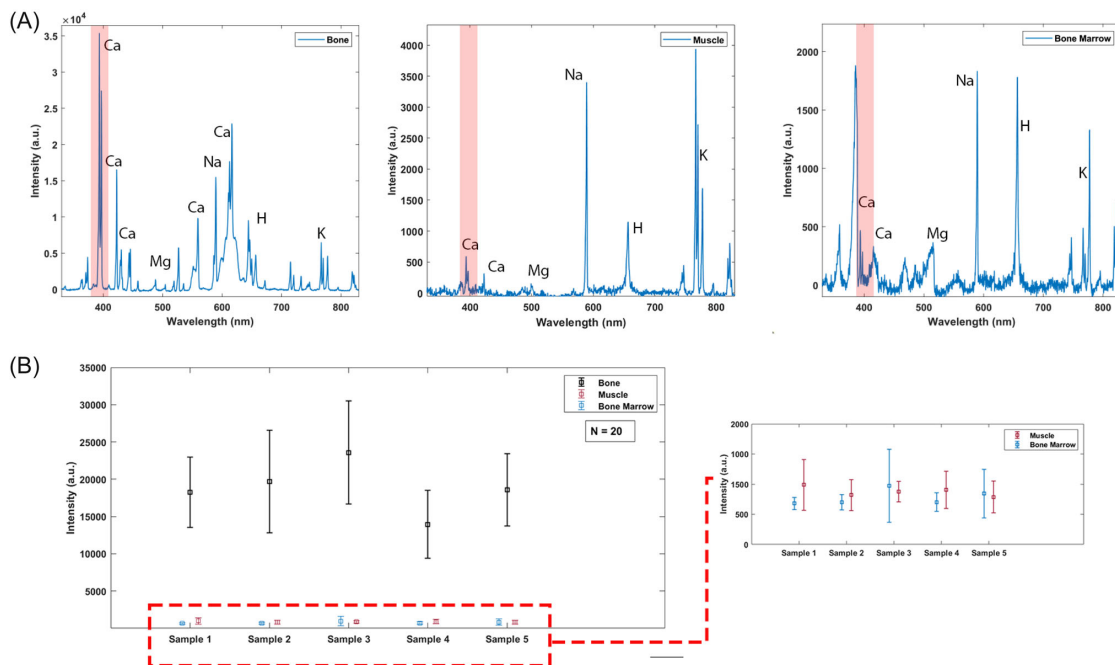
FIGURE 6 Tissue differentiation. (A) Laser-induced breakdown spectroscopy system spectrum of the bone, muscle, and bone marrow. (B) The mean and standard deviation of the intensity of the calcium peaks (385–400 nm) for 20 points for each tissue type. The experiment is performed on five samples.

| **En-Face OCT+ LIBS memory** | **Cross-sectional OCT** | **Micro-CT** |

FIGURE 7 Closed-loop tissue differentiation and depth monitoring in smart laser osteotomy. Representative three samples are separately presented in each row with corresponding optical coherence tomography (OCT) and computed tomography (CT) data. En-face OCT images overlaid with tissue map are presented in the first column; cross-sectional OCT images in the second; and micro-CT in the third. The cut on the left side is the controlled laser-induced cut, and the cut on the right side is the controlled tissue differentiation. The scale bars are 1 mm × 1 mm.

processing). The depth of the cut on the left side was controlled using the OCT system to achieve a cutting depth of 1 mm, and the cut on the right side was controlled using the tissue-differentiation method using LIBS (Figure 7). The controlled tissue differentiation stopped the Er:YAG laser as soon as the LIBS system detected soft tissue and the depth control stopped the ablative laser as soon as it reached the desired pre-planned depth of the cut by sending a command to OS2 to close.

Errors

The errors are illustrated in Figure 8, where Figure 8A illustrates the induced laser cut for tissue differentiation. The errors are calculated based on a total of 280 points from the micro-CT images. Here there is an error of cutting bone marrow of 0.468 mm. Figure 8B

corresponds to the error in the detection of tissue type. The Er:YAG laser stopped before reaching the bone marrow (0.19 mm of bone tissue is left).

Table 1 presents the accuracy of this experiment regarding depth control and tissue differentiation performed on five different samples of pig femur bones. Here, the border of the bone tissue and bone marrow is considered the reference point. Negative values denote the quantity of bone tissue left before reaching the bone marrow, whereas positive values indicate cases of false detection of tissue type and excessive ablation. It Is worth noting that due to variations in bone thickness along the ablation line, the error at each point is assessed in relation to the thickness of the bone at that specific point. For tissue differentiation, the mean value of the absolute error was 330.3 µm with a standard deviation of ±248.9 µm. The minimum and maximum values of this error show that bone ablation was usually stopped before it reached the bone marrow. The second row in Table 1
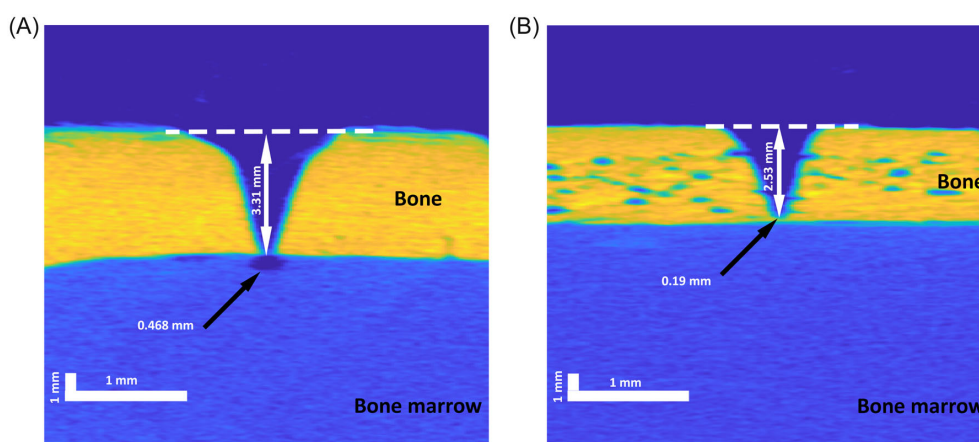
FIGURE 8 Cross-sectional images acquired with the micro-computed tomography to investigate the errors accompanied by closed-loop tissue differentiation and depth control. (A) Tissue (bone marrow) removal of 0.468 mm induced by the Nd:YAG laser for tissue differentiation; and (B) The Er:YAG laser stopped due to incorrect detection of the type of tissue. The scale bar is 1 mm 1 mm.

TABLE 1 Errors of the depth control and tissue differentiation for five samples of pig femur bones.

	Mean (µm)	Std (µm)	Maximum (µm)	Minimum (µm)
Tissue differentiation	330.3	±248.9	720	−1846
Depth control	65.9	±45	188	−279.9

shows that the mean value accuracy was 65.9 µm with a standard deviation of ±45 µm for the depth-controlled laser cut.

DISCUSSION AND CONCLUSION

In this study, we investigated the potential of a closed-loop laser ablation empowered with both OCT (visualization and depth control) and a LIBS system (tissue differentiation). Although laser osteotomy offers several advantages compared to conventional methods for bone surgery, feedback systems are crucial to ensuring the safety of the surgery. The left column of Figure 7 indicates that the proposed method has the potential to differentiate soft tissue (muscle) and hard tissue (bone) by comparing the peaks of Ca intensity in the collected spectrum. To evaluate the method, we acquired larger-scale tissue maps in comparison to the line cut. As one can see, the blue regions (uncertain tissue points) are largely located on the border between muscle and bone or between bone and air. These uncertain points are mainly due to the presence of debris created during plasma generation on the surrounding spatial points or to the difference in spot size of the lasers and movement steps of the stage. Furthermore, the uncertain points surrounded by the same type of tissue are unexpected

errors that will be converted to the value of the surrounding points after acquiring the tissue map. The column in the middle of Figure 7 represents the real-time visual feedback and depth control provided by the OCT images. In the sample arm of the OCT system, several optical components in the optical path of the OCT laser (DM1, HBS, DM3, and protective window) can cause some noise in the OCT images. We were able to adjust the angle of DM1, DM3, and the protective window to avoid reflections; a high reflection of the OCT wavelength in the HBS made the visible line in the OCT cross-sectional images. The third column in Figure 7 corresponds to the micro-CT images acquired just after finishing the experiment to avoid detaching soft tissue from the bone at room temperature.

Figure 8 presents the type of tissue in the depth of the bone with the detection error. Figure 8A illustrates the case of an incorrect detection of the tissue type that caused ablation of bone marrow. Here we used changes in the intensity of Ca peaks for tissue differentiation. As a consequence, changes in the amount of collected plasma can cause an error in detection. For example, the conical geometry of the laser-induced cut led to a lower collection of plasma light at the bottom of the cut than on the surface of the bone. Ablation of bone marrow by the Er:YAG laser or generation of plasma on soft tissue accompanied by splashing of soft tissue on

surrounding tissue could stop the ablation laser if soft tissue was detected (Figure 8B). While this experiment used continuous high-pressure air to avoid such errors, the air could not reach the bottom of the cut due to the shape of the laser-induced incision. Table 1 presents the method's accuracy with regard to tissue differentiation and depth control in its application to the five different samples. An error of $330.3 \pm 248.9\,\mu m$ indicates that the ablation was often stopped before reaching bone marrow. In addition, it is worth noting that this method could not avoid slight ablation of soft tissue by the Nd:YAG laser to generate plasma. The Er:YAG laser's maximum unwanted ablation of soft tissue below the surface was $1846\,\mu m$. This amount already shows how destructive Er:YAG laser can be in the case of a wrong detection or lacking feedback. The effect of such an error in tissue type detection can be reduced by controlling the ablation rate as the incision goes deeper. Another approach could be combining Er:YAG laser with a highly accurate light source producing ultrashort pulses. In this case, bulk ablation can be provided by the Er:YAG laser, while a secondary ablative laser is used to remove the tissue close to tissue borders and to define better borders. Alternatively, the feedback system can be combined with an ultrashort laser source to induce shallow cuts with high accuracy, then the speed of the feedback system should be optimized.

Advancing pre-planned and tissue-specific laser surgery was another aim of this study. Although OCT provided accurate monitoring of the cutting depth in real-time, controlling the depth of the cut also depended on changes in the properties of the bone tissue during the experiment. For example, dehydration or carbonization are parameters of the tissue that can change the ablation rate, which contributes to errors. The depth-controlled cuts for an incision with a depth of 1 mm had an error of $65.9 \pm 45\,\mu m$ (Table 1).

In 2016, an in-vivo mid-face osteotomy using a Carlo device was performed.[45,46] With the advancement of robotic laser surgery, research into feedback systems for ensuring safe automated surgery has become increasingly crucial. Even though certain safety aspects are included in the surgical device, achieving precision for depth control is significant. Highly precise laser surgery with depth control can provide pre-planned ablation accurately, providing small features and dimensions for patient-specific implants. Moreover, preventing damage to critical surrounding tissues (e.g., nerve tissue) can significantly enhance the safety of the laser osteotomy. The proposed closed-loop laser ablation approach can potentially improve the safety of minimally invasive surgery. This system can perform laser ablation with visual feedback and a tissue sensor to prevent unwanted damage to the tissue. Although the potential of OCT and LIBS systems have been well investigated in laser surgery systems, an integration of these

methods has not been undertaken. The tissue viability and feasibility studies can be performed in the future to test the method and laser ablation capabilities. To the best of our knowledge, this is the first integration of an ablative laser, visual feedback, and a tissue sensor in a coaxial manner, which has the potential to maintain the feedback's accuracy in a deep laser cut.

One of the limitations faced in the present study concerns the conical shape of the laser-induced cut, which limits the cross-section at the bottom of the cut and increases tissue differentiation errors. Using a tophat intensity beam could improve the accuracy of tissue differentiation.[47] Improving the airflow and irrigation system could further reduce errors in tissue differentiation. Furthermore, developing a real-time adjustment of the Er:YAG laser parameters is planned to achieve a higher accuracy in depth-controlled laser ablation. The integration of OCT has unlocked the potential for real-time depth monitoring and control in this study. We are also exploring additional capabilities of OCT, including temperature measurements,[48] tissue differentiation,[21] and the detection of parameters like water/blood content in tissue, which could potentially lead to incorrect tissue differentiation. For instance, OCT feedback regarding the accumulation of water/blood during surgery would trigger a pause in the operation of the LIBS and Er:YAG lasers to clean the surface using pressurized air and suction. Such feedback mechanisms have the potential to enhance the ablation efficiency of the Er:YAG laser and decrease the likelihood of false tissue type detection using the LIBS system.[49] in addition, A tracking system based on the OCT images targeting the center of the ablation crater can also reduce the error due to the movement of the patient. Integration of the aforementioned feedback systems is considered crucial before the transition of the developed system for an in-vivo experiment. Finally, improving the developed system and miniaturizing[50] it for use in minimally invasive surgery are among our future objectives.

CONFLICT OF INTEREST STATEMENT
The authors declare no conflict of interest.

ORCID
Arsham Hamidi http://orcid.org/0000-0002-3138-8939
Yakub A. Bayhaqi https://orcid.org/0000-0003-4193-5067
Sandra Drusová https://orcid.org/0000-0001-7728-8629
Alexander A. Navarini https://orcid.org/0000-0001-7059-632X
Philippe C. Cattin https://orcid.org/0000-0001-8785-2713

Ferda Canbaz https://orcid.org/0000-0003-4192-7163
Azhar Zam https://orcid.org/0000-0001-7789-5680

REFERENCES

1. Martins GL, Puricelli E, Baraldi CE, Ponzoni D. Bone healing after bur and Er:YAG laser ostectomies. J Oral and Maxillofac Surg. 2011;69(4):1214–20. https://doi.org/10.1016/j.joms.2010.02.029

2. Ohsugi Y, Aoki A, Mizutani K, Katagiri S, Komaki M, Noda M, et al. Evaluation of bone healing following Er:YAG laser ablation in rat calvaria compared with bur drilling. J Biophotonics. 2019;12(3):1–11. https://doi.org/10.1002/jbio.201800245

3. Baek Kw, Deibel W, Marinov D, Griessen M, Dard M, Bruno A, et al. A comparative investigation of bone surface after cutting with mechanical tools and Er: YAG laser. Lasers Surg Med. 2015;47(5):426–32.

4. Baek Kw, Dard M, Zeilhofer HF, Cattin PC, Juergens P. Comparing the bone healing after cold ablation robot-guided Er: YAG laser osteotomy and piezoelectric osteotomy–a pilot study in a minipig mandible. Lasers Surg Med. 2021;53(3): 291–9.

5. Stü binger S, Biermeier K, Bächi B, Ferguson SJ, Sader R, Von Rechenberg B. Comparison of Er:YAG laser, piezoelectric, and drill osteotomy for dental implant site preparation: A biomechanical and histological analysis in sheep. Lasers Surg Med. 2010;42(7):652–61. https://doi.org/10.1002/lsm.20944

6. Rajitha Gunaratne GD, Khan R, Fick D, Robertson B, Dahotre N, Ironside C. A review of the physiological and histological effects of laser osteotomy. J Med Eng Technol. 2017;41(1):1–12. https://doi.org/10.1080/03091902.2016.1199743

7. Landa FJO, Deán-Ben XL, de Espinosa FM, Razansky D. Noncontact monitoring of incision depth in laser surgery with air-coupled ultrasound transducers. Opt Lett. 2016;41(12):2704–7.

8. Bay E, Deán-Ben XL, Pang GA, Douplik A, Razansky D. Real-time monitoring of incision profile during laser surgery using shock wave detection. J Biophotonics. 2015;8(1–2):102–11.

9. Webster PJ, Wright LG, Mortimer KD, Leung BY, Yu JX, Fraser JM. Automatic real-time guidance of laser machining with inline coherent imaging. J Laser Appl. 2011;23(2):022001.

10. Hamidi A, Bayhaqi YA, Canbaz F, Navarini AA, Cattin PC, Zam A. Long-range optical coherence tomography with extended depth-of-focus: a visual feedback system for smart laser osteotomy. Biomed Opt Express. 2021;12(4):2118–33.

11. Fan Y, Zhang B, Chang W, Zhang X, Liao H. A novel integration of spectral-domain optical-coherence-tomography and laser-ablation system for precision treatment. Int J Comput Assist Radiol Surg. 2018;13:411–23.

12. Webster PJ, Muller MS, Fraser JM. High speed in situ depth profiling of ultrafast micromachining. Opt Express. 2007;15(23): 14967–72.

13. Singh SR, Chhablani J. Optical coherence tomography imaging: advances in ophthalmology. J Clin Med. 2022;11(10):2858. https://doi.org/10.3390/jcm11102858

14. Drexler W, Fujimoto JG, editors. Optical coherence tomography: technology and applications. vol. 2. Cham: Springer; 2015. https://doi.org/10.1007/978-3-319-06419-2

15. Hohmann M, Dörner D, Mehari F, Chen C, Späth M, Mü ller S, et al. Investigation of random lasing as a feedback mechanism for tissue differentiation during laser surgery. Biomed Opt Express. 2019;10(2):807. https://doi.org/10.1364/boe.10.000807

16. Gunaratne R, Goncalves J, Monteath I, Sheh R, Kapfer M, Chipper R, et al. Wavelength weightings in machine learning for ovine joint tissue differentiation using diffuse reflectance spectroscopy (DRS). Biomed Opt Express. 2020;11(9):5122. https://doi.org/10.1364/boe.397593

17. Stelzle F, Tangermann-Gerk K, Adler W, Zam A, Schmidt M, Douplik A, et al. Diffuse reflectance spectroscopy for optical soft tissue differentiation as remote feedback control for tissue-specific laser surgery. Lasers Surg Med. 2010;42(4):319–25.

18. Dahlstrand U, Sheikh R, Ansson CD, Memarzadeh K, Reistad N, Malmsjö M. Extended-wavelength diffuse reflectance spectroscopy with a machine-learning method for in vivo tissue classification. PLoS ONE. 2019;14(10):1–11. https://doi.org/10.1371/journal.pone.0223682

19. Ashok PC, Giardini ME, Dholakia K, Sibbett W. A Raman spectroscopy bio-sensor for tissue discrimination in surgical robotics. J Biophotonics. 2014;7(1–2):103–9. https://doi.org/10.1002/jbio.201300034

20. Bayhaqi YA, Hamidi A, Canbaz F, Navarini AA, Cattin PC, Zam A. Deep learning models comparison for tissue classification using optical coherence tomography images: toward smart laser osteotomy. OSA Continuum. 2021;4(9):2510. https://doi.org/10.1364/osac.435184

21. Bayhaqi YA, Hamidi A, Navarini AA, Cattin PC, Canbaz F, Zam A. Real-time closed-loop tissue-specific laser osteotomy using deep-learning-assisted optical coherence tomography. Biomed Opt Express. 2023;14(6):2986–3002.

22. Henn K, Gubaidullin GG, Bongartz J, Wahrburg J, Roth H, Kunkel M. A spectroscopic approach to monitor the cut processing in pulsed laser osteotomy. Lasers Med Sci. 2013;28:87–92.

23. Mehari F, Rohde M, Kanawade R, Knipfer C, Adler W, Klämpfl F, et al. Investigation of the differentiation of ex vivo nerve and fat tissues using laser-induced breakdown spectroscopy (LIBS): prospects for tissue-specific laser surgery. J Biophotonics. 2016;9(10):1021–32.

24. Kasem M, Gonzalez J, Russo R, Harith M. LIBS analysis of artificial calcified tissues matrices. Talanta. 2013;108:53–8.

25. Kanawade R, Mehari F, Knipfer C, Rohde M, Tangermann-Gerk K, Schmidt M, et al. Pilot study of laser induced breakdown spectroscopy for tissue differentiation by monitoring the plume created during laser surgery–an approach on a feedback Laser control mechanism. Spectrochim Acta B Atom Spectrosc. 2013;87:175–81.

26. Song Y, Hu G, Zhang Z, Guan Y. Real-time spectral response guided smart femtosecond laser bone drilling. Opt Lasers Eng. 2020;128:106017.

27. Rohde M, Mehari F, Klämpfl F, Adler W, Neukam FW, Schmidt M, et al. The differentiation of oral soft-and hard tissues using laser induced breakdown spectroscopy-a prospect for tissue specific laser surgery. J Biophotonics. 2017;10(10):1250–61.

28. Weimerskirch MJ, Kraft F, Pacher U, Hannesschläger G, Nagy TO. Absolute depth laser-induced breakdown spectroscopy-stratigraphy with non-scanning single spot optical coherence tomography. Spectrochim Acta B Atom Spectrosc. 2020;172: 105916.

29. Kaszewska EA, Sylwestrzak M, Marczak J, Skrzeczanowski W, Iwanicka M, Szmit-Naud E, et al. Depth-resolved multilayer pigment identification in paintings: combined use of laser-induced breakdown spectroscopy (LIBS) and optical coherence tomography (OCT). Appl Spectrosc. 2013;67(8):960–72.

30. Beltran Bernal LM. *Laser and wave-guides system for endoscopic/fiberscopic laser surgery*. PhD thesis. University of Basel; 2021.

31. Mehari F, Lengenfelder B, Figura R, Klämpfl F, Schmidt M. LIBS based tissue differentiation for Er:YAG surgical laser. In: Raposo M, Ribeiro PA, editors. Proceedings of the 6th International Conference on Photonics, Optics and Laser Technology in "Photoptics 2018". Setúbal: SCITEPRESS; 2018. https://doi.org/10.5220/0006637402470251

32. Kanawade R, Mahari F, Klämpfl F, Rohde M, Knipfer C, Tangermann-Gerk K, et al. Qualitative tissue differentiation by analysing the intensity ratios of atomic emission lines using laser induced breakdown spectroscopy (LIBS): prospects for a feedback mechanism for surgical laser systems. J Biophotonics. 2015;8(1–2): 153–61. https://doi.org/10.1002/jbio.201300159

33. Abbasi H, Bernal LMB, Hamidi A, Droneau A, Canbaz F, Guzman R, et al. Combined Nd: YAG and Er: YAG lasers for

real-time closed-loop tissue-specific laser osteotomy. Biomed Opt Express. 2020;11(4):1790–807.

34. Stü binger S. Advances in bone surgery: the Er: YAG laser in oral surgery and implant dentistry. Clin Cosmet Investig Dent. 2010;2: 47.

35. Bernal LMB, Canbaz F, Droneau A, Friederich NF, Cattin PC, Zam A. Optimizing deep bone ablation by means of a microsecond Er: YAG laser and a novel water microjet irrigation system. Biomed Opt Express. 2020;11(12):7253–72.

36. Forrer M, Frenz M, Romano V, Altermatt H, Weber H, Silenok A, et al. Bone-ablation mechanism using CO_2 lasers of different pulse duration and wavelength. Appl Phys B. 1993;56(2):104–12.

37. Fujii T, Baehni PC, Kawai O, Kawakami T, Matsuda K, Kowashi Y. Scanning electron microscopic study of the effects of Er: YAG laser on root cementum. J Periodontol. 1998;69(11):1283–90.

38. Tuchin VV. Tissue optics and photonics: light-tissue interaction. J Biomed Photon Eng. 2015;1(2):98–134.

39. Peavy GM, Reinisch L, Payne JT, Venugopalan V. Comparison of cortical bone ablations by using infrared laser wavelengths 2.9 to 9.2 μm. Lasers Surg Med. 1999;25(5):421–34.

40. Fujimoto JG, Pitris C, Boppart SA, Brezinski ME. Optical coherence tomography: an emerging technology for biomedical imaging and optical biopsy. Neoplasia. 2000;2(1–2):9–25.

41. Boppart SA, Herrmann J, Pitris C, Stamper DL, Brezinski ME, Fujimoto JG. High-resolution optical coherence tomography-guided laser ablation of surgical tissue. J Surg Res. 1999;82(2): 275–84.

42. Huang H, Yang LM, Bai S, Liu J. Smart surgical tool. J Biomed Opt. 2015;20(2):028001.

43. Tognoni E, Palleschi V, Corsi M, Cristoforetti G. Quantitative micro-analysis by laser-induced breakdown spectroscopy: a review of the experimental approaches. Spectrochim Acta B Atom Spectrosc. 2002;57(7):1115–30.

44. Beltran Bernal LM, Kosa G, Zelechowski M, Rauter G, Friederich N, Cattin P, et al. Performance of Er:YAG laser ablation of hard bone under different irrigation water cooling conditions. Optical interactions with tissue and cells XXIX. SPIE, Washington; 2018. https://doi.org/10.1117/12.2290929

45. Baek KW, Deibel W, Marinov D, Griessen M, Bruno A, Zeilhofer HF, et al. Clinical applicability of robot-guided contact-free laser osteotomy in cranio-maxillo-facial surgery: in-vitro simulation and in-vivo surgery in minipig mandibles. Br J Oral Maxillofac Surg. 2015;53(10):976–81.

46. Deibel W, Schneider A, Augello M, Bruno AE, Juergens P, Cattin P. A compact, efficient, and lightweight laser head for CARLO®: integration, performance, and benefits. Novel optical systems design and optimization XVIII. Washington: SPIE; 2015. https://doi.org/10.1117/12.2187992

47. Rung S, Barth J, Hellmann R. Characterization of laser beam shaping optics based on their ablation geometry of thin films. Micromachines. 2014;5(4):943–53.

48. Hamidi A, Bayhaqi YA, Canbaz F, Navarini A, Cattin PC, Zam A. Imaging photothermal-induced expansion of bone during laser osteotomy by phase-sensitive OCT: preliminary results. Biomedical spectroscopy, microscopy, and imaging. SPIE, Washington. https://doi.org/10.1117/12.2555675

49. Moon Y, Han JH, Lee JJ, Jeong S. Influence of water content on the laser-induced breakdown spectroscopy analysis of human cell pellet. Spectrochim Acta B Atom Spectrosc. 2015;114:27–33.

50. Hamidi A, Bayhaqi YA, Navarini AA, Cattin PC, Zam A, Canbaz F. Towards miniaturized OCT-guided laser osteotomy: integration of fiber-coupled Er:YAG laser with OCT. Opt Continuum. 2023;2(10):2106–15. https://doi.org/10.1364/OPTCON.497483

Phase-sensitive OCT system: Temperature Feedback

The publications in this chapter document the investigations on a phase-sensitive OCT system for use in temperature feedback during laser osteotomy. Temperature feedback could minimize the risk of thermal damage to the surrounding critical tissue.

4.1 Imaging photo-thermal expansion of bone tissue

The first publication concerns the development of a phase-sensitive OCT system. The developed phase-sensitive OCT system demonstrated the potential to detect the thermal expansion in bone tissue induced by the Er:YAG laser.

Publication: Hamidi, A., Bayhaqi, Y. A., Canbaz, F., Navarini, A., Cattin, P. C., and Zam, A. (2020, April). Imaging photothermal-induced expansion of bone during laser osteotomy by phase-sensitive OCT: preliminary results. In Biomedical Spectroscopy, Microscopy, and Imaging (Vol. 11359, pp. 127-133), SPIE.

PROCEEDINGS OF SPIE

Imaging photothermal-induced expansion of bone during laser osteotomy by phase-sensitive OCT: preliminary results

Hamidi, Arsham, Bayhaqi, Yakub, Canbaz, Ferda, Navarini, Alexander, Cattin, Philippe, et al.

SPIE.

Event: SPIE Photonics Europe, 2020, Online Only, France

Imaging photothermal-induced expansion of bone during laser osteotomy by phase-sensitive OCT: Preliminary results

Arsham Hamidi[1a], Yakub A. Bayhaqi[a], Ferda Canbaz[a], Alexander Navarini[b], Philippe C. Cattin[c], and Azhar Zam[2a]

[a]Biomedical Laser and Optics Group (BLOG), Dept. of Biomedical Engineering, University of Basel, Gewerbestrasse 14, 4123 Allschwil, Switzerland
[b]Dermatology, Dept. of Biomedicine, University of Basel, Hebelstrasse 20, 4031 Basel, Switzerland
[c]Center for medical Image Analysis and Navigation (CIAN), Dept. of Biomedical Engineering, University of Basel, Gewerbestrasse 14, 4123 Allschwil, Switzerland

ABSTRACT

Lasers have introduced many advantages to the medical field of osteotomy (bone cutting), however, they are not without drawbacks. The thermal side effects of laser osteotomy, in particular, affect a patient's healing process. Employing an irrigation system during surgery is a standard solution for reducing thermal damage to the surrounding tissue, but, due to the high absorption peak of water at the wavelength of Er:YAG laser (2.96 µm), accumulated water acts as a blocking layer and reduces the ablation efficiency. Therefore, irrigation systems would benefit from a high-speed and accurate feedback system to monitor the temperature changes in the tissue of interest. Phase-sensitive optical coherence tomography (PhS-OCT) is a highly sensitive method for measuring internal displacement (photothermal-induced expansion) during laser surgery. In this study, we utilized the integrated swept source PhS-OCT system (operating at a central wavelength of 1314 nm and with an imaging-speed of 104,000 A-scans/s) with an Er:YAG laser to detect localized phase changes induced by laser ablation irradiation and thereby quantify the photothermal-induced expansion of bone. The PhS-OCT system was calibrated by measuring the phase changes corresponding to the displacement of cover glass attached to a piezoelectric actuator (PA4HEW, Thorlabs) at different operating voltages. Furthermore, we explored how the induced photothermal expansion of bone changes when irradiated by different pulse energies. Using a PhS-OCT system to spatially and temporally resolve measurements of axial displacement of bone during laser surgery can play an important role in determining the corresponding temperature map, which can, in turn, offer feedback to the irrigation system in smart laser osteotomy.

Keywords: Optical coherence tomography, phase-sensitive OCT, smart laser osteotomy, photothermal-induced expansion

1. INTRODUCTION

There are distinct disadvantages to using conventional instruments like saws and drills for bone surgery. Among the may associated risks are the broadening of cuts, extensive heat deposition, mechanical traumatization, deposition of metal shaving, and bacterial contamination [1]. Laser osteotomy, in contrast, is an accurate, contactless and minimally invasive method for bone surgery. Studies have shown that during laser surgery, the porous structure of bone is preserved, which leads to an accelerated healing time [2]. The ablation mechanism of Er:YAG lasers is known as photothermal ablation [3]. The wavelength of the ablation laser coincides with one of the highest absorption peaks of water, at ~3 µm [4]. When the laser impinges the bone's surface, the heat transfers to water molecules present in the bone and increases the pressure in the bone's interstitial matrix, which finally leads to an explosion and, consequently, removal of tissue [5]. Nevertheless, if all of the water in the bone are vaporized, the organic constituents of bone are starting to carbonize with further laser exposure, thereby reducing the efficiency of ablation in laser osteotomy [6]. Although lasers induce less thermal damage to the surrounding tissue as compared to conventional instruments, controlling the accumulated temperature in tissue is still required to prevent any thermal damage to the surrounding tissue. The main thermal side effect in bone surgery is thermal osteonecrosis, defined as the death of bone tissue due to high temperature [7]. Several studies have shown that

---

[1]arsham.hamidi@unibas.ch ; phone +41 (0)61 207 54 62; dbe.unibas.ch
[2]azhar.zam@unibas.ch; phone +41 (0)61 207 54 60; dbe.unibas.ch

using an external irrigation system can prevent thermal osteonecrosis, such irrigation systems are considered to be the standard method for cooling tissue during bone surgery [8]. However, due to the high absorption peak of water at the Er:YAG wavelength, the water accumulated during continuous irrigation acts as a blocking layer, which reduces ablation efficiency. Therefore, a feedback system that monitors the temperature changes in tissue during laser ablation is required to control the irrigation system in a way that conserves the temperature of surrounding tissue below the critical temperature of 47°C [9], and enhances the efficiency of ablation.

To date, many techniques have been investigated for their potential to offer real-time temperature imaging with high resolution and high sensitivity. Directly measuring temperature with a thermocouple is the most accurate method, but it is invasive and often unfeasible during laser surgery. Infrared thermography is a real-time and non-invasive method, but is only capable of measuring superficial temperatures. Magnetic resonance imaging (MRI) can measure relative temperature changes with high accuracy and high resolution deep within living tissues. The proton resonance frequency of water is almost linearly related to temperature, but MRI cannot provide real-time temperature information [10, 11]. Ultrasound (US) has also been considered for real-time relative measurements of temperature at a depth of samples based on speckle tracking. Still, accuracy is poor due to native tissue motion artifacts and a limited range of measurements. Photoacoustic imaging can be used to measure temperature by tracking the temperature-induced changes in the optoacoustic (OA) signal amplitude (due to the dependence of the Grüneisen parameter on temperature) [12, 13]. Advanced OA volumetric temperature monitoring was performed with a three-dimensional OA imaging system consisting of a 512-element spherical transducer array, covering a 140° angle with a 4 cm radius of curvature, and spatial and temporal resolution of 150 μm and 10 ms, respectively [14]. However, OA monitoring is not able to show the temperature rise corresponding to each pulse during laser ablation, due to low temporal resolution in three-dimensional imaging. Optical coherence tomography (OCT) performs contactless, high-resolution, non-invasive, and volumetric imaging of the internal microstructure in biological tissue, by measuring backscattered or back-reflected light [15]. Conventional OCT imaging can be used to assess tissue deformation depending on the axial resolution of the OCT system. However, if the tissue deformation induced during laser surgery is in the order of microns or less, it may fall below the detection capabilities of structural OCT imaging. By analyzing the phase component of the OCT signal, phase-sensitive OCT (PhS-OCT) can provide much greater sample displacement sensitivity and direct quantitative measurements of the displacement due to photothermal-induced expansion of tissue [16-19].

In this study, we monitored the phase changes and corresponding displacement of bone during photoablation by a pulsed Er:YAG laser at different energy levels. First, we calibrated the PhS-OCT system with a cover glass attached to a piezoelectric actuator (PA4HEW, Thorlabs) to verify the displacement calculated from phase changes at different working voltages. Then, using an integrated PhS-OCT and Er:YAG laser system, we monitored the photothermal-induced expansion of bone in real-time.

2. MATERIALS AND METHOD

2.1 Integrated PhS-OCT system with laser ablation

In this experiment, we used a PhS-OCT system with a conventional fiber-based Michelson interferometer and an akinetic swept source laser from Insight (Insight Photonic Solution, Inc., Lafayette, Co, USA), as shown in Fig. 1. The laser source operates at a central wavelength of 1314 nm and spectral bandwidth of 61.5 nm. The axial and lateral resolution of the OCT system was 14 μm and 50 μm, respectively, while the sweep rate was set at 104 kHz. A dispersion compensator was placed in the reference arm to balance the dispersion induced by the telecentric lens in the sample arm. In the sample arm, the OCT beam was coaxially combined with the Er:YAG laser using a custom-made dichromatic mirror. A sapphire window was placed after the dichromatic mirror to protect the optical elements from debris generated during laser ablation. To investigate the thermal expansion of bone during ablation, we did not use an irrigation system in this experiment. To measure the photothermal-induced expansion, we set the PhS-OCT scanning parameter to record the B-scans continuously. At the same time, the center-of-line scan was positioned where the Er:YAG laser was focused on the sample. Hence, we were able to monitor the photothermal expansion in the surrounding tissue, as well. After each measurement, we monitored the sample using a thermal camera (FLIR A655sc, accuracy ±2°C) to ensure that the temperature of the sample had been reduced and was equal to room temperature. Then, by moving the sample using the translation stage, the next experiment was performed on the next intact point of the sample. It is also worth mentioning that all of the measurements were taken at the same distance (1 mm) from the center ablation area on the sample.
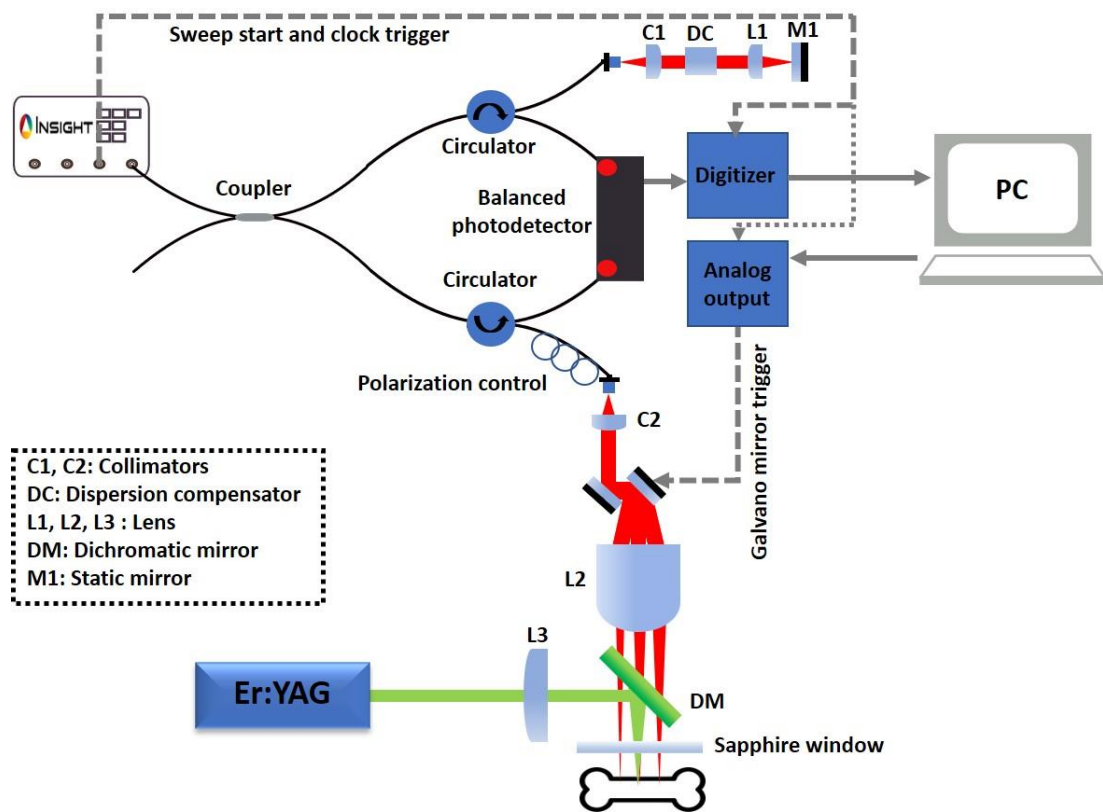
Figure 1. Schematic design of integrated PhS-OCT system with laser ablation to monitor the photothermal-induced expansion of bone. The PhS-OCT system operated at 1314 nm and 104 kHz A-scan rates and the center wavelength of the Er:YAG laser was 2.94 µm. The PhS-OCT system continuously recorded cross-sectional images during laser ablation.

2.2 Signal processing

Employing phase-sensitive OCT to measure fluctuation has been discussed and mathematically evaluated in earlier studies [20]. After dispersion compensation and DC subtraction, a Fourier transform was applied to the OCT interference spectrum $I(k)$ to get the interferogram $I(z)$ in the time-domain. This step is given as:

$$I(z) = FFT[I(k)] = A(z)\exp[i\Phi(z)]. \qquad (1)$$

In this equation, $A(z)$ is the amplitude and $\Phi(z)$ is the phase of the signal. The depth-resolved A-scan profile generated contains information about the sample in both amplitude and phase [21, 22], where the amplitude $A(z)$ is used to reconstruct the conventional OCT images. Both $A(z)$ and $\Phi(z)$ contain depth-resolved structural sample information; however, the main difference is that $A(z)$ cannot be used to measure any optical path length (OPD) variation smaller than the axial resolution of the OCT system. To determine the phase changes due to photothermal expansion, a pixel of interest was selected in the conventional OCT image and, then, phase changes in the pixel over time were evaluated by extracting phase information from consecutive frames. The physical path length difference (ΔL) is defined as:

$$\Delta L = \frac{\lambda_0 \Delta\Phi}{4\pi n}. \qquad (2)$$

Where, λ_0 is the central wavelength and n is the refractive index of the sample. Besides, the second Fourier transform of the unwrapped phase extracted from the complex OCT signal can be used to retrieve the phase changes:

$$\text{FFT}(\Delta\Phi(z,t)) = \frac{4\pi^2}{\lambda_0} . A . f_0 . \Delta t \rightarrow A = \frac{|p(f_0)|.\lambda_0}{4\pi^2 . f_0 . \Delta t}, \tag{3}$$

where $|p(f_0)|$ is the amplitude of the FFT peak and f_0 is the repetition rate of the laser ablation process. When measuring the induced photothermal expansion, either changes to the refractive index or expansion of bone due to localized heating can change the OPD. Both factors contribute to the variation of the interferometric phase, but it is not possible to distinguish the relative contribution of each factor, hence, both factors were considered together.

2.3 Calibration of PhS-OCT system

To prepare the sample for calibration of the PhS-OCT system, we fixed the piezoelectric actuator (PA4HEW, Thorlabs) to a holder. We attached a precision cover glass (170 µm thickness) on top of the actuator. First, we measured the displacement of the cover glass by using the PhS-OCT system as a function of the applied voltage, while considering the refractive index of the cover glass (1.51 at 1310 nm) and the time interval between frames (0.96 milliseconds). Here, we calculated the axial displacement using Eq. 2 and Eq. 3. Figure 2(a) shows the calculated displacement of the cover glass, using two methods, together with the displacement information provided by the datasheet. The resulting displacements were consistent with the datasheet provided by the piezoelectric actuator, as shown in Fig. 2(a). Then, to evaluate the performance of the PhS-OCT system, we ran the piezoelectric actuator at a fixed frequency of 10 Hz, with different applied voltages. Several B-scans (100 A-scans) recorded continuously the phase changes of the cover glass over time. Figure 2(b) shows the displacement of one pixel of the cover glass positioned on the top of the piezoelectric actuator over 0.2 seconds.
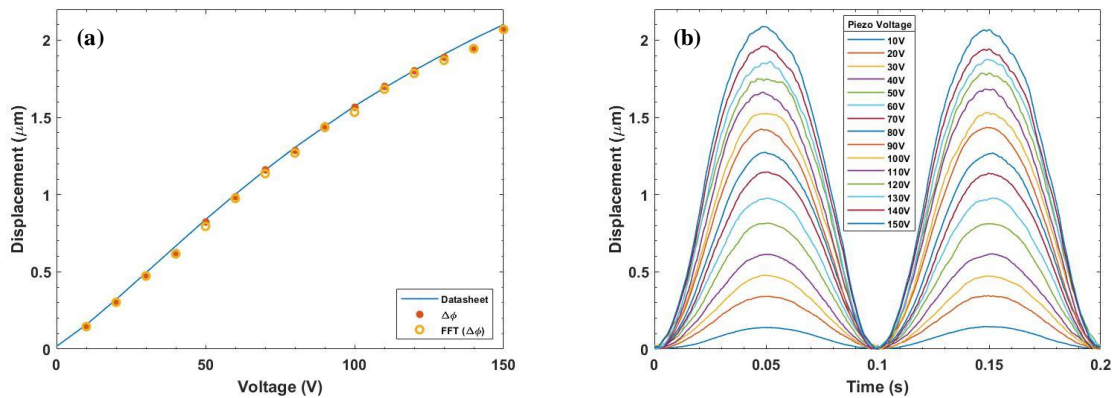

Figure 2. Calibration of the PhS-OCT system with the piezoelectric actuator. (a) Calculated displacement (based on Eq.2 and Eq.3) of cover glass attached to a piezoelectric actuator, together with the displacement information provided by the datasheet. (b) Time-resolved displacement of cover glass attached to the piezoelectric actuator at a frequency of 10 Hz and different voltages over 0.2 s, plots are laterally and axially positioned.

2.4 Imaging photothermal-induced expansion with the integrated setup

To measure the induced thermal expansion of bone with the integrated PhS-OCT and laser ablation system, we used a pig's femur bone as a sample. The soft tissues (fat, muscle, bone marrow) were completely removed. Then, the sample was washed to remove possible pollutants on the surface. The surface of the bone was cut to achieve a flat surface with respect to the optical axis of the OCT system. The thickness of the sample was 3.2 mm, and it was attached properly to the microscope cover slide to prevent any movement of the sample during laser ablation pulses. The pulse energy of the Er:YAG laser was measured with an energy meter (StarLite from Ophir Optronics) at different energy levels prior to the experiments. The ablation laser operated at a repetition rate of 10 Hz. Considering the refractive index of bone to be 1.51 at 1300 nm [23], we measured the axial expansion of bone using Eq. 2.

3. RESULTS AND DISCUSSION

Figures 3(a)-(d) show the phase changes and the corresponding photothermal expansion of bone acquired by PhS-OCT over 400 milliseconds (including four Er:YAG laser pulses) at different pulse energies. The time difference between frames (each frame included 200 A-scans) was 1.92 ms. In these figures, the initial phase has been set to zero to allow for better visualization of the amount of expansion per pulse. Figure 3(a) shows phase changes and axial expansion of bone due to 4 pulses from the Er:YAG laser (energy per pulse: 4.2 mJ). Each pulse follows a path of sharp expansion (increasing temperature) and gradually decreases (reducing temperature). Figures 3(b)–3(d) depict phase changes, and displacement of bone for different pulse energies of 43 mJ, 70 mJ and 128 mJ, respectively.
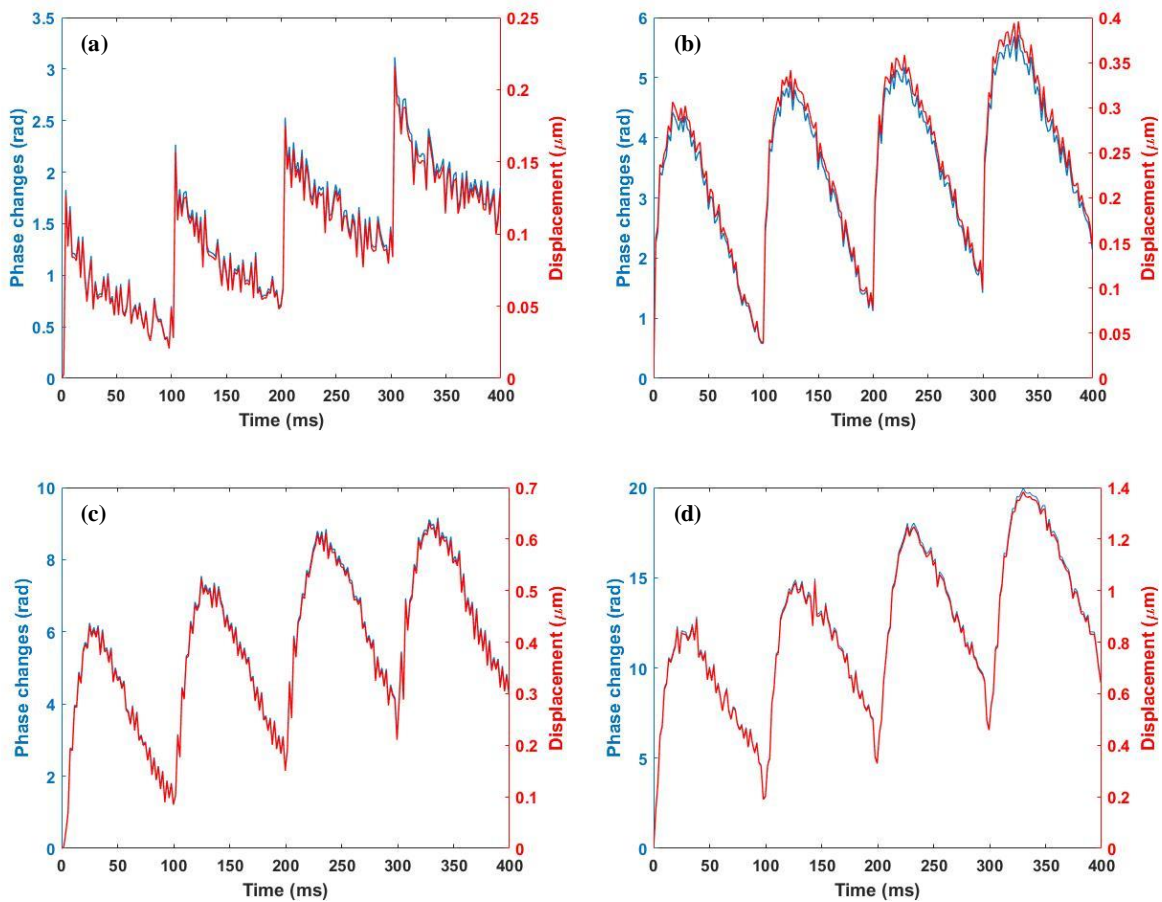
Figure 3. Monitoring the photothermal-induced expansion with PhS-OCT over 400 ms. Measurements were taken at the same distance from the center of the ablated area on the sample. (a) Shows the photothermal expansion of bone after four pulses from the Er:YAG laser, with a pulse energy of 4.2 mJ and a 10 Hz repetition frequency. (b), (c) and (d) show photothermal expansion during ablation with energies per pulses of 43 mJ, 70 mJ and 128 mJ, respectively. The initial phase has always been set to zero.

An increasing trend over 400 ms (four pulses) can clearly be seen from Figs. 3(a)-(d), indicating either accumulated temperature or changes in the refractive index of the sample. Figure 4 represents the average peak expansion over four pulses with different pulse energies. At low energy levels, the average peak expansion and energy level follow a linear trend. In contrast, at higher energy levels (more than 43 mJ), the average peak displacement is smaller than the amount of energy per pulse transferred to the sample.

In this study, we investigated the induced photothermal expansion of dehydrated bone. However, to make use of the PhS-OCT system to measure axial displacements and the resulting temperature changes of hydrated bone, proper calibration of the volumetric thermal expansion coefficient of bone and water is needed (the volumetric thermal expansion coefficient of water changes by approx. 50% between 20ºC and 30ºC).
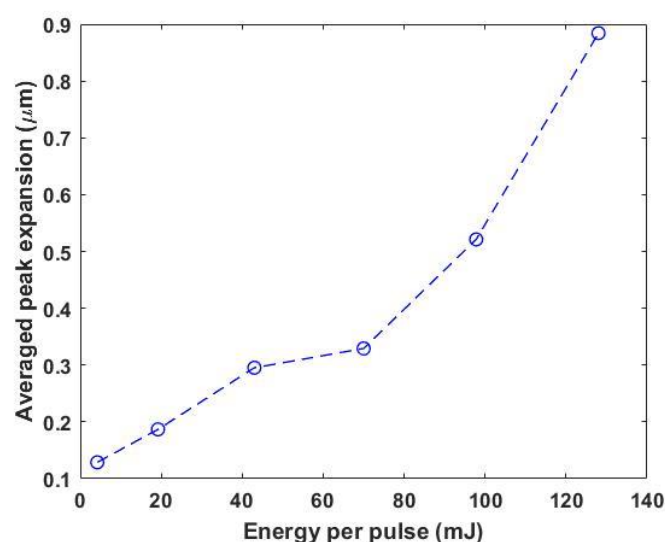

Figure 4. Averaged peak expansion of dehydrated bone over four pulses irradiated at different energy levels of the Er:YAG laser.

4. CONCLUSION

In smart laser osteotomy, a proper irrigation system is required to prevent thermal damage to surrounding tissue. To collect feedback for adjusting the amount of water applied to the tissue, we suggest using a phase-sensitive OCT system. Optimizing the amount of water will increase ablation efficiency and prevent thermal damage to surrounding tissues. Our experiments demonstrated the feasibility of using a PhS-OCT system to detect photothermal-induced expansion both in time and space, as feedback for laser surgery. Conventional OCT images cannot detect axial displacements less than its axial resolution. However, in this study, we showed that the PhS-OCT system is capable of detecting displacements at the scale of nanometers. In conclusion, with proper calibration of the volumetric thermal expansion coefficient of hydrated bone, PhS-OCT can be used as a feedback system for irrigation set-ups in smart laser osteotomy, leading to increased ablation efficiency and reduced thermal damage to surrounding tissue.

ACKNOWLEDGMENT

REFERENCES

[1] Eyrich, Gerold KH, "Laser-osteotomy induced changes in bone," Medical Laser Application 20(1), 25-36 (2005).
[2] Baek, Kyung-won, et al., "A comparative investigation of bone surface after cutting with mechanical tools and Er: YAG laser," Laser in surgery and medicine 47(5), 426-432 (2015).
[3] Tuchin, V., "Tissue optics and photonics: Light-tissue interaction II," Biomedical Photonics and Engineering 2(3), 030201 (2016).

[4] Vogel, Alfred, and Vasan Venugopalan, "Mechanisms of pulsed laser ablation of biological tissues," Chemical reviews 103(2), 577-644 (2003).

[5] Bernal, Lina M. Beltrán, et al., "Performance of Er: YAG laser ablation of hard bone under different irrigation water cooling conditions," Proc. SPIE 10492, 104920B (2018).

[6] Ansari, Mohammad Ali, Mohsen Erfanzadeh, and Ezeddin Mohajerani, "Mechanisms of laser-tissue interaction: II. Tissue thermal properties," Journal of laser in medical science 4(3), 99 (2013).

[7] Timon, Charles, and Conor Keady, "Thermal Osteonecrosis Caused by Bone Drilling in Orthopedic Surgery: A Literature Review," Cureus 11(7), (2019).

[8] Augustin, Goran, et al., "Thermal osteonecrosis and bone drilling parameters revisited," Archives of orthopaedic and trauma surgery 128(1), 71-77 (2008).

[9] Augustin, Goran, et al., "Temperature changes during cortical bone drilling with a newly designed step drill and an internally cooled drill," International orthopaedics 36(7), 1449-1456 (2012).

[10] Ishihara, Yasutoshi, et al., "A precise and fast temperature mapping using water proton chemical shift," Magnetic resonance in medicine 34(6), 814-823 (1995).

[11] Quesson, Bruno, Jacco A. de Zwart, and Chrit TW Moonen, "Magnetic resonance temperature imaging for guidance of thermotherapy," Journal of Magnetic Resonance Imaging: An Official Journal of International Society for Magnetic Resonance in Medicine 12(4), 525-533 (2000).

[12] Larina, Irina V., Kirill V. Larin, and Rinat O. Esenaliev, "Real-time optoacoustic monitoring of temperature in tissues," Journal of Physics D: Applied: Applied Physics 38(15), 2633 (2005).

[13] Schüle, Georg, et al. "Noninvasive optoacoustic temperature determination at the fundus of the eye during laser irradiation," Journal of biomedical Optics 9(1), 173-180 (2004).

[14] Landa, Francisco Javier Oyaga, et al. "Volumetric optoacoustic temperature mapping in photothermal therapy," Scientific reports 7(1), 1-8 (2007).

[15] Fujimoto, James G., et al., "Optical coherence tomography: an emerging technology for biomedical imaging and optical biopsy," Neoplasia (New York, NY) 2(1-2), 9 (2000).

[16] Zhao, Yonghua, et al., "Phase-resolved optical coherence tomography and optical Doppler tomography for imaging blood flow in human skin with fast scanning speed and high velocity sensitivity," Optics letters 25(2), 114-116 (2000).

[17] Adler, Desmond C., Robert Huber, and James G. Fujimoto., "Phase-sensitive optical coherence tomography at up to 370,000 lines per second using buffered Fourier domain mode-locked lasers," Optics letters 32(6), 626-628 (2007).

[18] Müller, Heike H., et al., "Imaging thermal expansion and retinal tissue changes during photocoagulation by high speed OCT," Biomedical optic express 3(5), 1025-1046 (2012).

[19] Choma, Michael A., et al., "Spectral-domain phase microscopy," Optics letters 30(10), 1162-1164 (2005).

[20] Adler, Desmond C., et al., "Photothermal detection of gold nanoparticles using phase-sensitive optical coherence tomography," Optics express 16(7), 4376-4393 (2008).

[21] Hu, Yong, Adrian Podoleanu, and George Dobre, "Photothermal optical coherence tomography for investigation and imaging photothermal trapping of gold nano-rods in clear media and biological tissue," Journal of Optics 21(9), 095301(2019).

[22] Tucker-Schwartz, J. M., et al., "In vivo photothermal optical coherence tomography of gold nanorod contrast agents," Biomedical optic express 3(11), 2881-2895 (2012).

[23] Rahlves, M., et al., "Towards refractive index corrected optical coherence tomography as a navigation tool for bone surgery," The European Conference on Laser and Electro-Optics International Quantum Electronics Conference, CL_P_2 (2013).

4.2 Towards phase-sensitive optical coherence tomography in smart laser osteotomy: temperature feedback

The second publication in this chapter demonstrates the use of the calibrated phase-sensitive OCT system for temperature feedback during laser osteotomy. The preliminary results show that the calibrated correlation between photothermal expansion and its corresponding temperature can be used to predict temperature rise in bone tissue.

ORIGINAL ARTICLE

Towards phase-sensitive optical coherence tomography in smart laser osteotomy: temperature feedback

Arsham Hamidi[1] · Yakub A. Bayhaqi[1] · Ferda Canbaz[1] · Alexander A. Navarini[2] · Philippe C. Cattin[3] · Azhar Zam[1,4,5]

Abstract

Thermal effects during bone surgery pose a common challenge, whether using mechanical tools or lasers. An irrigation system is a standard solution to cool the tissue and reduce collateral thermal damage. In bone surgery using Er:YAG laser, insufficient irrigation raises the risk of thermal damage, while excessive water lowers ablation efficiency. This study investigated the potential of optical coherence tomography to provide feedback by relating the temperature rise with the photo-thermal expansion of the tissue. A phase-sensitive optical coherence tomography system (central wavelength of $\lambda=1.288$ μm, a bandwidth of 60.9 nm and a sweep rate of 104.17 kHz) was integrated with an Er:YAG laser using a custom-made dichromatic mirror. Phase calibration was performed by monitoring the temperature changes (thermal camera) and corresponding cumulative phase changes using the phase-sensitive optical coherence tomography system during laser ablation. In this experiment, we used an Er:YAG laser with 230 mJ per pulse at 10 Hz for ablation. Calibration coefficients were determined by fitting the temperature values to phase later and used to predict the temperature rise for subsequent laser ablations. Following the phase calibration step, we used the acquired values to predict the temperature rise of three different laser-induced cuts with the same parameters of the ablative laser. The average root-mean-square error for the three experiments was measured to be around 4°C. In addition to single-point prediction, we evaluated this method's performance to predict the tissue's two-dimensional temperature rise during laser osteotomy. The findings suggest that the proposed principle could be used in the future to provide temperature feedback for minimally invasive laser osteotomy.

Keywords Optical coherence tomography · Phase-sensitive OCT · Laser ablation · Laser osteotomy

✉ Arsham Hamidi
  Arsham.hamidi@unibas.ch

  Azhar Zam
  Azhar.zam@nyu.edu

1   Biomedical Laser and Optics Group (BLOG), Department of Biomedical Engineering, University of Basel, CH-4123 Allschwil, Switzerland

2   Digital Dermatology, Department of Biomedical Engineering, University of Basel, CH-4123 Allschwil, Switzerland

3   Center for Medical Image Analysis and Navigation (CIAN), Department of Biomedical Engineering, University of Basel, CH-4123, Allschwil, Switzerland

4   Division of Engineering, New York University Abu Dhabi, Abu Dhabi 129188, UAE

5   Tandon School of Engineering, New York University, Brooklyn, NY 11201, USA

Introduction

Osteotomy (bone surgery) is a surgical intervention involving machining processes such as drilling, sawing, and grinding the bone [1]. The mechanical stress that conventional tools apply to the surface of the bone is associated with several disadvantages, including poor surface evenness, limited cutting geometry, and extensive heat deposition [2]. Laser osteotomy, the proclaimed successor of mechanical saws and chisels, has the potential to revolutionize osteotomy. The unique advantages of using lasers, such as non-contact intervention, faster healing time, and the possibility of performing unrestricted cutting geometries, have garnered significant interest in applying this technology in medical settings [3–8]. Cortical bone is composed of approximately 13% water, 60% mineral in the form of hydroxyapatite crystallites, and 27% of organic matrix [9]. The absorption peak of different constituents of bone tissue in the mid-infrared

wavelength range makes these lasers interesting for the ablation of bone tissue. For instance, CO_2 laser at 10.6 μm with a high absorption peak in mineral composition and Er:YAG laser at 2.94 μm with a high absorption peak in water's spectrum [10]. The ablation process with Er:YAG lasers assisted by water improves the ablation efficiency and surface morphology [11]. Several studies have shown the advantages of using Er:YAG lasers generating microsecond pulses to achieve deep bone ablation with minimum collateral thermal damage to the surrounding tissue. Laser ablation using an Er:YAG laser is known as photothermal ablation, where following the high absorption of the Er:YAG laser pulse in bone tissue, transferred energy to water molecule builds high pressure (~several hundred bars) which leads to a series of micro explosions by vaporization and consequently the removal of bone tissue [12–14]. Although this laser-tissue interaction can minimize collateral thermal damage and achieve a deeper cut, it also quickly dries out the surrounding tissue and can cause thermal damage [15]. Generally, photothermal damage can be divided into two main categories: reversible effects, such as hyperthermia, and irreversible damages, which encompass coagulation, vaporization, carbonization, and melting. The denaturation of proteins (coagulation) arises when the temperature within biological tissue reaches ≅60°C. Localized temperature increases beyond 100 °C result in tissue vaporization, and when this vaporization process exhausts the tissue's water content, it transforms the organic compounds of the tissue into carbon (carbonization) [16]. Melting occurs at temperatures surpassing 300°C. Consequently, irrigation is required during laser osteotomy to rehydrate and prevent thermal damage to the surrounding critical tissues [17]. However, because of the high absorption of Er:YAG laser in water, an excessive amount of water will work as a protective layer by absorbing the energy of the laser pulses, thereby reducing ablation efficiency [18]. To overcome this challenge, a non-contact feedback system is required to allow for pulsed irrigation instead of continuous irrigation during laser osteotomy.

To date, many methods have demonstrated potential for measuring temperature changes during laser treatments in cases where ablation (tissue removal) is not involved. These methods include magnetic resonance thermal imaging (MRTI), fiber optic sensors (FOS), and ultrasound (US) among others [17, 19–21]. Among these methods, the optoacoustic (OA) technique has shown promising results for achieving non-contact temperature measurements [22]. OA uses short laser pulses to generate pressure waves in the tissue. The Grüneisen parameter, a dimensionless parameter, is proportional to an increase in the pressure of the produced acoustic wave [23]. OA leverages the linear relation between the temperature and the tissue's Grüneisen parameter for temperature measurement. This accuracy could be enhanced through tissue-specific calibration. Volumetric OA

temperature mapping has demonstrated potential for utilization in photothermal therapy [24]. However, there are some drawbacks associated with temperature measurement using OA during laser surgery. These include poor axial and lateral resolution, a low acquisition rate for 3D measurements, and dependence on the repetition rate of the ablative laser. It should be noted that the accuracy of these methods has only been investigated below the coagulation temperature of the biological tissue. For temperatures exceeding 50 °C, there is non-linearity in the Grüneisen parameter and changes in the optical properties (absorption and scattering coefficients) of the tissue [25]. Consequently, the ability of OA techniques to accurately predict the temperature is limited to temperatures below the coagulation threshold. Optical coherence tomography (OCT) is another method with proven potential to measure temperature changes of tissue based on its photothermal expansion. OCT is a non-invasive, high-resolution, non-contact, and high-speed interferometric imaging technique capable of producing three-dimensional images of biological tissue based on the particular optical scattering properties of the various tissues [26, 27]. Recent studies have extensively investigated the advantages of using OCT integrated with laser ablation as a visual feedback system [28–30]. Phase-sensitive OCT (PhS-OCT) is an extension of conventional OCT that can detect axial deformation beyond its axial resolution, with high sensitivity and temporal resolution [12, 31, 32]. The high sensitivity of PhS-OCT makes it possible to detect the induced thermal expansion of the tissue caused by the absorption of the laser's pulse energy during laser surgery. Therefore, the dependency of the optical path difference (OPD) on temperature can be used for photothermal tissue imaging during thermal therapy. Recent studies have proven PhS-OCT's capacity to predict the temperature of a given sample for low-temperature changes (below the coagulation threshold) [33–36].

Although OCT's potential to measure tissue temperature rise in the laser coagulation regime has been well-investigated, further investigation is required to predict the tissue's temperature rise in the more complicated laser ablation regime. In this work, the principle of temperature rise of bone tissue during laser ablation using an Er:YAG laser is investigated. Followed by the proposed thermal model, a calibrated phase-sensitive OCT system that could potentially trigger the irrigation system by detecting the highest temperature in the area surrounding the laser-induced cut is introduced.

Methods

Figure 1 shows a schematic of the principles for a temperature rise of bone during laser ablation. The Gaussian distribution of the Er:YAG laser's energy results in
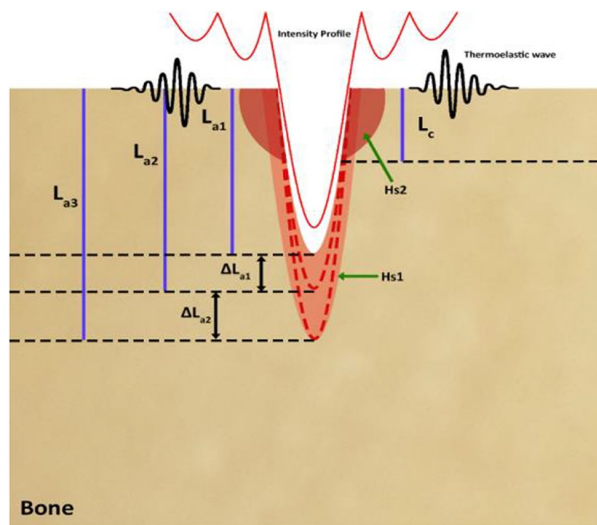
Fig. 1 Schematic of the temperature rise of bone during laser ablation. Hs1 indicates the infinite number of heat disk sources, Hs2 represents the heat source on the surface of the bone. L_a, ΔL_a, and L_c are ablation depth, effective heat depth after ablation pulse, and effective heat depth on the surface of the bone, respectively

a cone-shaped ablation of the bone (Fig. 1). The geometry of the laser-induced cut denoted that the ablation volumes within the cut were not constant. Consequently, in a sequence of laser pulses, the difference between the ablated areas could be considered as an infinite number of disk heat sources, which is denoted by Hs1 in Fig. 1. This effect is similar to the friction between the drill bit and the wall of the cut, in traditional bone surgery [37]. The radius of the disk-shaped heat sources is equivalent to the laser-induced crater. In addition to the heat distribution from the borders of the cut, Er:YAG lasers often suffer from a low beam quality factor (M^2), leading to the heating of an extended area on the bone's surface. It measures the spatial distortion level of a laser beam in comparison to an ideal Gaussian beam of the same wavelength, with a value closer to 1 indicating a higher resemblance to the ideal Gaussian beam. In this study, the beam quality factor is measured as $M^2 = 22$, which results in heating an extended area on the bone, beyond the borders of the laser-induced cut (Hs2 in Fig. 1) [38]. Hs2 indicates the heat source on the bone's surface. The effective heat-diffusion length during a single laser pulse, ΔL_a, was defined as $\Delta L_a \sqrt{4Dt_p}$, in which t_p is the laser pulse-width, and D stands for the diffusion constant of the tissue [39]. Thermoelastic waves induced by absorbed laser energy, ablation depth (L_a), effective heat source in between laser pulses (ΔL_a), and effective heat depth induced by sidelobes of laser (L_c) are also shown in Fig. 1.

Induced temperature rise

The mechanism of hard tissue ablation using an Er:YAG laser can be considered a "photo-mechanical" procedure [40]. For bovine cortical bone, the effective heat-diffusion length (pulse duration of 300 μs) and laser penetration depth using an Er:YAG laser (λ=2.94 μm) are 18.6 μm and 4 μm, respectively [38, 41]. The beam size of the Er:YAG laser measured as 2.5 mm at the focal plane. Considering the cutting width of 1.1 mm on the surface of the bone, the heat source on either side of the crater was around 0.85 mm. Therefore, for the Hs2, due to the larger beam size value compared to penetration depth, the axial distribution of the heat (T_{axial}) is more effective and the temperature profile followed an exponential-like decay in the axial direction (Beer-Lambert law). However, for Hs1, which indicates the infinite number of heating disks, the spot size was assumed to be comparable to or less than the laser penetration depth, which meant that radial heat distribution (T_{radial}) is dominant and followed a radial distribution of temperature. It is worth mentioning that in the proposed thermal model, it was assumed that the energy of the laser pulse is mainly consumed for tissue removal. Therefore, the temperature at any point in the tissue during laser osteotomy could be considered as follows:

$$T = T_{axial} + T_{radial} \tag{1}$$

To determine the temperature rise (axial and radial) induced by these heat sources over time ($\Delta T(r,t)$), an analytical solution of the heat diffusion equation was used as follows [42]:

$$\frac{\partial \Delta T(r,t)}{\partial t} - \alpha \nabla^2 \Delta T(r,t) = \frac{Q_{res}}{\rho_0 c_p} \tag{2}$$

In equation (2), α is the thermal diffusivity, ρ_0 density and c_p stands for the heat capacity of the bone tissue. To define the temperature rise of the tissue using equation (2), some parameters need to be considered. The residual heat that causes tissue temperature rise (Q_{res}) is difficult to measure inside a laser-induced cut. Furthermore, specific parameters should be known in advance. For instance, the water content in a human femur cortical bone varies between 21 and 17 % for humans aged 5 and 95 years old, respectively [43]. Furthermore, the micro-structural attributes of bone, including the size of pockets or pores within its structure, play an important role in affecting ablation efficiency. This influence arises from the changes in bone tissue's thermal conductivity. The presence of water within bone can be found associated with mineral phase or free water (bulk water) [44, 45]. The pores within the calcified matrix are filled with bulk water, creating a network of interconnected channels. Consequently, these pores

could serve as escape routes for laser-generated vapor, reducing pressure buildup that has the potential to diminish ablation efficiency [46]. Due to the aforementioned shortcomings, alternative solutions were sought for a tissue-specific calibration method.

Phase-sensitive OCT

PhS-OCT is a functional OCT-based technique that can detect the axial deformation of a sample with a higher degree of accuracy than its axial resolution. PhS-OCT can provide additional contrast to conventional OCT images in terms of tissue changes over time. For this purpose, a highly phase-stable OCT system is required to isolate the changes in the phase of the tissue under investigation. In general, although spectral-domain OCT (SD-OCT) demonstrates higher inherent phase stability, faster imaging speed, and lower effect of fringes washout make SS-OCT more interesting for PhS-OCT applications [47]. Nevertheless, the mechanical principle of sweeping the wavelength in conventional swept lasers, such as polygonal scanning mirrors, and microcavity tunable lasers with microelectromechanical systems (MEMS), causes lower phase stability compared to the SD-OCT [48]. It is worth mentioning that several studies reported software and hardware-based solutions to improve the phase-stability of the measurements [49]. In this study, an akinetic swept source is utilized which provides a high-phase stability by eliminating the mechanical part, providing high-phase stability without the need for further post-processing.

During laser osteotomy, the tissue absorbs high-power laser energy and results in generation of heat. Consequently, the tissue expands and the optical path difference (OPD) changes on the surface of the tissue. At first, only the changes in OPD induced by Hs2, the heat source on the surface of the bone, are considered. The measured phase changes correspond to the integral of the refractive index within the depth of the tissue.

$$OPD(T_0) = \int_0^{L_0} n(T)dz = n(T_0)L_0 \tag{3}$$

where $n(T_0)$ is the sample refractive index at the initial temperature, T_0, and L_0 is the physical length of the sample. Assuming that the refractive index and the thermal expansion coefficient of bone tissue change linearly over time [50]:

$$n(T) = n(T_0) + \frac{dn}{dT} \Delta T(z), \beta(T) = \beta(T_0) + \frac{d\beta}{dT} \Delta T(z) \tag{4}$$

In addition, internal acoustic stress induced by the ablative laser causes thermoelastic deformation, which can be written as:

$$\rho \frac{\partial^2 u}{\partial t^2} - \frac{E}{2(1+v)}\nabla^2 u - \frac{E}{2(1+v)(1-2v)}\nabla(\nabla.u) = \frac{-E\beta}{3(1-2v)}\nabla(\Delta T) \tag{5}$$

In equation (5), ρ is the density of the tissue, u is the displacement, E is Young's modulus, v stands for the Possion ratio, β is the thermal expansion coefficient, ΔT is temperature changes, and ∇ defines the displacement in the volume [51]. At the end of the acoustic stress, a quasi-steady-state equilibrium settles in. Therefore, the first term in equation (5) can be considered as zero. Then, the thermoelastic displacement can be described as:

$$u_z = \frac{\beta(1+v)}{3(1-v)}\int_0^L \Delta T dz \tag{6}$$

Therefore, the total tissue displacement can be derived from the summation of the thermo-optic and thermo-elastic terms. J. Kim et al., reported that in this thermal model, considering the axial temperature profile of the tissue heated by laser (Beer-Lambert law, $\Delta T(z) = \Delta(T_0)\exp(-\mu_a z)$), axial displacement $\delta(T)$ can be written as [35]:

$$
\begin{aligned}
\delta(T) = {} & n_{T_0} \times L(T_0) + \left[n_{T_0}\frac{1+v}{3(1-v)}\beta(T_0) + \frac{dn}{dT}\right] \\
& \times \frac{\exp(-\mu_a L(T_0))}{-\mu_a} T_0 + \left[n_{T_0}\frac{d\beta}{dT} + \frac{dn}{dT}\beta(T_0)\right] \\
& \times \frac{1+v}{3(1-v)}\frac{\exp(-\mu_a L(T_0))}{-2\mu_a} T_0^2 \\
& + \left[\frac{dn}{dT}\frac{1+v}{3(1-v)}\frac{d\beta}{dT}\frac{\exp(-3\mu_a L(T_0))}{-3\mu_a}\right]\Delta T_0^3 = c_{a0} \\
& + c_{a1}\Delta T_0 + c_{a2}\Delta T_0^2 + c_{a3}\Delta T_0^3
\end{aligned}
\tag{7}
$$

In equation (7), C_{a0}, C_{a1}, C_{a2}, and C_{a3} are constant terms to correlate the optical path difference to the corresponding temperature rise induced by the ablative laser. Changes in the phase ($\Delta\varphi$) in PhS-OCT can be converted as $\delta = \frac{\lambda_0 \Delta_\varphi}{4\pi n}$.

For Hs2, where the conic-shaped laser-induced cut showed an infinite number of disk-heat sources, equation (4) for a specific depth could be written in a cylindrical coordinate. This indicated that the axial temperature profile (equation (7)) was modified by Hs2, which is a depth-dependent parameter; thus, the contribution of Hs2 adds more complexity to describing the bone's axial temperature profile during laser ablation. Therefore, in this study, a calibrated PhS-OCT method capable of predicting the axial temperature profile of bone tissue induced by Hs1 and Hs2 is introduced. Equation (8) shows a simplified contribution of Hs1 and Hs2, which leads to the heat-induced displacement ($\delta'(T)$) of tissue:
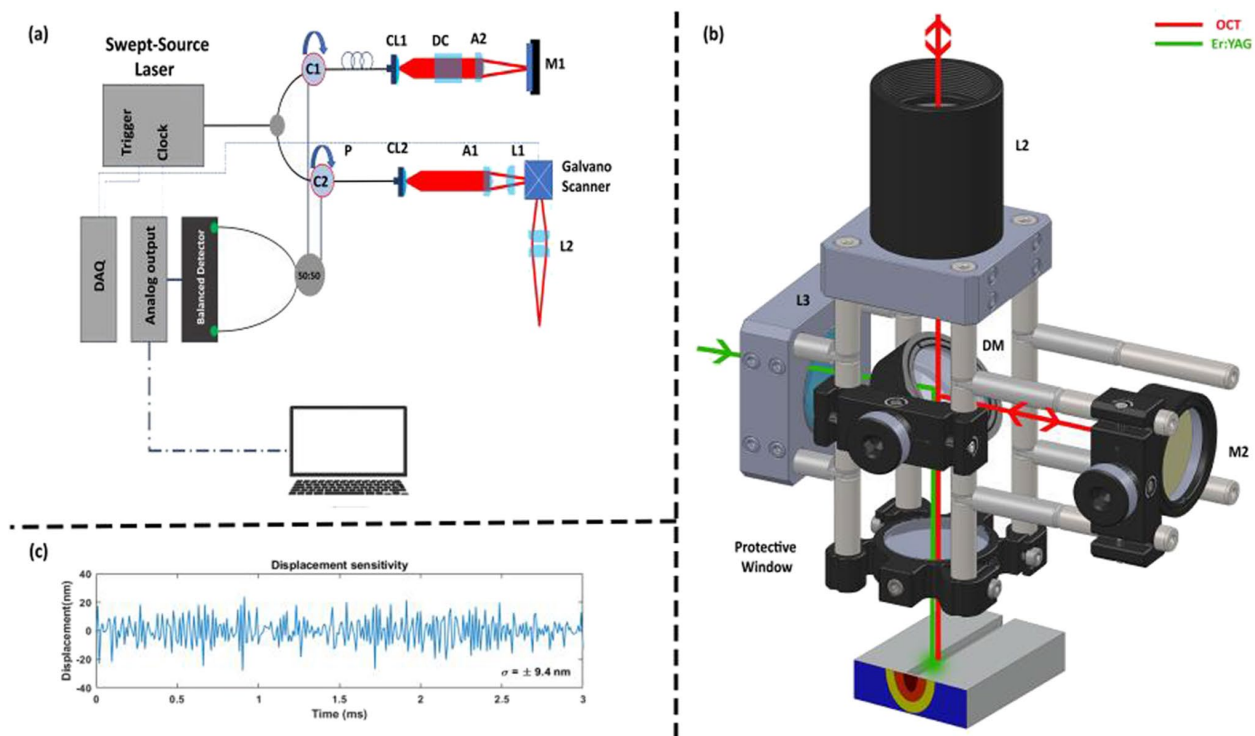
Fig. 2 Schematic of the optical setup of the PhS-OCT system. **a** Schematic of the BLB-OCT system. **b** Integrated phase-sensitive OCT system and the ablative laser for PhS-OCT. P (polarization controller), CL (collimator), M1 and M2 (mirrors), A1 and A2 (axicon lens, apex angle of two degrees), L1 (achromatic lens, f=75 mm), L2 (achromatic pair lens, f=100 mm), and DM (custom-made dichromatic mirror)

$$\delta'(T) = \left[C_{a0} + C_{Q0}\right] + \left[C_{a1} + C_{Q1}\right]\Delta T_0 \\ + \left[C_{a2} + C_{Q2}\right]\Delta T_0^2 + \left[C_{a3} + C_{Q3}\right]\Delta T_0^3 \tag{8}$$

Experimental setup and signal processing

A simple configuration of the tissue-specific PhS-OCT system is presented in Fig. 2, where Fig. 2a shows the Bessel-like beam OCT (BLB-OCT) system and Fig. 2b illustrates the modified sample arm for the PhS-OCT system. The configuration of the BLB-OCT has been described in [29]. The swept-source laser utilized in this experiment was a programmable akinetic swept-source laser (Insight Photonic Solutions, Inc.) with a central wavelength of $\lambda_0 = 1288$ nm, a bandwidth of 60.9 nm, sweep rate of 104.17 kHz, and sample clock of 400 MHz (50% duty cycle). OCT's wavelength is selected based on the density and highly scattering characteristics of bone and its components [44, 45]. This wavelength range exhibits less scattering and absorption compared to shorter wavelengths. The conjunction of reduced scattering and absorption, combined with the deeper penetration depth into bone tissue facilitated by BLB's extended depth of focus, guarantees improved image contrast.

Imaging parameters were selected to provide sufficient speed, image quality, and imaging range, which are crucial features for a visual feedback system in laser osteotomy. The arrangement of the BLB-OCT system, shown in Fig. 2a, included two circulators (C1, C2) that directed the light to the sample arm and to the reference arm while also delivering the light collected from both arms to the balanced photodetectors (PDB480C-AC Thorlabs). In the reference arm, the polarization controller, collimator lens (F260APC-C, Thorlabs), dispersion compensation, axicon lens (AX-122C, apex angle of two degrees, Thorlabs), and mirror are represented by P, CL1, DC, AL, and M1, respectively. In the sample arm, the collimator lens, axicon lens (same as the reference arm), achromatic doublet lens (f=75 mm, AC127-075-C, Thorlabs), and achromatic pair lens ($f = 100$ mm, Edmund optics, #47-302) are sequentially indicated by CL2, A2, L1, and L2. In Fig. 2b, the Er:YAG laser combined with the OCT laser using a custom-made dichromatic mirror (DM, 97% reflection at 2.94 μm, and transmission of $> 90\%$ at 1300 ± 75 nm), and focused on the sample using a f =75 mm calcium fluoride lens (L3, L5042, Thorlabs). The standard deviation of the phase sensitivity measured using a microscope glass slide (1 mm) is measured as $\approx \pm 9.16$ radians over 3 ms.

Figure 2c illustrates the corresponding measured displacement sensitivity with a standard deviation of ± 9.4 nm.

To calibrate the tissue-specific PhS-OCT, phase information (using PhS-OCT) and the value of the temperature rise should be recorded simultaneously. In this experiment, a thermal camera is used as a reference. Despite the difference in the pixel sizes of these systems, to the best of our knowledge, an infrared camera is a standard technology that can remotely measure the temperature rise in the ablation regime ($T > 50°C$). The region of interest in selected based on the reference point (ablation crater) and correlation of the pixel sizes in both systems (170-µm thermal camera, 18 µm OCT). Then, the raw data from the PhS-OCT system and the thermal images from the thermal camera were recorded continuously, starting just before laser ablation, and ending when the sample returned to room temperature. The pre-processing steps for the PhS-OCT included background subtraction, spectral shaping, and fast Fourier transformation. Then, to evaluate the phase changes, phase information of the sequential A-scans between the frames (1000 A-scans) was extracted and converted to the axial displacement. To remove the bulk phase fluctuation, cumulative phase information on the sample was subtracted from the reference value acquired by the calibration arm in Fig. 2b. To compare the temperature, rise and phase changes within the lasing window, a re-sampling was performed so that both systems would have the same sampling rate. Finally, by fitting a polynomial of degree three to the cumulative phase and temperature, the constants mentioned in equation (8) are determined. Having calculated a constant parameter with which to correlate temperature rise and cumulative phase change, the temperature rise corresponding to the phase change using the fzero function in Matlab software (version R2021b) is estimated.

Tissue-specific phase calibration

Equation (8) denotes the correlation between the temperature rise and changes in the optical path length. Once the fitted coefficient has been established, the temperature rise of the bone at the same depth as the laser-induced during the calibration step can be calculated. Consequently, the calibration coefficient could be used in place of the thermal camera to predict the temperature rise of the bone. The unique advantage of the proposed tissue-specific calibration method is that allows temperature rise of a sample without any initial information about the tissue.

Sample preparation

For this study, bovine femur slices were purchased from a local supermarket. The soft tissue was removed, and the bone was frozen for one day. Then, the edges of each bone were flattened using a bone saw. Ablating bone on the flattened edge made it possible to monitor the temperature inside the bone tissue. After cutting, each bone was washed carefully with tap water to remove surface debris.

Results

Figure 3 illustrates the photothermal expansion of the bone during laser osteotomy using an Er:YAG laser with a repetition rate of 10 Hz and an energy per pulse of 230 mJ. Figure 3a shows the intensity-based images of the recorded laser-induced cuts. The line at the bottom of the image represents the reference line, which was used to remove phase fluctuation. Figure 3b illustrates the extracted A-scan (red dashed line in Fig. 3a) from a sequence of B-scans over time (M-scan), and Fig. 3c corresponds to a zoomed-in version of Fig. 3b, where induced displacement by absorption of the laser pulse energy is visible.

As mentioned above, during the calibration process, simultaneous recording of the bone's phase change and temperature change during laser osteotomy is required. Figure 4a demonstrates the calibration process performed on the bone, where the x-axis is the recorded temperature difference, and the y-axis shows the axial displacement.

In Figure 4a, the red line shows the polynomial degree three, which correlates the cumulative axial displacement
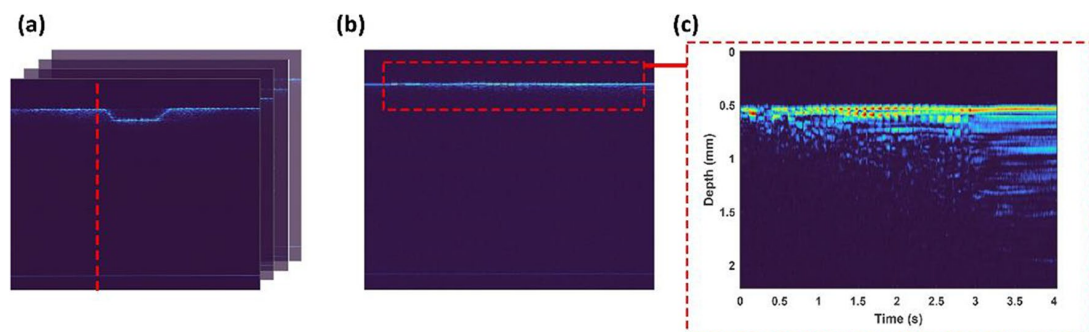
Fig. 3 Induced photothermal expansion of the bone during laser osteotomy. **a** intensity-based image, **b** M-scan image corresponds to the A-scan illustrated by dashed red-line in **a** over time, and **c** magnified photo of the induced displacement of the bone tissue from **b**
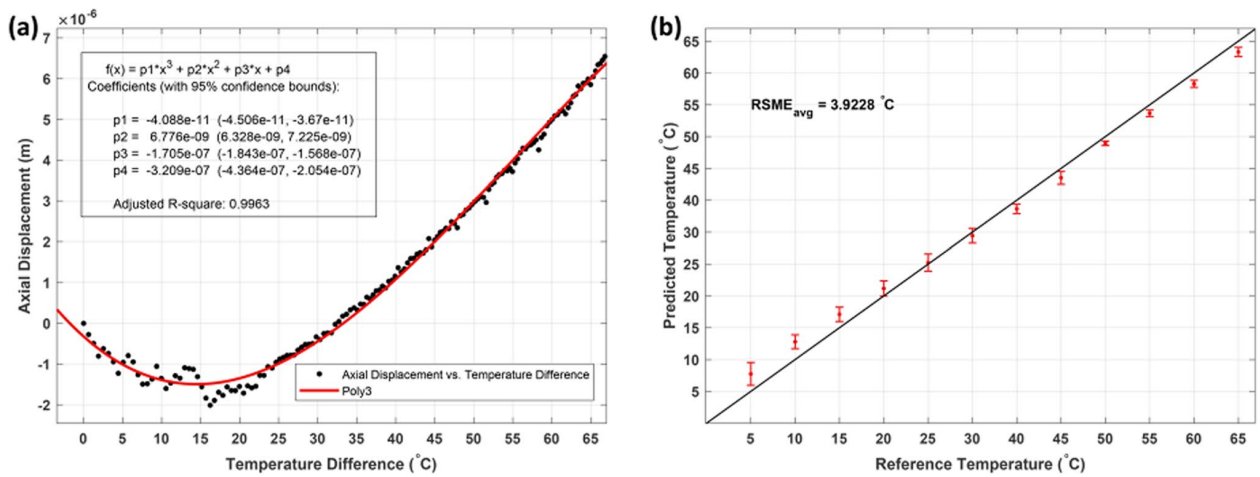
Fig. 4 **a** Polynomial of degree three defines the calibration coefficient for correlating the temperature rise and corresponding axial displacement. **b** The errors of the predicted temperature are shown using the coefficients acquired during the calibration process and used for three different spatial points on the same bone samples
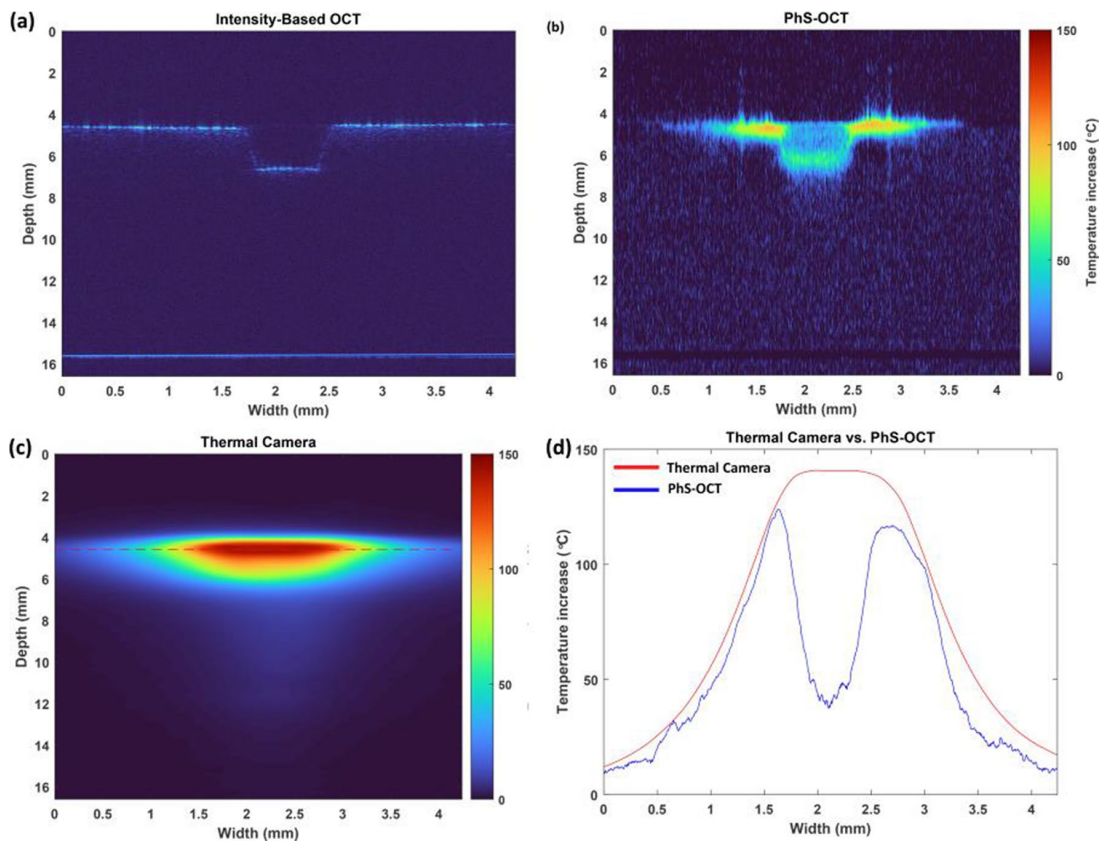
Fig. 5 Monitoring the depth and temperature rise of the bone during laser osteotomy using an Er:YAG laser (10 Hz, 230 mJ energy per pulse). **a** Intensity-based image of the crater, **b** PhS-OCT image of the cumulative temperature rise, **c** reference temperature using a thermal camera, and **d** comparison of the predicted temperature and temperature rise on the surface of the bone. The duration of the experiment was 3.7 s

and temperature differences. Following the calibration process and having acquired the required coefficient, equation (8) was used to predict the tissue temperature rise. Figure 4b shows the predicted temperature rise for three different spots on the bone tissue and the differences compared to the temperatures recorded by the thermal camera. The comparison was performed at the same distance to the crater's center as for the calibration experiment.

In addition to the single-point temperature measurements, the potential of using the coefficients acquired during the calibration process to predict tissue temperature rise in the B-scan OCT images (Fig. 5) is investigated. To investigate the two-dimensional temperature map, a thermal camera continuously monitored the bone's temperature. Figure 5a corresponds to the intensity-based OCT image, which shows the depth and shape of the laser-induced cut in real time. Figures 5b and c demonstrate the predicted temperature map using PhS-OCT, and the reference temperature map using the thermal camera, respectively. Figure 5d compares the predicted temperatures and reference temperatures on the surface of the bone.

Discussion

Although laser osteotomy offers several advantages over conventional methods for bone surgery, induced thermal damage is a major challenge that limits its application in clinical settings. In this study, the potential of a PhS-OCT system to provide feedback for controlling irrigation and real-time feedback for monitoring the depth of the laser-induced crater (provided by a conventional OCT system) is demonstrated. Figure 3 illustrates the photothermal expansion of the bone during laser osteotomy, which underlies the proposed PhS-OCT method for determining tissue temperature rise. Here, in addition to tissue expansion, changes in the attenuation coefficients of the bone due to temperature increase are also visible. The latter of which can also be used to determine the temperature rise of the tissue [52]. The PhS-OCT calibration step is characterized by simultaneously monitoring the temperature rise of the tissue (using a thermal camera) and its photothermal expansion (using an OCT system) and defining the correlation between them using equation (8). Figure 4a shows the process of extracting the coefficient by fitting the recorded temperature difference and axial displacement of the bone using equation (8). An adjusted R-square of 0.9963 using a polynomial of degree three demonstrates that the fitted parameter can predict the temperature rise of the tissue. An initial decrease in the cumulative phase was followed by an increase in the bone's temperature, due to the decrease in the refractive index of the water and the expansion of the bone's structure demonstrated in Fig. 4a [53]. During the experiments, it was

noticed that this decreasing tendency varied among different bone samples. Fresh bone, for example, had the greatest decrease in the phase, while dried bone did not show any initial decrease but followed an increasing trend from the first laser pulse. Extracting the attenuation map of the tissue from OCT images could potentially prevent this issue by monitoring and classifying the status of bone samples (hydrated, dehydrated, and carbonized). The preliminary results demonstrated the potential of utilizing attenuation map to classify the status of bone, however, identifying the reasons for variation in attenuation profile can be challenging since it could arise from the refractive index change of the tissue or the reduced water content due to high temperatures. It is worth noting that dependency of the refractive index on temperature limits this comparison in the ablation regime. This requires further investigation to calculate the refractive index of bone as a function of temperature.

The acquired calibration coefficients were used to predict the temperature rise of three different laser-induced cuts at the same distance to the center of the crater as the calibration experiment (Fig. 4b). The average value of root-mean-square error for the three experiments was estimated as 3.9°C. The main error has been observed at the beginning of the laser ablation process, which attenuation map can assist in reducing this error by classification of the state of the bone. Moreover, the generation and accumulation of debris around the incision are considered contributing parameters affecting the precision of temperature prediction. The interaction between debris and subsequent laser pulses introduces variations in phase comparison on the bone's surface. Utilization of high-pressure air can potentially reduce this error. Additionally, the proposed calibration approach currently focuses on evaluating the temperature of a single pixel, However, extending this calibration to encompass all the pixels on the surface could not only enhance accuracy but also enable the determination of the relationship between tissue-specific parameters and the temperature profile (spans from the crater's edge to more distant spatial point). The primary objective is to utilize it as a feedback system for the irrigation process during laser osteotomy. This can be achieved by defining a desired threshold and considering the error.

Finally, further investigation was conducted to determine the two-dimensional temperature rise of bone using the calibration coefficients acquired at a single point (Fig. 5). A cross-sectional intensity-based OCT image of the laser-induced crater is presented in Fig. 5a, where both the depth and shape of the cut are visible. The calculated temperature rise of the bone in this experiment is given in Fig. 5b, and the reference temperature recorded by the thermal camera for comparison can be seen in Fig. 5c. The image acquired by the reference indicates that the highest temperature rise occurred inside the laser-induced cut, where the tissue had been removed. In contrast, due to the working principle of the PhS-OCT, the highest temperature

rise is detected at the borders of the crater. This unique feature, the ability to detect temperature where tissue exists, could potentially enhance ablation efficiency compared to utilizing a thermal camera for controlling an irrigation system [54]. The structure of the cut is not visible in the infrared camera image, making it challenging to find a suitable reference point on the surface. However, the PhS-OCT system can visualize the cumulative temperature rise of the bone during laser-induced ablation and preserve the crater's shape. The phase noise and limited image range of OCT inside the tissue cause incorrect temperature detection. These errors can be minimized by selecting the region of interest in the PhS-OCT images based on the level of the signal in the intensity-based images of the OCT. Moreover, this process can also improve the calculation time required to produce PhS-OCT images. Figure 5d compares the temperature profiles on the bone's surface, which implies the difference between the detected temperature rise inside the cut in PhS-OCT method and thermal camera. Since the principle of the PhS-OCT is to follow the cumulative temperature changes over time, the removal of tissue inside the cut results in the PhS-OCT showing the last temperature reading at that point when the tissue was present.

The proposed method has the potential for use as a feedback mechanism by which to trigger pulsed irrigation during laser surgery (instead of continuous irrigation). Furthermore, calibrated PhS-OCT has the unique advantage of predicting the temperature rise of the tissue during laser ablation without prior knowledge of the opto-mechanical and thermo-optic properties of the target tissue, which are usually difficult to obtain. This method could be used in endoscopic applications and minimally invasive surgery, where a thermal camera would not be suitable. Although the PhS-OCT shows several unique advantages, it also has some limitations. To ensure the same configuration of the temperature distribution for Hs1 and Hs2, the distance between the bone and the focusing lens of the Er:YAG laser should be kept constant. Likewise, since this method uses induced cumulative phase changes, a proper unwrapping method is required to maintain the accuracy of this method. When transitioning from ex vivo to in vivo experiments, it is crucial to consider various parameters, including the presence of blood during surgery, the existence of other instruments in the surgical room, and the patient's movements. These factors have the potential to introduce noise into the phase measurements. To address this, the implementation of a real-time tracking and calibration algorithm is proposed. For instance, repositioning and real-time calibration can be performed by implementation of an external point temperature measurement (such as a miniaturized infrared camera). This continuous monitoring and adjustment of the acquired calibration parameters could potentially serve to enhance precision and maintain accuracy. In addition, the suggested

improvement ensures the safety of laser surgery which is desired for medical applications.

Conclusion

Lasers have brought many advantages to the medical field of osteotomy; however, they are not without drawbacks. During laser osteotomy using Er:YAG lasers, thermal damage is usually prevented by applying a continuous irrigation system, which, consequently, may lead to water accumulation reducing the ablation efficiency. The experimental results demonstrate the potential for utilizing the calibrated phase-sensitive OCT system as a temperature feedback mechanism, with an average root-mean-square error of 3.9°C. The introduced method is based on acquiring the tissue-specific parameters during calibration step by correlation of the measured temperature (acquired by thermal camera) and photo-thermal expansion (using phase-sensitive OCT). This feedback, combined with real-time visualization of the depth of cut using intensity-based OCT images (as shown in Fig. 5), offers a comprehensive solution to mitigate thermal damage and monitor the depth of laser-induced cut during laser osteotomy procedures.

Improving the accuracy of temperature prediction by integration of an online calibration algorithm is among our main interests for the future. Furthermore, despite the fact that OCT can provide three-dimensional images of the tissue, limited comparison means preventing further investigation of the temperature map which needs to be addressed. Independence of the phase-calibration method offers additional benefits such as acquiring the linear thermal expansion coefficient/refractive index of the tissue as a function of temperature.

Data Availability Data underlying the results presented in this paper are not publicly available at this time but may be obtained from the authors upon request.

Declarations

Ethics approval The specimens used in this experiment were available as food-based material, therefore no ethical committee approval was required.

Conflict of interest The authors declare no competing interests.

Open Access This article is licensed under a Creative Commons Attribution 4.0 International License, which permits use, sharing, adaptation, distribution and reproduction in any medium or format, as long as you give appropriate credit to the original author(s) and the source, provide a link to the Creative Commons licence, and indicate if changes were made. The images or other third party material in this article are included in the article's Creative Commons licence, unless indicated otherwise in a credit line to the material. If material is not included in the article's Creative Commons licence and your intended use is not permitted by statutory regulation or exceeds the permitted use, you will need to obtain permission directly from the copyright holder. To view a copy of this licence, visit http://creativecommons.org/licenses/by/4.0/.

References

1. Pantawane M, Dahotre N (2019) Challenges and advances in osteotomy. Ann Bone Joint Surg 2(1):1007
2. Eyrich GK (2005) Laser-osteotomy induced changes in bone. Med Laser Appl 20(1):25–36
3. Stübinger S (2010) Advances in bone surgery: the Er: YAG laser in oral surgery and implant dentistry. Clin Cosmet Investig Dent 2:47
4. Jowett N, Wöllmer W, Reimer R, Zustin J, Schumacher U, Wiseman PW et al (2014) Bone ablation without thermal or acoustic mechanical injury via a novel picosecond infrared laser (PIRL). Otolaryngol–Head Neck Surg 150(3):385–393
5. Gertzbein S, Dedemeter D, Cruickshank B, Kapasouri A (1981) The effect of laser osteotomy on bone healing. Lasers Surgery Med 1(4):361–373
6. Ohsugi Y, Aoki A, Mizutani K, Katagiri S, Komaki M, Noda M et al (2019) Evaluation of bone healing following Er: YAG laser ablation in rat calvaria compared with bur drilling. J Biophotonics 12(3):e201800245
7. Nelson JS, Orenstein A, Liaw LHL, Berns MW (1989) Mid-infrared erbium: YAG laser ablation of bone: the effect of laser osteotomy on bone healing. Lasers Surg Med 9(4):362–374
8. Panduric DG, Juric IB, Music S, Molčanov K, Sušic M, Anic I (2014) Morphological and ultrastructural comparative analysis of bone tissue after Er: YAG laser and surgical drill osteotomy. Photomed Laser Surg 32(7):401
9. Forrer M, Frenz M, Romano V, Altermatt H, Weber H, Silenok A et al (1993) Bone-ablation mechanism using CO 2 lasers of different pulse duration and wavelength. Appl Phys B 56:104–112
10. Peavy GM, Reinisch L, Payne JT, Venugopalan V (1999) Comparison of cortical bone ablations by using infrared laser wavelengths 2.9 to 9.2 μm. Lasers Surgd Med: Official J Am Soc Laser Med Surg 25(5):421–434
11. Fried D, Zuerlein MJ, Le CQ, Featherstone JD (2002) Thermal and chemical modification of dentin by 9–11-μm CO2 laser pulses of 5–100-μs duration. Lasers Surg Med: Official Je Am Soc Laser Med Surg 31(4):275–282
12. Adler DC, Huang S-W, Huber R, Fujimoto JG (2008) Photothermal detection of gold nanoparticles using phase-sensitive optical coherence tomography. Opt Express 16(7):4376–4393
13. Rajitha Gunaratne G, Khan R, Fick D, Robertson B, Dahotre N, Ironside C (2017) A review of the physiological and histological effects of laser osteotomy. J Med Eng Technol 41(1):1–12
14. Walsh JT Jr, Deutsch TF (1989) Er: YAG laser ablation of tissue: measurement of ablation rates. Lasers Surg Med 9(4):327–337
15. Bernal LMB, Shayeganrad G, Kosa G, Zelechowski M, Rauter G, Friederich N et al (2018) Performance of Er: YAG laser ablation of hard bone under different irrigation water cooling
16. conditions. SPIE, Optical Interactions with Tissue and Cells XXIX, pp 43–49
17. Niemz MH (2007) Laser-tissue interactions. Springer
18. Hibst R, Keller U (1996) Effects of water spray and repetition rate on the temperature elevation during Er: YAG laser ablation of dentine. Medical Applications of Lasers III: SPIE, pp 139–144
19. Mir M, Meister J, Franzen R, Sabounchi SS, Lampert F, Gutknecht N (2008) Influence of water-layer thickness on Er: YAG laser ablation of enamel of bovine anterior teeth. Lasers Med Sci 23:451–457
20. Hall TA, Cegla F, van Arkel RJ (2021) Simple smart implants: simultaneous monitoring of loosening and temperature in orthopaedics with an embedded ultrasound transducer. IEEE Trans Biomed Circuits Syst 15(1):102–110
21. Korganbayev S, Orrico A, Bianchi L, De Landro M, Wolf A, Dostovalov A et al (2020) Closed-loop temperature control based on fiber Bragg grating sensors for laser ablation of hepatic tissue. Sensors 20(22):6496
22. Stauffer P, Craciunescu OI, Maccarini P, Wyatt C, Arunachalam K, Arabe O et al (2009) Clinical utility of magnetic resonance thermal imaging (MRTI) for real-time guidance of deep hyperthermia. Energy-based Treatment of Tissue and Assessment V: SPIE, pp 177–188
23. Xiang L, Wang B, Ji L, Jiang H (2013) 4-D photoacoustic tomography. Sci Rep 3(1):1–8
24. Pramanik M, Erpelding TN, Jankovic L, Wang LV (2010) Tissue temperature monitoring using thermoacoustic and photoacoustic techniques. In: Photons Plus ultrasound: imaging and sensing 2010. SPIE, pp 439–448
25. Landa FJO, Deán-Ben XL, Sroka R, Razansky D (2017) Volumetric optoacoustic temperature mapping in photothermal therapy. Sci Rep 7(1):1–8
26. Oraevsky AA, Esenaliev RO, Motamedi M, Karabutov AA (2001) Real-time optoacoustic monitoring of changes in tissue properties. Google Patents
27. Huang D, Swanson EA, Lin CP, Schuman JS, Stinson WG, Chang W et al (1991) Optical coherence tomography. Science 254(5035):1178–1181
28. Fercher AF, Drexler W, Hitzenberger CK, Lasser T (2003) Optical coherence tomography-principles and applications. Rep Progr Phys 66(2):239
29. Beaudette K, Baac HW, Madore W-J, Villiger M, Godbout N, Bouma BE et al (2015) Laser tissue coagulation and concurrent optical coherence tomography through a double-clad fiber coupler. Biomed Opt Express 6(4):1293–1303
30. Hamidi A, Bayhaqi YA, Canbaz F, Navarini AA, Cattin PC, Zam A (2021) Long-range optical coherence tomography with extended depth-of-focus: A visual feedback system for smart laser osteotomy. Biomed Opt Express 12(4):2118–2133
31. Oh W-Y, Yun S, Vakoc B, Tearney G, Bouma B (2006) Ultra-high-speed optical frequency domain imaging and application to laser ablation monitoring. Appl Phys Lett 88(10):103902
32. Adler DC, Huber R, Fujimoto JG (2007) Phase-sensitive optical coherence tomography at up to 370,000 lines per second using buffered Fourier domain mode-locked lasers. Opt Lett 32(6):626–628
33. Manapuram RK, Manne VGR, Larin KV (2009) Phase-sensitive swept source optical coherence tomography for imaging and quantifying of microbubbles in clear and scattering media. J Appl Phys 105(10):102040
34. Hamidi A, Bayhaqi YA, Canbaz F, Navarini A, Cattin PC, Zam A (2020) Imaging photothermal-induced expansion of bone during laser osteotomy by phase-sensitive OCT: preliminary results. In: Biomedical Spectroscopy, Microscopy, and Imaging. SPIE, pp 127–133
35. Müller HH, Ptaszynski L, Schlott K, Debbeler C, Bever M, Koinzer S et al (2012) Imaging thermal expansion and retinal

tissue changes during photocoagulation by high speed OCT. Biomed Opt Express 3(5):1025–1046

35. Kim J, Oh J, Milner TE (2006) Measurement of optical path length change following pulsed laser irradiation using differential phase optical coherence tomography. J Biomed Opt 11(4):041122

36. Hamidi A, Bayhaqi YA, Canbaz F, Navarini AA, Cattin PC, Zam A (2021) Observation of controlled temperature changes of bone by phase-sensitive optical coherence tomography. Eurn Conf Biomed Opt: Opt Soc Am:ETu2A. 38

37. Amewoui F, Le Coz G, Bonnet AS, Moufki A (2019) Bone drilling: a thermal model for bone temperature prediction. Comput Methods Biomech Biomed Eng 22(sup1):S305–S3S7

38. Beltran Bernal LM (2021) Laser and wave-guides system for endoscopic/fiberscopic laser surgery. University_of_Basel

39. Perhavec T, Diaci J (2009) Comparison of heat deposition of Er: YAG and Er, Cr: YSGG lasers in hard dental tissues. J Laser Health Acad 2:1–6

40. Aoki A, Mizutani K, Taniguchi Y, Komaki M, Ejiri K, Mikami R et al (2017) Periodontal pocket therapy using Er: YAG laser: systematic review of literature and introduction of a new treatment procedure. Nippon Laser Igakkaishi 38(2):167–178

41. Akhbar MFA, Yusoff AR (2019) Comparison of bone temperature elevation in drilling of human, bovine and porcine bone. Proc CIRP 82:411–414

42. Lukac M, Perhavec T, Nemes K, Ahcan U (2010) Ablation and thermal depths in VSP Er: YAG laser skin resurfacing. J Laser Health Acad 1(1):56–71

43. Timmins P, Wall J (1977) Bone water. Calcif Tissue Res 23(1):1–5

44. Behari J, Guha S, Agarwal P (1977) Absorption spectra of bone. Calcif Tissue Res 23:113–114

45. Genina EA, Bashkatov AN, Tuchin VV (2008) Optical clearing of cranial bone. Adv Opt Technol 2008

46. Wong BJ-F, Sung V, Berns MW, Svaasand LO, Neev J (1995) Holmium-YAG laser ablation characteristics in calvarial lamellar and cortical bone: The role of water and tissue micro-architecture. Lasers Med Sci 10:181–188

47. Park KS, Park E, Lee H, Lee H-J, Lee S-W, Eom TJ (2021) Phase stable swept-source optical coherence tomography with active mode-locking laser for contrast enhancements of retinal angiography. Sci Rep 11(1):16636

48. Moon S, Chen Z (2018) Phase-stability optimization of swept-source optical coherence tomography. Biomed Opt Express 9(11):5280–5295

49. Song S, Wei W, Hsieh B-Y, Pelivanov I, Shen TT, O'Donnell M et al (2016) Strategies to improve phase-stability of ultrafast swept source optical coherence tomography for single shot imaging of transient mechanical waves at 16 kHz frame rate. Appl Phys Lett 108(19)

50. Miyazaki H, Ushiroda I, Itomura D, Hirashita T, Adachi N, Ota T (2009) Thermal expansion of hydroxyapatite between− 100° C and 50° C. Mater Sci Eng: C 29(4):1463–1466

51. Albagli D, Dark M, von Rosenberg C, Perelman L, Itzkan I, Feld MS (1994) Laser-induced thermoelastic deformation: a three-dimensional solution and its application to the ablation of biological tissue. Med Phys 21(8):1323–1331

52. Su Y, Yao XS, Li Z, Meng Z, Liu T, Wang L (2015) Measurements of the thermal coefficient of optical attenuation at different depth regions of in vivo human skins using optical coherence tomography: a pilot study. Biomed Opt Express 6(2):500–513

53. Goetz G, Ling T, Gupta T, Kang S, Wang J, Gregory PD et al (2018) Interferometric mapping of material properties using thermal perturbation. Proc Natl Acad Sci 115(11):E2499–EE508

54. Bernal LMB, Canbaz F, Droneau A, Friederich NF, Cattin PC, Zam A (2020) Optimizing deep bone ablation by means of a microsecond Er: YAG laser and a novel water microjet irrigation system. Biomed Opt Express 11(12):7253–7272

Miniaturized OCT-assisted Laser Ablation for Minimally Invasive Laser Osteotomy

This chapter presents the miniaturized version of the OCT system integrated with an Er:YAG laser. Coupling high-power lasers into fiber has always been a challenge. In this publication, we coupled an Er:YAG laser into a sapphire fiber with high efficiency. We integrated a miniaturized OCT system with it to monitor and control ablation depth. Using the miniaturized integrated setup, we could achieve the controlled depth of ablation up to 5 mm in a cow femur-bone tissue.

Towards miniaturized OCT-guided laser osteotomy: integration of fiber-coupled Er:YAG laser with OCT

ARSHAM HAMIDI,[1,6] (iD) **YAKUB A. BAYHAQI,**[1] (iD)
ALEXANDER A. NAVARINI,[2] **PHILIPPE C. CATTIN,**[3] (iD)
AZHAR ZAM,[1,4,5,7] (iD) **AND FERDA CANBAZ**[1,8] (iD)

[1]*Biomedical Laser and Optics Group (BLOG), Department of Biomedical Engineering, University of Basel, CH-4123 Allschwil, Switzerland*
[2]*Digital Dermatology, Department of Biomedical Engineering, University of Basel, CH-4123 Allschwil, Switzerland*
[3]*Center for Medical Image Analysis and Navigation (CIAN), Department of Biomedical Engineering, University of Basel, CH-4123 Allschwil, Switzerland*
[4]*Division of Engineering, New York University Abu Dhabi, Abu Dhabi 129188, United Arab Emirates*
[5]*Tandon School of Engineering, New York University, Brooklyn, NY 11201, USA*
[6]*arsham.hamidi@unibas.ch*
[7]*azhar.zam@nyu.edu*
[8]*ferda.canbaz@unibas.ch*

Abstract: Optical coherence tomography (OCT) combined with an ablative Er:YAG laser has been recognized as a promising technique for real-time monitoring and controlling the depth of laser-induced cuts during laser osteotomy procedures. In this study, a miniaturized OCT-assisted Er:YAG laser system was developed for controlled laser ablation of bone tissue. The developed system involved coupling a high-power Er:YAG laser into a sapphire fiber with a core diameter of 425 μm and miniaturizing the sample arm of a long-range swept-source OCT system. Controlled laser osteotomy experiments were performed to evaluate the performance of the miniaturized setup. Real-time depth monitoring and control were achieved through an optical shutter controlled by the OCT system. The experimental results showed controlled ablation with a mean accuracy of 0.028 mm when targeting depths of 1 mm, 3 mm, and 5 mm on cow femur bones. These results demonstrate the potential of the developed miniaturized OCT-assisted Er:YAG laser system for use in robotic-assisted minimally-invasive laser osteotomy.

1. Introduction

In recent years, several studies have demonstrated the advantages of using lasers in the medical field of bone-cutting (osteotomy). Laser technology offers distinct advantages by enabling precise, sterile, and functional cuts to be performed remotely with a clear field-of-view, while preserving the porous structure of bone, promoting accelerated healing [1–5]. The contactless nature of laser osteotomy has the added benefit of incurring fewer mechanical effects in comparison to traditional bone surgery methods [6–9]. Photo-thermal ablation using mid-infrared wavelengths has shown promising results in laser osteotomy [7,10]. Bone tissue primarily consists of approximately 13 % water, 27 % collagen, and 60 % hydroxyapatite [11,12]. The Er:YAG laser (2.9 μm), with its high absorption peak in water molecules present in bone tissue, is an ideal choice for laser osteotomy [1]. Upon laser heating, the water molecules in the bone tissue rapidly evaporate, resulting in micro-explosions and subsequent removal of the bone tissue [13,14]. This ablation mechanism, commonly referred to as cold ablation in literature, offers high ablation efficiency while minimizing thermal damage [15].

Despite the added benefits of employing lasers in the medical field of osteotomy, it is crucial to note that the accuracy of lasers is contingent upon their level of control. Employing a real-time visualization and depth monitoring system during laser osteotomy can improve the accuracy of laser surgery, especially in minimally invasive procedures. For this reason, feedback systems are essential for providing surgeons with the information required during laser surgery [16]. To date, several methods for real-time monitoring and feedback have been introduced. To ensure that the laser-induced cut follows a pre-defined depth of cut, for example, monitoring techniques include photoacoustic tomography, linnik interferometers using a femtosecond laser, self-mixing interferometers, and cameras with high magnification optics [17–22]. There are some drawbacks associated with each of these techniques, such as angled views of the ablation cut, invasive detection, limited resolution, and limited application in miniaturized configurations. One technique that may overcome these drawbacks is optical coherence tomography (OCT), a non-invasive, high-resolution, and high-speed interferometric imaging modality with a wide range of applications in the medical field [23]. The first study to use an OCT system to monitor laser ablation successfully demonstrated its potential as a monitoring system [24]. Since then, several researchers have confirmed the potential of OCT as a real-time visual feedback tool during laser surgery [20,25,26].

With the advancement of OCT-assisted laser osteotomy in free-space, the next step is to develop a miniaturized integrated setup for use in minimally-invasive laser osteotomy [27]. Jivraj et al. demonstrated that a pulsed CO_2 (1064 nm) laser coaxially integrated with an OCT system using double-clad fiber could monitor a laser-induced cut up to 0.5 mm in cortical bone of porcine scapula specimens [25]. Bernal et al. have shown that a fiber-coupled Er:YAG laser (germanium oxide fiber) with a forward-cutting configuration can achieve a cutting depth of 6.82 ± 0.99 mm in sheep bone [28]. Despite the promising outcomes of utilizing a germanium oxide fiber to deliver Er:YAG laser into an endoscope for laser osteotomy, certain limitations such as the high temperature of the fiber's tip (approximately 70 °C) and its limited working distance hindered its integration with a feedback system.

The present study builds upon our previous research, which focused on the integration of OCT and Er:YAG lasers in free space, where the challenges of this integrated system are investigated [5,10,20]. This study introduces a novel approach by integrating a miniaturized fiber-based Er:YAG laser, employing a sapphire fiber, with a long-range swept-source OCT (SS-OCT) system to enable real-time depth feedback during laser osteotomy. By optimizing the coupling mechanism, a high coupling efficiency of 75.7 % with a stable fiber's tip temperature of ~ 31 °C at an input energy of 990 mJ is achieved. The combined systems were successfully incorporated into a compact probe with the dimensions of 13 mm × 42.1 mm x 10.13 mm for side ablation. In addition, a depth-controlled system is developed which could stop the ablative procedure by reaching the desired depth of laser-induced cut.

2. Methods

2.1. Miniaturized integrated setup

Figure 1 presents the schematic of the integrated setup designed for controlled bone ablation. A programmable akinetic swept-source laser (SLE-101, Insight Photonic Solution, Inc., Lafayette, CO, USA) was utilized, featuring a central wavelength of 1289 nm, a bandwidth of 62 nm, and an A-scan rate of 104.17 kHz. For the ablation process, an Er:YAG laser (R4X100C2-ER, MegaWatt lasers, USA,) producing 350 µs-long pulses was employed. In Fig. 1(a), the OCT laser is directed to the reference arm (10 %) and sample arm (90 %) using a fiber optic coupler (TW1300R2A1, Thorlabs). Then, OCT laser is delivered to the reference and sample arms using an optical circulator (CIR1310-APC, Thorlabs). The reference and sample arm outputs are connected to pigtailed ferrules (SMPF0115-FC, Thorlabs) and collimated using a grin lens with 0.23 pitch (GRIN2313A, Thorlabs). In the reference arm, the collimated beam is focused on the

reference mirror (M1, PF10-03-M01, Thorlabs) using an achromatic doublet (L1, f = 30 mm, AC127-030-C, Thorlabs). The reflected/scattered light coupled back to the fiber is sent to a balanced detector (PDB480C-AC, Thorlabs) using a 50/50 fiber coupler. With this configuration, the OCT system has an imaging range of 2.25 cm in the air, with an axial resolution of 11 μm. During laser ablation of the bone, depth information is recorded using M-mode data over the time of laser ablation.
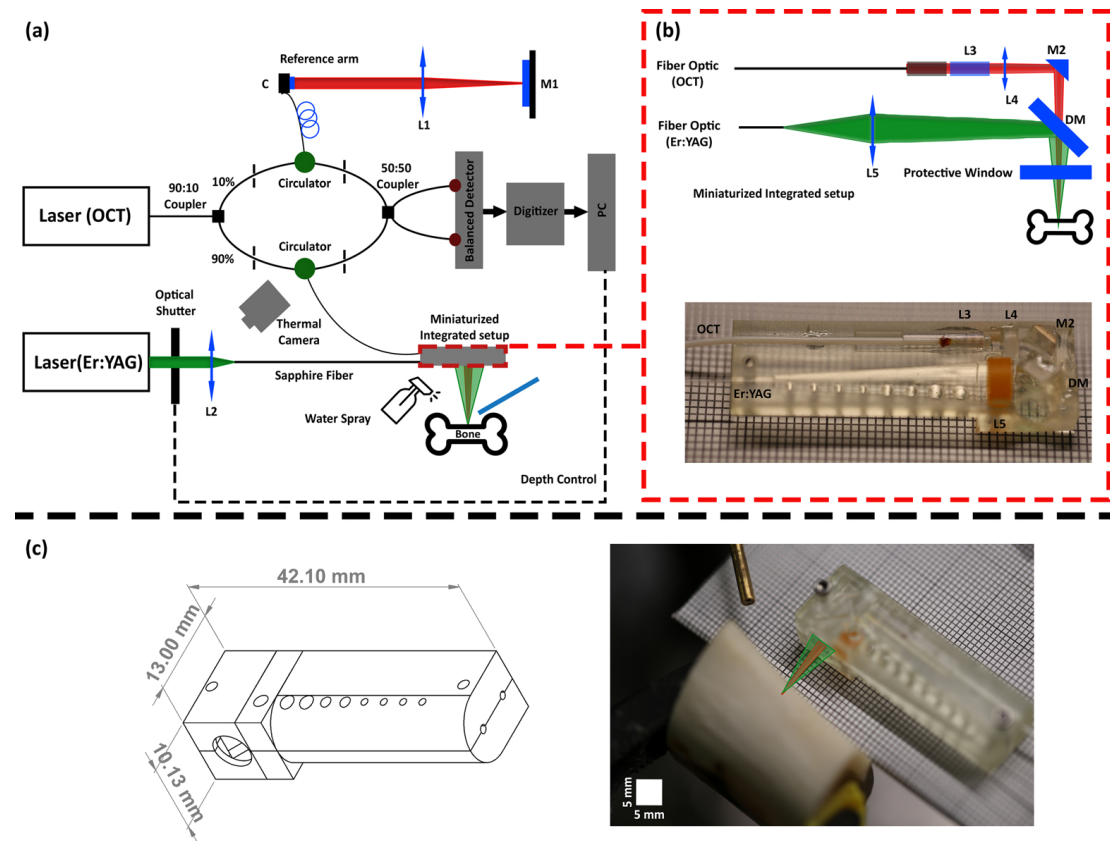
Fig. 1. (a) Schematic of the integrated setup, (b) schematic diagram of the integrated Er:YAG laser in the sample arm of the OCT system, (c) 3D-printed housing of the integrated setup.

In Fig. 1(a), the output of the Er:YAG laser was controlled by an optical shutter (SH1/M, Thorlabs) that received commands from the OCT system. The optical shutter has a 15 ms response time based on the information provided by the manufacturing company. Fiber coupling of Er:YAG laser was performed by a CaF_2 lens (L2, f=50 mm, LA5763, Thorlabs). The sapphire fiber (Photran, USA) had a core diameter of 425 μm, with a numerical aperture (NA) of 0.12. Sapphire fibers serve the purpose of maintaining low tip temperature and minimizing beam divergence. However, a major drawback of using sapphire fibers is their cost because drawing sapphire fibers is challenging due to their high melting temperatures, leading to the production of costly pieces that typically offer limited length options. During the fiber coupling process, a thermal camera (FLIR A655sc, accuracy = ± 2 °C) was used to monitor the temperature rise at the tip of the fiber. We used a sapphire fiber in these experiments because of the low temperature of the fiber tip and the small NA of the fiber [29]. The length of the sapphire fiber was ∼ 1 m. During the bone ablation experiments, the repetition frequency and the output energy of fiber were set to 5 Hz and 1 J/pulse, respectively.

Figure 1(b), shows an enlarged version of the integrated Er:YAG laser in the sample arm of the OCT system. It is worth noting that the required size of the optics was not readily available off the shelf. As a result, the optical elements underwent manual grinding. The required diameter of the optical components is attained by grinding the optics, which are mounted on a milling head, using 1000 and 2000-grade sandpapers. This process is performed with respect to the calculated beam size and designed housing. The 3D-printed housing is designed with a proper grooved holder for each optics which aids the initial alignment of the system. The OCT laser was collimated using a grin lens (L3) and focused using a polished achromatic doublet (L4, $f =$ 30 mm, AC127-030-C, Thorlabs) with a diameter of 3 mm, and directed to the dichroic filter using a right-angle mirror (M2, # 65-844, Edmund Optics). The spot size is calculated as 51 µm. Fine alignment of the OCT is performed by adjusting the M2. Induced dispersion mismatched between the reference and sample arm is compensated using a standard dispersion compensator algorithm. The Er:YAG laser was focused on the sample using a polished lens (L5, $f =$ 20 mm, LA5315, Thorlabs) with a diameter of 6 mm. The distance between the laser's fiber output and the lens was 2.3 cm, and the corresponding beam diameter was measured to be 0.9 mm. The waist location was 4.9 cm away from the lens. The working distance of the current design is roughly 2.2 cm away from the sapphire window. The spot size was intentionally kept relatively large to ensure that no damage was induced on the dichroic mirror and to provide a long depth of focus. OCT and Er:YAG lasers were combined using a custom-made dichroic filter (DM, 97 % reflection at 2.94 µm, and 90 % transmission at 1289 ± 75 nm, II-VI Coherent, USA). For aligning the sapphire fiber, we utilize a fiber optic positioner (FP-1A, FPH-J, Newport) with the fiber's end-tip. This positioner is mounted on a linear translation stage (PT1/M, Thorlabs) that offers the necessary degrees of freedom for fiber alignment. We carry out this alignment process using a 532 nm laser diode coupled to the fiber through a flip mirror within the path of the Er:YAG laser in free space. Finally, A 0.5 mm thick sapphire window was used in the miniaturized setup to protect the optics from debris generated during laser osteotomy (Ultitech Xiamen, China). Figure 1 (c) shows a photo of the 3D-printed housing of the integrated setup and its design.

2.2. Depth-controlled ablation

Depth-controlled ablation is performed by controlling the optical shutter with the OCT software. In free space, the depth-control software works based on the detection of the depth in the middle of the crater and comparing it with the reference lines (in the left and right of the ablation crater). This depth predication is enhanced by using the Kalman filter, which is based on a constant ablation rate model, and has the potential to stop the ablative laser before reaching the desired depth based on the prediction that the next pulse will ablate more than the pre-planned depth of the cut [30,31]. The reference point was set to be the surface of the bone before ablation. In addition, irrigation causes an accumulation of water inside the laser-induced cut, and the next pulse causes a water explosion which can dramatically affect the depth measurements. The detection of the water's surface as depth of cut can cause an error. We have modified the depth detection algorithm to ignore the values which show a decrease in the depth of cut compared to the last measured depth.

3. Results and discussion

3.1. Er:YAG laser: fiber coupling

Coupling a high-energy laser into a fiber has always been a challenge, which has been clearly described in our previous study [29]. When employing fibers for surgical applications via endoscopes, the coupling mechanism must be highly robust. Thus, in this study, we implemented a thermal camera and an aperture to monitor the maximum temperature at the fiber tip and adjust the energy on the fiber through the beam size on the fiber. Before increasing the energy level,

the aperture diameter was reduced to deliver approximately 50 mJ of energy into the fiber. At the next energy level, first, the tip position was optimized in the *x*, *y*, and *z* directions. Since the laser output consists of multiple longitudinal modes that may vary with different output energies and shift the focal plane, this step enhanced the repeatability of the fiber coupling process by observing the temperature increase of the fiber tip while repositioning the fiber, especially in the z-direction. The simultaneous temperature measurements helped to foresee the damage before it occurred. With the suggested method, once the fiber position was optimized, the setup required no further alignment for months. Concurrently, continuous monitoring of the tip temperature served as feedback to assess the risk of fiber damage, reinforcing the robustness of the coupling setup. For instance, tip temperature measurements around 31 °C suggested "safe positions," while temperature readings above 35 °C ended up damaging the fiber. Thus, this approach enabled the determination of the optimal position for the fiber tip, considering not only the transmitted energy but also the tip temperature. This outcome has paved the way for the development of a resilient fiber coupling system that holds the potential for future automation. Note that, diffraction can hinder the coupling efficiency with this method when the aperture blocks the beam. An alternative could be using a half-wave plate and a beam-splitter combination, however, a feedback signal may still be needed from the fiber tip to prevent any damage.

Table 1 presents the performance of the sapphire fiber at various energy levels. The sapphire fiber demonstrated an estimated maximum transmission of 80 % at the lowest input energy. The average coupling efficiency, which is closely aligned with the estimates provided by the manufacturer (Photran, USA), reached 76.5 %. The maximum input tip temperature recorded was approximately 31°C. It was observed that the fiber tip suffered damage beyond this temperature threshold, potentially attributed to the high beam intensity at the center, considering a Gaussian beam profile for the laser. Damage due to dust during the experiments usually resulted in a momentary irreversible decrease in the transmitted energy. During the fiber coupling tests, however, as soon as the applied peak fluence was above 2.1 kJ/cm^2, the fiber tip was ablated. We performed the experiments at a safe level peak fluence level of 1.76 kJ/cm^2. Figure 2 (a) depicts the experimental configuration of the fiber coupling setup, where a thermal camera placed above the fiber's tip monitored temperature changes. Figure 2(b) illustrates the maximum temperature rise experienced by the fiber's tip during the coupling procedure. As previously mentioned, the spatial filter was gradually opened after the laser initiation, resulting in an increase in tip temperature. The vertical dashed line in Figure 2(b) indicates the time when the maximum laser energy was delivered into the fiber. The graph reveals that the fiber's tip temperature fluctuated within the range of the maximum and minimum temperature values (indicated by horizontal dashed lines), confirming the stability of the temperature throughout the experiments.

Table 1. Evaluation of coupling efficiency and measured tip temperature of the sapphire fiber.

| Input energy (mJ)	Coupling efficiency (%)	Maximum measured input tip temperature (°C)
110	80	27.7
210	71.4	27.7
380	79.2	29
566	75.9	29.8
770	76.6	30.2
990	75.7	31

3.2. Depth-controlled laser osteotomy

The Er:YAG arm of the miniaturized integrated setup consisted of a focusing lens, dichroic mirror, and a sapphire window after the fiber. At the maximum input energy of 1000 mJ, the fiber was
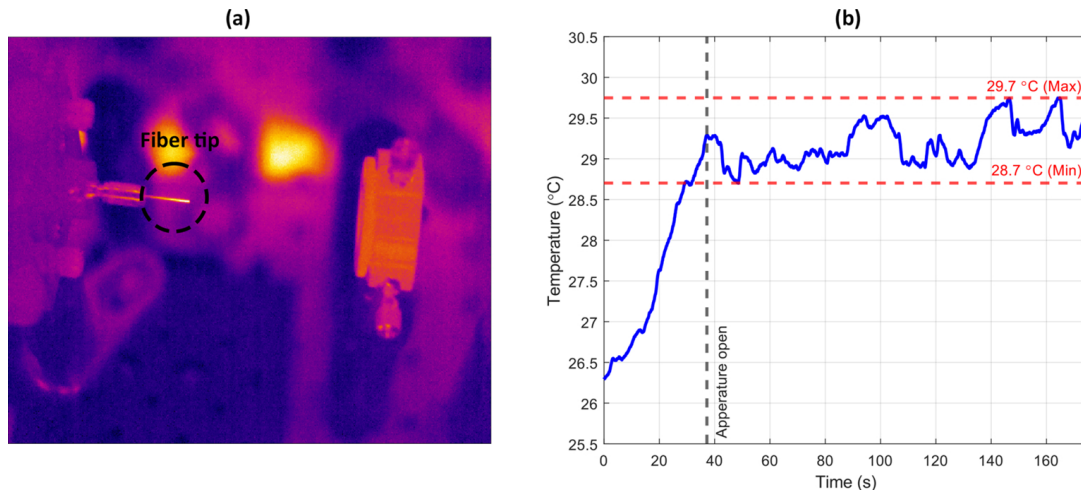
Fig. 2. Er:YAG laser fiber coupling configuration. (a) Experimental setup, and (b) the temperature of the fiber tip during the fiber coupling procedure.

able to transmit 75.7 % of the input energy. After the optics, the transmitted energy was 420 mJ corresponding to 56 % of the delivered energy and a peak fluence level of 132 J/cm^2 on the sample. Optical instruments used in the miniaturized probe for the Er:YAG laser were prepared by polishing, grinding, and cutting, possibly decreasing the surface quality and increasing the losses. We believe the overall transmission can be improved up to 65 %. Figure 3 depicts the real-time monitoring of bone tissue ablation utilizing the developed OCT system. The experimental procedure was conducted on cow femur bone tissue. The acquisition of OCT images commenced prior to the initiation of the first pulse from the Er:YAG laser and ceased upon completion of laser ablation. In Fig. 3, the process of creating a laser-induced cut with a depth of 4.35 mm is illustrated. It is important to highlight that manual irrigation was employed during laser ablation to minimize bone tissue dehydration, while pressurized air was directed towards the cut to remove accumulated water. We employed manual irrigation by monitoring reduced ablation efficiency through sound generation and OCT depth detection [5,32]. With the help of manual irrigation, no visible thermal damage was induced in the bone samples, and clean line cuts were achieved. Furthermore, given the high water absorption of the Er:YAG laser, it is crucial to eliminate accumulated water within the laser-induced cut, as this water can act as a protective barrier and diminish ablation efficiency [29]. The vertical and horizontal lines observed in Fig. 3 correspond to the water explosion within the bone and the reflection from the protective window, respectively [20].

As the next step, we created laser-induced cuts with pre-defined depths of 1 mm, 3 mm, and 5 mm. Real-time monitoring of the ablation crater using the OCT system allows us to provide this feedback and send a close command to the optical shutter when the desired pre-planned depth of the cut is reached. The depth of the cut is determined by comparing it to the bone's surface before the start of the ablation. Figure 4 shows the corresponding results of the depth-controlled ablation using the miniaturized integrated setup. Performance was evaluated by making three laser cuts on the bone tissue at the three pre-defined depths (controlled using M-mode OCT image in real-time), and measurements were taken using the same OCT system with a free-space sample arm of OCT system which is described in our previous study [20]. This sample arm is empowered using a Bessel-like beam which extends the depth of focus up to 28.7 mm. For the pre-determined 1 mm, 3 mm, and 5 mm deep cuts, the mean values were 1.0487 mm (std = ±0.0336 mm), 3.0873 mm (std =± 0.1303 mm), and 4.972 mm (std =± 0.2382 mm), respectively. The average ablation efficiency is measured as 0.338 mm^3/s in this experiment.
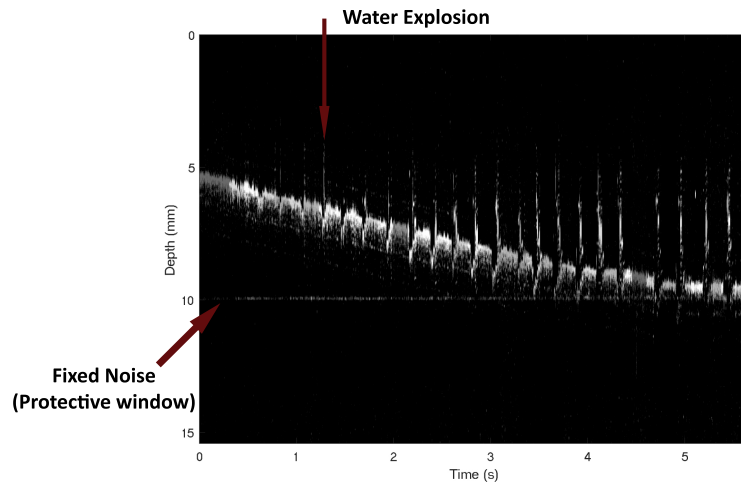
Fig. 3. Bone tissue ablation process as a function of time (M-mode). Vertical lines indicate splashes of the water accumulated in the laser-induced cut.
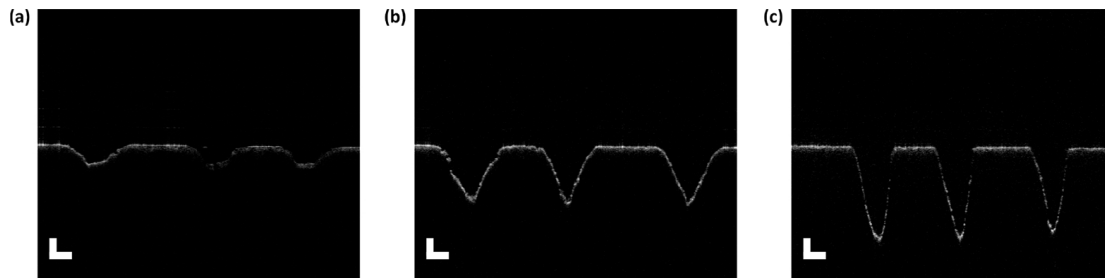
Fig. 4. Depth-controlled ablation of the bone tissue. (a), (b), and (c) present the pre-defined ablation depths of 1 mm, 3 mm, and 5 mm, respectively.

4. Conclusions

The Er:YAG laser has demonstrated great potential in laser osteotomy, offering deep ablation with minimal thermal damage to surrounding tissues. Additionally, OCT-assisted laser ablation has proven to be a reliable system, providing real-time feedback on the depth of laser-induced cuts. In this study, we miniaturized the integrated setup by coupling the Er:YAG laser into a sapphire fiber. A maximum output energy of 750 mJ was achieved when ablating bone tissue, with a fiber tip temperature of 30°C. However, the incorporation of an uncoated focusing lens, dichroic filter, and sapphire window led to a decrease in energy output to ~420 mJ. Nevertheless, we were able to achieve a 5 mm ablation depth on bone tissue using the fiber-coupled Er:YAG laser at a repetition rate of 5 Hz. The miniaturized integrated setup exhibited a promising average ablation rate of 0.338 mm^3/s, compared to previous studies involving the use of the Er:YAG laser in osteotomy [7,28,33]. As the width of the cut and the parameters related to irrigation and pressurized air play a crucial role in investigating the efficient ablation rate, further research is necessary to enhance its efficiency. We tested its performance with pre-determined ablation depths of 1 mm, 3 mm, and 5 mm. The depth-controlled ablation system errors were ±0.0336 mm, ±0.1303 mm, and ±0.02383 mm, respectively. The Er:YAG laser has demonstrated the output energy of 1.056 J±61.22 mJ measured over 169 pulses. The main error in the depth-controlled ablation arises from the lack of real-time adjustment of the energy of the Er:YAG laser. For instance, in the depth-controlled ablation monitoring using the OCT system, the energy of the last laser pulse should be modified to remove the required depth indicated by the OCT system. In

addition, relatively slow communication to the optical shutter can also contribute to the induced error.

Despite its distinct advantages, the miniaturized integrated setup does have certain limitations. Long sapphire fibers are costly and hard to produce mainly because of their high melting temperatures. However, because of their resilience to high energies, low divergence, and low tip temperature under laser illumination, they have great potential to be used in minimally invasive surgical applications of lasers. In our study, however, we used a 1-m fiber to test the integrated setup for bone ablation performance and to investigate challenges of integration, but in certain medical cases, this length could be limiting. To use sapphire fibers in clinical devices, the first step would be the extension of the length to at least 2 m. This could increase the losses and decrease the transmitted laser energy. In addition, since our primary goal is to achieve a robotically controlled minimally invasive surgical probe, we should consider placing the ablation laser and the fiber coupling setup close enough to be able to use this length. In real surgery, the miniaturized integrated system needs to be accompanied by suction and pulsed irrigation units. These additions would be necessary to avoid the blood layer on the bone surface blocking the laser ablation. Furthermore, the miniaturized probe would also require tissue-specific surgery, by incorporating miniaturized tissue detection systems.

The integration of the fiber-based Er:YAG laser with the OCT system in a compact configuration leads to increased housing temperature, which can hinder the use of scanning mechanisms (such as MEMS mirrors, micro motors, etc.) [34]. Due to the limited reflection of the dichroic mirror at 2.9 um, the leaking energy caused a temperature increase of up to 80°C (at this point the laser beam was blocked before any damage). The damage to the 3D-printed material was prevented by doing the ablation experiment in discrete steps, allowing the material to cool down. This could be easily avoided by using a custom-made beam block. Furthermore, as demonstrated in a previous study, laser ablation of bone tissue generates debris that can accumulate on the protective window during laser osteotomy [20]. Although the Er:YAG laser can clean its path on the protective window, the surrounding area remains covered with debris. Since the accumulated debris layer consists of bone particles and water splashes, the ablation laser induces ablation on the surface at the center of the beam where we expect to have higher intensity. This was the reason behind employing the M-mode scanning system to capture images through the clean path on the sapphire window. The measured errors in the depth-controlled system indicate that the errors tend to increase with the depth of the laser-induced cut. These errors primarily arise due to the accumulation of water inside the laser-induced cut, which cannot be effectively removed by pressurized air. Consequently, depending on the volume of water accumulated inside the cut, either the surface of the cut or an incorrect depth of the cut (due to the refractive index of water) may be detected.

The miniaturized system has exhibited promising performance in creating laser-induced cuts on bone tissue. However, to facilitate its application in robot-assisted laser osteotomy, several enhancements are necessary. First, the designed 3D-printed housing lacked the degree of freedom required for aligning the mirror and dichroic filter. This can be achieved by designing a holder that can be adjusted with a screw. The implementation of a top-hat beam shaper holds the potential to improve the maximum energy coupled to the fiber. Furthermore, further exploration of the scanning methodology for both the OCT system and Er:YAG laser is warranted. This would enable the acquisition of two-dimensional OCT images and line cuts. Employing scanning for the Er:YAG laser can also offer the advantage of cleaning the protective window, thereby enhancing the quality of OCT images. By optimizing the system developed in this study, there is a promising outlook for its utilization in minimally invasive robot-assisted laser osteotomy. We foresee that with the advancement of high-energy custom-made optics and miniaturized holders, the size of the integrated system can be further reduced.

CHAPTER 6

Discussion and conclusion

6.1 Discussion

The main objective of this doctoral thesis was to develop a reliable and accurate visual feedback system for surgeons during laser osteotomy using an OCT modality. The developed system had to provide real-time images of structural and dynamic changes in bone tissue during laser osteotomy. Furthermore, the integrated system (Er:YAG laser and OCT) had to have the potential for miniaturization to fulfill the aim of the MIRACLE project for minimally invasive laser osteotomy. The following research was therefore carried out in the framework of this thesis project.

Chapter 3: As a first step, we developed a long-range OCT system (26.2 mm imaging range in air) integrated with an Er:YAG laser to be able to monitor deep laser ablations of bone. To achieve optimal image quality within the imaging range, we designed and implemented a Bessel-like beam OCT system to achieve an extended DOF of 28.7 mm. In addition to an extended DOF, the self-healing properties of the BLB could reduce imaging artifacts during laser osteotomy, such as debris and water droplets. An experimental comparison of the Gaussian beam and the BLB demonstrated the significant advantages of the BLB in the presence of imaging artifacts. The results of this study demonstrate the potential of the developed integrated system to monitor the ablation of bone in real-time.

Chapter 4: Temperature rise in bone during conventional and laser osteotomy can lead to irreversible damage to critical surrounding tissue. Monitoring and controlling temperature rise in bone tissue is therefore crucial to achieving safe laser osteotomy. We experimentally demonstrated that a calibrated phase-sensitive OCT system could be used to monitor temperature rise in tissue in real-time. The preliminary results show that tissue-specific optomechanical and thermo-optical properties can be acquired to estimate the temperature rise in bone during laser ablation.

Chapter 5: Safe and accurate laser osteotomy additionally requires feedback from a tissue sensor. A tissue sensor can detect the type of tissue before laser ablation and perform tissue-specific laser ablation. To do this, we integrated tissue differentiation using the LIBS method with the BLB-OCT and Er:YAG laser. The optical design aimed for a coaxial combination of the Er:YAG laser, the OCT system, and the Nd:YAG laser to improve the safety and accuracy of laser osteotomy. The experimental results demonstrated that the developed system generated a map of the tissue surface and detected the type of tissue before firing the ablation laser as the cut proceeded into the depth of the tissue.

Chapter 6: For minimally invasive endoscopic applications, the integrated setup (OCT and Er:YAG laser) was miniaturized. As a first step, we optimized the coupling efficiency of the Er:YAG laser into a sapphire fiber. The ablation procedure was monitored and controlled using an integrated OCT system with a fiber-based Er:YAG laser. The first miniaturized prototype demonstrates the possibility of cutting femur bone tissue up to 5 mm in a controlled way.

6.2   Future work

Several approaches can be pursued in the future toward achieving real-time and accurate visual feedback during laser osteotomy. Regarding the accuracy of depth-controlled laser surgery, improving the properties of Er:YAG lasers could improve the results. The ablation rate of the Er:YAG laser in bone tissue does not follow a constant value and highly depends on the optics and properties of the tissue. This fact suggests that an extra degree of freedom to control the energy per pulse during laser ablation could improve preplanned laser ablations. Furthermore, a laser cut induced by a Gaussian-intensity laser beam follows a conical geometry. The cone-shaped profile of the cut could reduce the contrast between the OCT image and the collection of plasma light on the tissue sensor at the bottom of the laser-induced cut. Therefore, using a top-hat intensity Er:YAG laser could improve the accuracy of the feedback of both OCT and LIBS systems.

Accumulated debris and water droplets on the protective window are significant issues for the feedback system during laser osteotomy. Although solutions like using continuous air pressure to clean the window, mechanical cleaning methods, and taking advantage of the self-healing properties of the Bessel beam could reduce this issue, in long-lasting ablations to reach deep levels, alternative solutions are sought. For instance, we have noticed that during laser osteotomy the Er:YAG laser could clean its spot size on the window by ablating the accumulated debris. Developing a custom-made double-clad fiber to deliver the OCT and Er:YAG laser into the endoscope could therefore solve this issue. Another approach could consist in overlapping the Er:YAG laser with the OCT scanning rather than moving the bone tissue or displacing the ablation unit by a robotic arm. This would provide a clear field of view for the OCT system. For instance, a fixed housing and two separate proximal scanning systems could be utilized for OCT (B-scan) and

the integrated unit could be used to clean the protective window based on the OCT's feedback.

This thesis demonstrates the preliminary results of using phase-sensitive OCT for temperature feedback during laser surgery. Integrating the miniaturized infrared detector into the OCT system could provide a continuous calibration of the predicted temperature. In addition, as demonstrated in Figure 2.5, a clear change in the attenuation profile of bone tissue over the time of laser ablation is visible. Investigating the attenuation profile of bone in different conditions (fresh, dehydrated, and carbonized) can lead to another feedback for the irrigation system to prevent thermal damage.

We presented the first prototype of the miniaturized OCT-guided laser osteotomy. Nevertheless, additional improvements are essential to achieve the required size for minimally invasive laser osteotomy [83]. For instance, exploring the development of double-clad fiber optic for OCT and Er:YAG laser wavelengths represents a promising solution to meet this objective. A shared challenge in the scanning mechanism used for endoscopic applications is its low-temperature tolerance, which hindered its implementation in this study. Further investigation on the isolating mechanism between optics and electronics in the scanning system can potentially address this challenge.

6.3 Conclusion

In conclusion, we have developed a long-range visual feedback system capable of monitoring the depth of the cut and temperature rise in bone tissue and producing three-dimensional images of the cut. This feedback mechanism was integrated with an Er:YAG laser to provide real-time controlled laser osteotomy. Finally, the integrated OCT system and Er:YAG laser was miniaturized for minimally invasive surgery.

Bibliography

[1] Ensieh Khalkhal, Majid Rezaei-Tavirani, Mohammad Reza Zali, and Zahra Akbari. The evaluation of laser application in surgery: a review article. *Journal of Lasers in Medical Sciences*, 10(Suppl 1):S104, 2019.

[2] Qian Peng, Asta Juzeniene, Jiyao Chen, Lars O Svaasand, Trond Warloe, Karl-Erik Giercksky, and Johan Moan. Lasers in medicine. *Reports on Progress in Physics*, 71(5):056701, 2008.

[3] Leon Goldman. *The biomedical laser: technology and clinical applications*. Springer Science & Business Media, 2013.

[4] WE Siebert. History of lasers in orthopedic medicine. In *Lasers in the Musculoskeletal System*, pages 3–6. Springer, 2001.

[5] Herbert Deppe and Hans-Henning Horch. Laser applications in oral surgery and implant dentistry. *Lasers in medical science*, 22(4):217–221, 2007.

[6] J Stuart Nelson, Arie Orenstein, Lih-Huei L Liaw, and Michael W Berns. Mid-infrared erbium: Yag laser ablation of bone: The effect of laser osteotomy on bone healing. *Lasers in surgery and medicine*, 9(4):362–374, 1989.

[7] Shinichi Watanabe. Basics of laser application to dermatology. *Archives of dermatological research*, 300(1):21–30, 2008.

[8] Harvey A Wigdor, Joseph T Walsh Jr, John DB Featherstone, Steven R Visuri, Daniel Fried, and Joseph L Waldvogel. Lasers in dentistry. *Lasers in surgery and medicine*, 16(2):103–133, 1995.

[9] Gustavo Lisboa Martins, Edela Puricelli, Carlos Eduardo Baraldi, and Deise Ponzoni. Bone healing after bur and er: Yag laser ostectomies. *Journal of Oral and Maxillofacial Surgery*, 69(4):1214–1220, 2011.

[10] Yujin Ohsugi, Akira Aoki, Koji Mizutani, Sayaka Katagiri, Motohiro Komaki, Masahiro Noda, Toru Takagi, Sho Kakizaki, Walter Meinzer, and Yuichi Izumi. Evaluation of bone healing following er: Yag laser ablation in rat calvaria compared with bur drilling. *Journal of biophotonics*, 12(3):e201800245, 2019.

[11] Kyung-won Baek, Waldemar Deibel, Dilyan Marinov, Mathias Griessen, Michel Dard, Alfredo Bruno, Hans-Florian Zeilhofer, Philippe Cattin, and Philipp Juergens. A comparative investigation of bone surface after cutting with mechanical tools and er: Yag laser. *Lasers in surgery and medicine*, 47(5):426–432, 2015.

[12] Marko Blaskovic, Dragana Gabrić, Nichola J Coleman, Ian J Slipper, Mitko Mladenov, and Elizabeta Gjorgievska. Bone healing following different types of osteotomy: scanning electron microscopy (sem) and three-dimensional sem analyses. *Microscopy and Microanalysis*, 22(6):1170–1178, 2016.

[13] Omar S Bholat, Randy S Haluck, Willie B Murray, Paul J Gorman, and Thomas M Krummel. Tactile feedback is present during minimally invasive surgery. *Journal of the American College of Surgeons*, 189(4):349–355, 1999.

[14] GD Rajitha Gunaratne, Riaz Khan, Daniel Fick, Brett Robertson, Narendra Dahotre, and Charlie Ironside. A review of the physiological and histological effects of laser osteotomy. *Journal of medical engineering & technology*, 41(1):1–12, 2017.

[15] Florian Stelzle, Katja Tangermann-Gerk, Werner Adler, Azhar Zam, Michael Schmidt, Alexandre Douplik, and Emeka Nkenke. Diffuse reflectance spectroscopy for optical soft tissue differentiation as remote feedback control for tissue-specific laser surgery. *Lasers in Surgery and Medicine: The Official Journal of the American Society for Laser Medicine and Surgery*, 42(4):319–325, 2010.

[16] Erwin Bay, Xosé Luís Deán-Ben, Genny A Pang, Alexandre Douplik, and Daniel Razansky. Real-time monitoring of incision profile during laser surgery using shock wave detection. *Journal of biophotonics*, 8(1-2):102–111, 2015.

[17] Gerard S Letterie. Ultrasound guidance during endoscopic procedures. *Obstetrics and gynecology clinics of North America*, 26(1):63–82, 1999.

[18] Kamran Ahrar and R Jason Stafford. Magnetic resonance imaging–guided laser ablation of bone tumors. *Techniques in vascular and interventional radiology*, 14(3):177–182, 2011.

[19] Stephen A Boppart, Juergen Herrmann, Costas Pitris, Debra L Stamper, Mark E Brezinski, and James G Fujimoto. High-resolution optical coherence tomography-guided laser ablation of surgical tissue. *Journal of Surgical Research*, 82(2):275–284, 1999.

[20] Fanuel Mehari, Maximillian Rohde, Rajesh Kanawade, Christian Knipfer, Werner Adler, Florian Klämpfl, Florian Stelzle, and Michael Schmidt. Investigation of the differentiation of ex vivo nerve and fat tissues using laser-induced breakdown spectroscopy (libs): Prospects for tissue-specific laser surgery. *Journal of biophotonics*, 9(10):1021–1032, 2016.

[21] Arsham Hamidi, Yakub A Bayhaqi, Ferda Canbaz, Alexander A Navarini, Philippe C Cattin, and Azhar Zam. Long-range optical coherence tomography with extended depth-of-focus: a visual feedback system for smart laser osteotomy. *Biomedical Optics Express*, 12(4):2118–2133, 2021.

[22] Arsham Hamidi, Yakub A Bayhaqi, Sandra Drusová, Alexander A Navarini, Philippe C Cattin, Ferda Canbaz, and Azhar Zam. Multimodal feedback systems for smart laser osteotomy: Depth control and tissue differentiation. *Lasers in Surgery and Medicine*, 2023.

[23] Arsham Hamidi, Yakub A Bayhaqi, Ferda Canbaz, Alexander A Navarini, Philippe C Cattin, and Azhar Zam. Towards phase-sensitive optical coherence tomography in smart laser osteotomy: temperature feedback. *Lasers in Medical Science*, 38(1):222, 2023.

[24] Arsham Hamidi, Yakub A Bayhaqi, Alexander A Navarini, Philippe C Cattin, Azhar Zam, and Ferda Canbaz. Towards miniaturized oct-guided laser osteotomy: integration of fiber-coupled er: Yag laser with oct. *Optics Continuum*, 2(10):2106–2115, 2023.

[25] Theodore H Maiman et al. Stimulated optical radiation in ruby. 1960.

[26] DSJ Choy. History of lasers in medicine. *The Thoracic and cardiovascular surgeon*, 36(S 2):114–117, 1988.

[27] Michael L Geiges. History of lasers in dermatology. In *Basics in dermatological laser applications*, volume 42, pages 1–6. Karger Publishers, 2011.

[28] Myron C Muckerheide. Laser medical technology for the twenty-first century. In *The Biomedical Laser*, pages 313–324. Springer, 1981.

[29] Margi A Gilmour. Lasers in ophthalmology. *Veterinary Clinics: Small Animal Practice*, 32(3):649–672, 2002.

[30] Elizabeth L Tanzi, Jason R Lupton, and Tina S Alster. Lasers in dermatology: four decades of progress. *Journal of the American Academy of Dermatology*, 49(1):1–34, 2003.

[31] Sanjeev Kumar Verma, Sandhya Maheshwari, Raj Kumar Singh, and Prabhat Kumar Chaudhari. Laser in dentistry: An innovative tool in modern dental practice. *National journal of maxillofacial surgery*, 3(2):124, 2012.

[32] Roy George. Laser in dentistry-review. *Int J Dent Clin*, 1(1):13–19, 2009.

[33] Yue Zhang, Chengyong Wang, Shaobo Zhou, Wentao Jiang, Zhihua Liu, and Linlin Xu. A comparison review on orthopedic surgery using piezosurgery and conventional tools. *Procedia Cirp*, 65:99–104, 2017.

[34] Umberto Romeo, Alessandro Del Vecchio, Gaspare Palata, Gianluca Tenore, Paolo Visca, and Claudia Maggiore. Bone damage induced by different cutting instruments: an in vitro study. *Brazilian Dental Journal*, 20:162–168, 2009.

[35] Stefan Stübinger. Advances in bone surgery: the er: Yag laser in oral surgery and implant dentistry. *Clinical, Cosmetic and Investigational Dentistry*, 2:47, 2010.

[36] Zhao-Zhang Li, Lou Reinisch, and Willem P Van de Merwe. Bone ablation with er: Yag and co2 laser: study of thermal and acoustic effects. *Lasers in Surgery and Medicine*, 12(1):79–85, 1992.

[37] Zhenzhi Ying, Liming Shu, and Naohiko Sugita. Bone milling: On monitoring cutting state and force using sound signals. *Chinese Journal of Mechanical Engineering*, 35(1):1–12, 2022.

[38] Stephan Rupprecht, Katja Tangermann-Gerk, Joerg Wiltfang, Friedrich Wilhelm Neukam, and Andreas Schlegel. Sensor-based laser ablation for tissue specific cutting: an experimental study. *Lasers in medical science*, 19(2):81–88, 2004.

[39] Jose A Robles-Linares, Dragos Axinte, Zhirong Liao, and Andres Gameros. Machining-induced thermal damage in cortical bone: Necrosis and micro-mechanical integrity. *Materials & Design*, 197:109215, 2021.

[40] Yici Guo, PP Ho, H Savage, D Harris, P Sacks, S Schantz, Feng Liu, N Zhadin, and RR Alfano. Second-harmonic tomography of tissues. *Optics Letters*, 22(17):1323–1325, 1997.

[41] Paul JL Webster, Logan G Wright, Kevin D Mortimer, Ben Y Leung, Joe XZ Yu, and James M Fraser. Automatic real-time guidance of laser machining with inline coherent imaging. *Journal of Laser Applications*, 23(2):022001, 2011.

[42] Francesco P Mezzapesa, Lorenzo Columbo, Massimo Brambilla, Maurizio Dabbicco, Antonio Ancona, Teresa Sibillano, Francesco De Lucia, Pietro M Lugarà, and Gaetano Scamarcio. Simultaneous measurement of multiple target displacements by self-mixing interferometry in a single laser diode. *Optics Express*, 19(17):16160–16173, 2011.

[43] Paul JL Webster, Matthew S Muller, and James M Fraser. High speed in situ depth profiling of ultrafast micromachining. *Optics express*, 15(23):14967–14972, 2007.

[44] Ashley J Welch, Martin JC Van Gemert, et al. *Optical-thermal response of laser-irradiated tissue*, volume 2. Springer, 2011.

[45] Markolf H Niemz et al. *Laser-tissue interactions*, volume 322. Springer, 2007.

[46] Paola Saccomandi, Emiliano Schena, and Sergio Silvestri. Techniques for temperature monitoring during laser-induced thermotherapy: an overview. *International Journal of Hyperthermia*, 29(7):609–619, 2013.

[47] Lina M Beltrán Bernal, Ferda Canbaz, Antoine Droneau, Niklaus F Friederich, Philippe C Cattin, and Azhar Zam. Optimizing deep bone ablation by means of a microsecond er: Yag laser and a novel water microjet irrigation system. *Biomedical Optics Express*, 11(12):7253–7272, 2020.

[48] Ngot Thi Pham, Seul Lee Lee, Suhyun Park, Yong Wook Lee, and Hyun Wook Kang. Real-time temperature monitoring with fiber bragg grating sensor during diffuser-assisted laser-induced interstitial thermotherapy. *Journal of biomedical optics*, 22(4):045008, 2017.

[49] Davide Polito, Michele Arturo Caponero, Andrea Polimadei, Paola Saccomandi, Carlo Massaroni, Sergio Silvestri, and Emiliano Schena. A needlelike probe for temperature monitoring during laser ablation based on fiber bragg grating: Manufacturing and characterization. *Journal of Medical Devices*, 9(4), 2015.

[50] Sean M Munier, Allison S Liang, Akshay N Desai, Jose K James, and Shabbar F Danish. Characterization of magnetic resonance thermal imaging signal artifact during magnetic resonance guided laser-induced thermal therapy. *Operative Neurosurgery*, 19(5):619–624, 2020.

[51] Irina V Larina, Kirill V Larin, and Rinat O Esenaliev. Real-time optoacoustic monitoring of temperature in tissues. *Journal of Physics D: Applied Physics*, 38(15):2633, 2005.

[52] Francisco Javier Oyaga Landa, Xosé Luís Deán-Ben, Ronald Sroka, and Daniel Razansky. Volumetric optoacoustic temperature mapping in photothermal therapy. *Scientific reports*, 7(1):1–8, 2017.

[53] Heike H Müller, Lars Ptaszynski, Kerstin Schlott, Christina Debbeler, Marco Bever, Stefan Koinzer, Reginald Birngruber, Ralf Brinkmann, and Gereon Hüttmann. Imaging thermal expansion and retinal tissue changes during photocoagulation by high speed oct. *Biomedical optics express*, 3(5):1025–1046, 2012.

[54] Desmond C Adler, Shu-Wei Huang, Robert Huber, and James G Fujimoto. Photothermal detection of gold nanoparticles using phase-sensitive optical coherence tomography. *Optics express*, 16(7):4376–4393, 2008.

[55] Piotr Targowski, Bogumiła Rouba, Maciej Wojtkowski, and Andrzej Kowalczyk. The application of optical coherence tomography to non-destructive examination of museum objects. *Studies in conservation*, 49(2):107–114, 2004.

[56] Erkki Alarousu, Leszek Krehut, Tuukka Prykäri, and Risto Myllylä. Study on the use of optical coherence tomography in measurements of paper properties. *Measurement Science and Technology*, 16(5):1131, 2005.

[57] Yi Wang, Shanshan Liu, Shiliang Lou, Weiqian Zhang, Huaiyu Cai, and Xiaodong Chen. Application of optical coherence tomography in clinical diagnosis. *Journal of X-ray Science and Technology*, 27(6):995–1006, 2019.

[58] James G Fujimoto. Biomedical imaging and optical biopsy using optical coherence tomography. *The Journal of the Japan Society for Respiratory Endoscopy*, 23(3):188, 2001.

[59] James G Fujimoto and Wolfgang Drexler. Introduction to oct. *Optical Coherence Tomography*, page 3, 2015.

[60] David Huang, Eric A Swanson, Charles P Lin, Joel S Schuman, William G Stinson, Warren Chang, Michael R Hee, Thomas Flotte, Kenton Gregory, Carmen A Puliafito, et al. Optical coherence tomography. *science*, 254(5035):1178–1181, 1991.

[61] Frank L Pedrotti, Leno M Pedrotti, and Leno S Pedrotti. *Introduction to optics*. Cambridge University Press, 2017.

[62] Albert A Michelson and Edward W Morley. Lix. on a method of making the wavelength of sodium light the actual and practical standard of length. *The London, Edinburgh, and Dublin Philosophical Magazine and Journal of Science*, 24(151):463–466, 1887.

[63] Leonard Mandel and Emil Wolf. *Optical coherence and quantum optics*. Cambridge university press, 1995.

[64] W Gao and X Wu. Differences between time domain and fourier domain optical coherence tomography in imaging tissues. *Journal of Microscopy*, 268(2):119–128, 2017.

[65] Wolfgang Drexler, Mengyang Liu, Abhishek Kumar, Tschackad Kamali, Angelika Unterhuber, and Rainer A Leitgeb. Optical coherence tomography today: speed, contrast, and multimodality. *Journal of biomedical optics*, 19(7):071412, 2014.

[66] Desmond Christopher Adler. *Applications of Fourier Domain Mode Locked lasers for optical coherence tomography imaging*. PhD thesis, Massachusetts Institute of Technology, 2009.

[67] Michael A Choma, Kevin Hsu, and Joseph A Izatt. Swept source optical coherence tomography using an all-fiber 1300-nm ring laser source. *Journal of biomedical optics*, 10(4):044009, 2005.

[68] Wolfgang Drexler, James G Fujimoto, et al. *Optical coherence tomography: technology and applications*, volume 2. Springer, 2015.

[69] Hrebesh M Subhash and Ruikang K Wang. Optical coherence tomography: technical aspects. In *Biomedical Optical Imaging Technologies*, pages 163–212. Springer, 2013.

[70] Guillermo J Tearney, Mark E Brezinski, Brett E Bouma, Stephen A Boppart, Costas Pitris, James F Southern, and James G Fujimoto. In vivo endoscopic optical biopsy with optical coherence tomography. *Science*, 276(5321):2037–2039, 1997.

[71] Michalina J Gora, Melissa J Suter, Guillermo J Tearney, and Xingde Li. Endoscopic optical coherence tomography: technologies and clinical applications. *Biomedical optics express*, 8(5):2405–2444, 2017.

[72] Zahid Yaqoob, Jigang Wu, Emily J McDowell, Xin Heng, and Changhuei Yang. Methods and application areas of endoscopic optical coherence tomography. *Journal of biomedical optics*, 11(6):063001, 2006.

[73] Zi-Kui Liu, Shun-Li Shang, and Yi Wang. Fundamentals of thermal expansion and thermal contraction. *Materials*, 10(4):410, 2017.

[74] John M Jewell, Charles Askins, and Ishwar D Aggarwal. Interferometric method for concurrent measurement of thermo-optic and thermal expansion coefficients. *Applied optics*, 30(25):3656–3660, 1991.

[75] Sergey A Telenkov, Digant P Dave, and Thomas E Milner. Low-coherence interferometric detection of photo-thermal and photo-acoustic effects in tissue. In *Biomedical Optoacoustics IV*, volume 4960, pages 142–146. SPIE, 2003.

[76] Ryan Scholl and Bruce W Liby. Using a michelson interferometer to measure coefficient of thermal expansion of copper. *The Physics Teacher*, 47(5):306–308, 2009.

[77] Desmond C Adler, Robert Huber, and James G Fujimoto. Phase-sensitive optical coherence tomography at up to 370,000 lines per second using buffered fourier domain mode-locked lasers. *Optics letters*, 32(6):626–628, 2007.

[78] Jihoon Kim, Junghwan Oh, and Thomas E Milner. Measurement of optical path length change following pulsed laser irradiation using differential phase optical coherence tomography. *Journal of biomedical optics*, 11(4):041122, 2006.

[79] Mohammad Hossein Salimi, Martin Villiger, and Nima Tabatabaei. Effects of lipid composition on photothermal optical coherence tomography signals. *Journal of biomedical optics*, 25(12):120501, 2020.

[80] David Veysset, Tong Ling, Yueming Zhuo, Vimal Prabhu Pandiyan, Ramkumar Sabesan, and Daniel Palanker. Interferometric imaging of thermal expansion for temperature control in retinal laser therapy. *Biomedical optics express*, 13(2):728–743, 2022.

[81] JM Tucker-Schwartz, TA Meyer, CA Patil, CL Duvall, and MC Skala. In vivo photothermal optical coherence tomography of gold nanorod contrast agents. *Biomedical optics express*, 3(11):2881–2895, 2012.

[82] Alexander A Oraevsky, Rinat O Esenaliev, Massoud Motamedi, and Alexander A Karabutov. Real time optoacoustic monitoring of changes in tissue properties, October 30 2001. US Patent 6,309,352.

[83] Manuela Eugster, Esther I Zoller, Philipp Krenn, Sandra Blache, Niklaus F Friederich, Magdalena Müller-Gerbl, Philippe C Cattin, and Georg Rauter. Quantitative evaluation of the thickness of the available manipulation volume inside the knee joint capsule for minimally invasive robotic unicondylar knee arthroplasty. *IEEE Transactions on Biomedical Engineering*, 68(8):2412–2422, 2020.

List of peer-reviewed publications and presentations on the thesis topic

Journal papers

Published

- **Hamidi, A.**, Bayhaqi, Y. A., Canbaz, F., Navarini, A. A., Cattin, P. C., and Zam, A. (2021). Long-range optical coherence tomography with extended depth-of-focus: a visual feedback system for smart laser osteotomy. Biomedical Optics Express, 12(4), 2118–2133.

- **Hamidi, A.**, Bayhaqi, Y. A., Canbaz, F., Navarini, A. A., Cattin, P. C., & Zam, A. (2023). Towards phase-sensitive optical coherence tomography in smart laser osteotomy: temperature feedback. Lasers in Medical Science, 38(1), 222.

- **Hamidi, A.**, Bayhaqi, Y. A., Navarini, A. A., Cattin, P. C., Zam, A., & Canbaz, F. (2023). Towards miniaturized OCT-guided laser osteotomy: integration of fiber-coupled Er: YAG laser with OCT. Optics Continuum, 2(10), 2106-2115.

- **Hamidi, A.**, Bayhaqi, Y. A., Drusová, S., Navarini, A. A., Cattin, P. C., Canbaz, F., & Zam, A. Multimodal feedback systems for smart laser osteotomy: Depth control and tissue differentiation. Lasers in Surgery and Medicine.

- Seppi, C., Huck, A., **Hamidi, A.**, Schnider, E., Filipozzi, M., Rauter, G., Zam, A., and Cattin, P. C. (2022). Bone Ablation Depth Approximation from Er: YAG Laser-generated Acoustic Waves. IEEE Access.

- Bayhaqi, Y. A., **Hamidi, A.**, Canbaz, F., Navarini, A. A., Cattin, P. C., and Zam, A. (2022). Deep-learning-based fast optical coherence tomography (OCT) image denoising for smart laser osteotomy. IEEE Transactions on Medical Imaging, 41(10), 2615–2628.

- Bayhaqi, Y. **A., Hamidi**, Canbaz, F., Navarini, A. A., Cattin, P. C., and Zam, A. (2021). Deep learning models comparison for tissue classification using optical coherence tomography images: toward smart laser osteotomy. OSA Continuum, 4(9), 2510–2526.

- Bayhaqi, Y. **, Hamidi, A.**, Navarini, A. A., Cattin, P. C., Canbaz, F., & Zam, A. (2023). Real-time closed-loop tissue-specific laser osteotomy using deep-learning-assisted optical coherence tomography. Biomedical Optics Express, 14(6), 2986-3002.

- Abbasi, H., Bernal, L. M. B., **Hamidi, A.**, Droneau, A., Canbaz, F., Guzman, R., and Zam, A. (2020). Combined Nd: YAG and Er: YAG lasers for real-time closed-loop tissue-specific laser osteotomy. Biomedical Optics Express, 11(4), 1790–1807.

Conference proceedings

- **Hamidi, A.**, Bayhaqi, Y. A., Canbaz, F., Navarini, A. A., Cattin, P. C., and Zam, A. (2021, June). Observation of controlled temperature changes of bone by phase-sensitive optical coherence tomography. In European Conference on Biomedical Optics (pp. ETu2A–38). Optical Society of America.

- **Hamidi, A.**, Bayhaqi, Y. A., Canbaz, F., Navarini, A., Cattin, P. C., and Zam, A. (2020, April). Imaging photothermal-induced expansion of bone during laser osteotomy by phase-sensitive OCT: preliminary results. In Biomedical Spectroscopy, Microscopy, and Imaging (Vol. 11359, pp. 127–133). SPIE.

Oral Presentations

- **Hamidi, A.**, Bayhaqi, Y. A., Canbaz, F., Navarini, A., Cattin, P. C., and Zam, A. EUCOR Crossborder: Crossing Borders for Joint Exchange and Collaboration in Biomedical Engineering: Two-day Networking Event, The 2018 Eucor-GRACE Crossborder Education Grant, La Bresse, France, 29–30 April 2019.

- **Hamidi, A.**, Bayhaqi, Y. A., Canbaz, F., Navarini, A., Cattin, P. C., and Zam, A. The 5th DBE Research Day, Zentrum für Lehre und Forschung, Basel, 28 August 2019.

- **Hamidi, A.**, Bayhaqi, Y. A., Canbaz, F., Navarini, A., Cattin, P. C., and Zam, A. Imaging photothermal-induced expansion of bone during laser osteotomy by phase-sensitive OCT: preliminary results (conference presentation), SPIE Photonics Europe 2020, Paper Number: 11359–19.

- **Hamidi, A.**, Bayhaqi, Y. A., Schmidt, I. T., Canbaz, F., Jian, Y., Navarini, A., and Zam, A. (2020, March). Ablation monitoring with integrated long-range OCT and Er: YAG laser for smart laserosteotomy (conference presentation). In Advanced Biomedical and Clinical Diagnostic and Surgical Guidance Systems XVIII (Vol. 11229, p. 1122914). SPIE.

- Bayhaqi, Y. A., **Hamidi, A.**, Navarini, A., Cattin, P. C., and Zam, A. (2020, March). Monte Carlo investigation of deep learning tissue classification performance in OCT-based smart laser bone surgery (conference presentation). In Advanced Biomedical and Clinical Diagnostic and Surgical Guidance Systems XVIII (Vol. 11229, p. 112290H). SPIE.

Poster Presentation

- The 7th DBE Research Day, Zentrum für Lehre und Forschung, Basel, 7 September 2021.

- Investigating the reliability of depth monitoring using OCT during laser osteotomy, Mesrob 2021, online, 7–9 June 2021.

- The 6th DBE Research Day, Zentrum für Lehre und Forschung, Basel, 8 September 2020.

- Development of long-range OCT for smart laser surgery, Biomedical Photonics Network (bmpn), 2019, Bern, Switzerland.

- The 4th DBE Research Day, Zentrum für Lehre und Forschung, Basel, 5 September 2018.